Towards a Long-Lived and Efficient Photonic Quantum Memory in a Thulium-Doped Crystal

Das, A.

DOI
10.4233/uuid:61c88b1b-1269-4cec-9e09-4b1ac0622d4f

Publication date
2023

Document Version
Final published version

Citation (APA)
Das, A. (2023). *Towards a Long-Lived and Efficient Photonic Quantum Memory in a Thulium-Doped Crystal*. [Dissertation (TU Delft), Delft University of Technology]. https://doi.org/10.4233/uuid:61c88b1b-1269-4cec-9e09-4b1ac0622d4f

Towards a Long-Lived and Efficient Photonic Quantum Memory in a Thulium-doped Crystal

TOWARDS A LONG-LIVED AND EFFICIENT PHOTONIC QUANTUM MEMORY IN A THULIUM-DOPED CRYSTAL

Dissertation

for the purpose of obtaining the degree of doctor
at Delft University of Technology,
by the authority of the Rector Magnificus Prof.dr.ir. T.H.J.J. van der Hagen;
Chair of the Board for Doctorates
to be defended publicly on
Wednesday 1st of February 2023 at 12:30 o'clock

by

Antariksha DAS

Master of Science in Physical Sciences,
Indian Institute of Science Education and Research (IISER), Kolkata, India
born in Dinhata, West Bengal, India.

This dissertation has been approved by the promotors.

promotor: prof. dr. W. Tittel
promotor: prof. dr. ir. R. Hanson

Composition of the promotion committee:

Rector Magnificus,	voorzitter
Prof. dr. W. Tittel,	Technische Universiteit Delft
Prof. dr. ir. R. Hanson,	Technische Universiteit Delft
Independent Members:	
Prof. dr. ir. L.M.K. Vandersypen,	Technische Universiteit Delft
Dr. J. Borregaard,	Technische Universiteit Delft
Prof. dr. P. Goldner	Institut de Recherche de Chimie Paris, Frankrijk
Prof. dr. M. Atatüre,	University of Cambridge
Prof. dr. S. Kröll,	Lund University
Reserve member:	
Prof. dr. S. Groeblacher,	Technische Universiteit Delft

Printed by: Gildeprint

ISBN 000-00-0000-000-0

An electronic version of this dissertation is available at
http://repository.tudelft.nl/.

A dream is not that which you see while sleeping, it is something that does not let you sleep.

- APJ Abdul Kalam

CONTENTS

SUMMARY

A future quantum network will allow distributing entanglement over arbitrarily long distances. This topic holds importance for applications in quantum information science as well as for fundamental investigations, and currently receives significant attention around the world. The most promising approach for achieving long-distance quantum communication over terrestrial links is to use quantum repeaters, many of which employ optical quantum memories to store quantum information.

The realization of an optical quantum memory is a challenging task. Not only do we want to realize a proof-of-principle of quantum storage, but we would also like to realize a quantum memory whose performances allow us to use it in a quantum repeater for long-distance quantum communication. In this thesis, I will present the different aspects I worked on toward such a goal.

In our group, we focus on rare-earth-ion-doped crystals which are very promising platforms, suitable for quantum memory applications. Depending on the task, some of the rare-earth elements are more promising than others, because of their unique spectroscopic properties. In my Ph.D., I investigated a thulium-doped yttrium gallium garnet (Tm:YGG) crystal.

The thesis starts by shedding light on the broad framework of long-distance quantum communication, and the role of quantum repeaters in achieving this goal. Then we highlight the scope of this thesis, an optical quantum memory, an essential component in the whole quantum repeater scheme. After a short introduction in chapter 1, chapter 2 elaborates on the frequency-multiplexed quantum repeater architecture and important features of rare-earth-doped materials in the context of quantum memory. We discuss the various criteria that are needed for a quantum memory to be useful in practical quantum communication purposes, namely long storage time, high multimode capacity, and high storage efficiency. We introduce several useful and widely-employed spectroscopic tools and techniques necessary to understand spectroscopic investigations and storage demonstrations.

Spectroscopy of rare earth-doped materials is an active field, with the goal of finding the ideal system with the best properties for quantum memory. Towards this end, in chapter 3, spectroscopic investigation and coherence measurements are performed on Tm:YGG at cryogenic temperatures (~500 mK). We implement the atomic frequency comb (AFC) protocol to demonstrate multiplexed storage of classical laser pulses in the temporal and spectral domains with the goal of using the Tm:YGG crystal for quantum storage.

By applying our newfound knowledge, in chapter 4, we model the population dynamics in Tm:YGG using frequency-dependent rate equations to explain the relaxation dynamics and to improve the spectral tailoring process for memory preparations. In addition to adiabatic pulse shaping for coherent population excitation, we detail the experimental limitations of the memory initialization process and also the system limitations

in the context of spectral diffusion over short, medium, and long-time scales.

Long optical storage times are required to achieve high entanglement distribution rates in quantum repeaters. In chapter 5, we show that Tm: YGG's optical coherence time can reach 1.1 ms, which is one of the longest optical coherence times reported for any rare-earth crystal. We demonstrate storage of laser pulses up to 100 μs record storage time. We confirm the possibility of frequency-multiplexed storage and feed-forward-based spectral mode mapping. We also show that quantum correlations between members of photon pairs persist throughout storage, i.e. that our memory can indeed operate in the quantum regime.

The limits of these experiments indicate new routes for improvement in memory parameters that are pursued in chapter 6. In order to improve memory efficiency, the idea of a monolithic impedance-matched cavity quantum memory is conceived. We show that absorption profiles of the created spectral features in the Tm:YGG crystal can be modified when embedded into a cavity and we simulate the impedance-matching criteria for our system. We discuss the measurements and our effort toward building an efficient alignment-free cavity quantum memory in Tm:YGG crystal.

Finally, in chapter 7, we conclude the thesis with an outlook and future improvements or potential projects that will help to design the next generation of optical quantum memories. We believe that the results of this thesis establish a promising photonic quantum memory platform for quantum communication and show the potential of rare-earth ion-doped materials, in particular thulium-doped yttrium gallium garnet for developing optical quantum memories.

SAMENVATTING

Een toekomstig kwantumnetwerk zal het mogelijk maken om verstrengeling te genereren over willekeurig lange afstanden. Dit is van belang voor toepassingen in de kwantuminformatiewetenschap en voor fundamenteel onderzoek, en krijgt momenteel wereldwijd veel aandacht. De meest veelbelovende manier om kwantumcommunicatie over lange aardse afstanden te bereiken is door gebruik te maken van kwantumrepeaters. Veel van deze apparaten gebruiken optische kwantumgeheugens om kwantuminformatie op te slaan.

Het realiseren van een optisch kwantumgeheugen is een uitdagende taak. We willen niet alleen een proof-of-principle kwantumopslag realiseren, maar we willen ook een kwantumgeheugen realiseren waarvan de prestaties ons in staat stellen het te gebruiken in een kwantumrepeater voor kwantumcommunicatie over lange afstand. In dit proefschrift zal ik de verschillende aspecten presenteren waaraan ik heb gewerkt om een dergelijk doel te bereiken.

In onze groep richten we ons op kristallen gedoteerd met ionen van zeldzame aardmetalen. Dit zijn veelbelovende platformen die geschikt zijn voor kwantumgeheugentoepassingen. Afhankelijk van de taak zijn sommige ionen van zeldzame aardmetalen veelbelovender dan andere. Dit komt door hun unieke spectroscopische eigenschappen. In mijn doctoraat heb ik een met thulium gedoteerd yttrium gallium granaat (Tm:YGG) kristal onderzocht.

Het proefschrift begint met licht te werpen op het brede raamwerk van lange-afstand kwantumcommunicatie, en de rol van kwantumrepeaters bij het bereiken van dit doel. Vervolgens belichten we het kernonderwerp van dit proefschrift, een optisch kwantumgeheugen, een essentieel onderdeel van het hele kwantumrepeater schema. Na een korte introductie in hoofdstuk 1, gaat hoofdstuk 2 dieper in op de frequentiegemultiplexte kwantumrepeaterarchitectuur en belangrijke kenmerken van materialen die gedoteerd zijn met ionen van zeldzameaardmetalen in de context van kwantumgeheugen. We bespreken de verschillende criteria die nodig zijn om een kwantumgeheugen bruikbaar te maken voor praktische kwantumcommunicatiedoeleinden, namelijk lange opslagtijd, hoge multimode-capaciteit en hoge opslagefficiëntie. We introduceren verschillende nuttige en veelgebruikte spectroscopische hulpmiddelen en technieken die nodig zijn om spectroscopische onderzoeken en opslagdemonstraties te begrijpen.

Spectroscopie van kristallen gedoteerd met zeldzame aardmetalen is een actief veld, met als doel het vinden van het ideale systeem met de beste eigenschappen voor een kwantumgeheugen. Hiertoe worden in hoofdstuk 3 spectroscopisch onderzoek en coherentiemetingen uitgevoerd op Tm:YGG bij cryogene temperatuurs (500 mK). We implementeren het atomaire frequentiekam (AFK)-protocol om multiplexopslag van klassieke laserpulsen in de temporele en spectrale domeinen aan te tonen met als doel het gebruik van het Tm:YGG-kristal voor kwantumopslag.

Door onze nieuw gegenereerde kennis toe te passen, modelleren we in hoofdstuk 4 de populatiedynamiek in Tm:YGG met behulp van frequentieafhankelijke snelheidsvergelijkingen om de relaxatiedynamiek te verklaren en om het spectrale aanpassingsproces voor geheugenvoorbereidingen te verbeteren. Naast adiabatische pulsvorming voor coherente populatie-excitatie, beschrijven we de experimentele beperkingen van het geheugeninitialisatieproces en ook de systeembeperkingen in de context van spectrale diffusie over korte, middellange en lange tijdschalen.

Lange optische opslagtijden zijn vereist om hoge verstrengelingsdistributiesnelheden in kwantumrepeaters te bereiken. In hoofdstuk 5 laten we zien dat de optische coherentietijd van Tm:YGG 1.1 ms kan bereiken, wat een van de langste optische coherentietijden is die is gerapporteerd voor enig kristal gedoteerd met een zeldzaam aardmetaal. We demonstreren opslag van laserpulsen tot 100 μs, wat een record is in termen van opslagtijd. We bevestigen de mogelijkheid van frequentiegemultiplexte opslag en feed-forward-gebaseerde spectrale modustoewijzing. We laten ook zien dat kwantumcorrelaties tussen leden van fotonparen blijven bestaan tijdens de opslag, d.w.z. dat ons geheugen inderdaad kan werken in het kwantumregime.

De limieten van deze experimenten geven nieuwe routes aan voor verbetering van geheugenparameters die in hoofdstuk 6 worden nagestreefd. Om de geheugenefficiëntie te verbeteren, is het idee van een monolithische impedantie-gematchte trilholteholte-quantumgeheugen bedacht. We laten zien dat absorptieprofielen van de gecreëerde spectrale kenmerken in het Tm:YGG-kristal kunnen worden gewijzigd wanneer ze in een trilholte worden ingebed en we simuleren de impedantie-aanpassingscriteria voor ons systeem. We bespreken de metingen en onze inspanningen om een efficiënte trilholte-kwantumgeheugen zonder uitlijning te bouwen in een Tm:YGG-kristal.

Tot slot, in hoofdstuk 7, sluiten we het proefschrift af met een vooruitblik en toekomstige verbeteringen of potentiële projecten die zullen helpen bij het ontwerpen van de volgende generatie optische kwantumgeheugens. We zijn van mening dat de resultaten van dit proefschrift een veelbelovend fotonisch kwantumgeheugenplatform voor kwantumcommunicatie vormen en het potentieel aantonen van met zeldzame aarde gedoteerde materialen, in het bijzonder met thulium gedoteerd yttrium gallium garnaat voor het ontwikkelen van optische kwantumgeheugens.

1

INTRODUCTION

No dream is ever chased alone.

Rahul Dravid

In the 20th century, often coined as the age of information, we have witnessed some fundamentally and radically new means of communication. Quantum communications gain increasing attention because it can enable secure communication and also provide technology to connect individual quantum computers to enhance their information processing power. The rapid development of various quantum technologies over the past decades suggests that we will soon find ourselves at yet another decisive point in history. Here, we briefly discuss some of the general goals and frameworks that underpin long-distance quantum communication, focusing in particular on quantum repeater-based large-scale quantum networks. With their ability to transfer and process quantum information, such networks could enable a range of fundamentally new applications. Thus, quantum networks could be at the heart of a new age of quantum information.

1

QUANTUM information science is a fast-growing field of research that studies situations in which information is encoded as quantum states [1]. The goal of this research area is to perform information processing tasks better than any possible classical counterpart within the exclusive framework of classical physics [2]. Advanced applications like quantum computing, quantum sensing and quantum communication, have the potential to revolutionize the way information is processed and communicated. Though it is difficult to foresee all applications of a future optically-connected quantum communication network, such a future quantum internet [3, 4] will enable us to establish completely secure communication [5] and blind quantum computing [6], atomic clock synchronization [7, 8], etc.

The basic unit of classical information processing is a bit, i.e. binary values of 0 or 1. Similarly, the basic unit of quantum information processing is the quantum bit or qubit, which is described by a superposition: $\alpha|0\rangle + \beta|1\rangle$, where $|0\rangle$ and $|1\rangle$ represent orthogonal basis states of a quantum system, and $|\alpha|^2 + |\beta|^2 = 1$. For example, two distinct times of arrival (temporal modes) of a photon could define the orthogonal basis states, e.g. an 'early' or 'late' arrival time would correspond to the basis states $|0\rangle$ or $|1\rangle$. This forms the so-called time-bin qubit [9].

Quantum communication is a branch of quantum information science and technology that facilitates the transmission of information in the form of qubits. Since the security of current cryptosystems is based on the inability of classical computers to efficiently factor large numbers [10, 11], the invention of quantum computers might endanger the secrecy of sensitive information transferred over the Internet. Quantum communication in parallel with classical communication offers a solution to overcome this security threat as it exploits the laws of quantum physics to protect the information channels against eavesdropping [5, 12].

1.1. QUANTUM REPEATERS FOR LONG-DISTANCE QUANTUM COMMUNICATION

The most common way of transmitting quantum information is to encode it into a photon and send it through an optical fiber. Despite a lot of progress, quantum communication still faces a distance barrier. The maximum distance and rate at which photons, and thus quantum information, can be distributed are ultimately limited by the optical attenuation introduced by the distribution link. For free-space links, the loss is mainly due to absorption. On the other hand, in optical fiber links, the loss is due to absorption and scattering loss inside the fiber. For these reasons, the signal decreases exponentially as the distance increases (0.2-0.3 dB/km using standard telecommunication fibers and photons at a telecommunication wavelength of 1550 nm).

In classical communication, where photons are also used to transmit information, signal amplifiers are used at intermediate distances (at repeater stations) to enhance the signal quality in order to overcome this exponential loss. However, there is no way of boosting a quantum state to extend the communication distance, as the "no-cloning

theorem" of quantum physics forbids the copying of an arbitrary quantum state. To overcome this problem and to extend the communication distance quantum repeaters are needed.

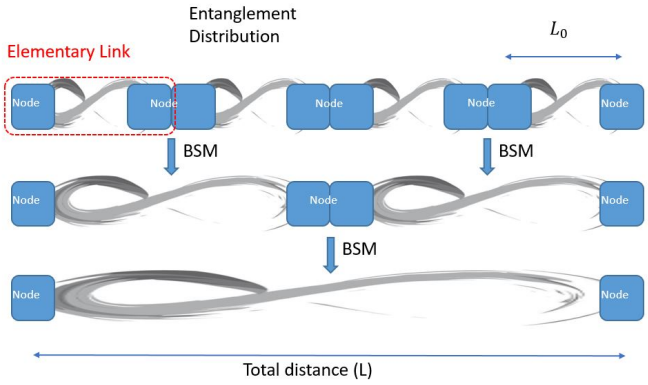

Figure 1.1: **Schematic of the quantum repeater:** Elementary links consist of two nodes. Bell-state measurements (BSM) between elementary links are performed for heralded entanglement distribution, represented by a bidirectional arrow.

Figure 1.1 shows the principle of how quantum repeaters are used to extend the communication distance to counteract the transmission loss. Each node in a quantum repeater (represented by the blue squares) contains an entangled photon pair source (the entangled photon pairs) and a multi-mode quantum memory. The main idea of a quantum repeater is to divide the entire communication link L into an array of shorter elementary links of distance L_0. Photons that are entangled with the quantum memories are transmitted over each elementary link. First, a Bell-state measurement is performed at the center of each link to establish entanglement between two quantum memories. Second, two neighboring links perform a local Bell-state measurement in order to generate entanglement over the distance of two elementary links. This process, which is known as entanglement swapping, continues (is concatenated) until entanglement is established across the entire communication link (two distance end-nodes). There are two well-known approaches for building a quantum repeater. In one of them, known as the Duan-Lukin-Cirac-Zoller (DLCZ) protocol [13], the processes of the generation and storage of entanglement are combined into the same system. In the other approach, which is the motivation for our quantum memory development, these processes are carried out by independent systems based on entangled photon pairs sources (Bell-pair or EPR sources) and absorptive quantum memories to store entangled photons [14, 15].

A conceptual schematic of such a quantum repeater architecture is depicted in Figure 1.2, where two elementary links connected via a local BSM (Bell-state measurement) are shown. Each elementary link is composed of two entangled photon pair sources (Bell-pair/EPR pair); two quantum memories (QM), and in between a Bell-state measurement (BSM). In an elementary link, one photon from each photon pair is sent to-

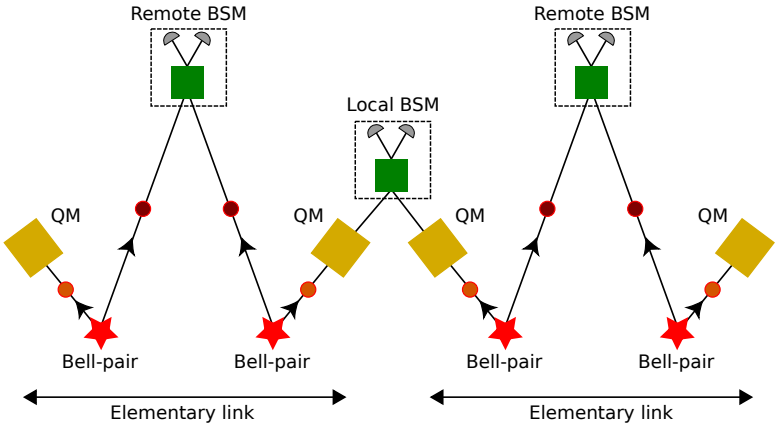

Figure 1.2: **Schematic of the quantum repeater with its main components:** A quantum repeater based on absorptive quantum memories (QM) and entangled photon-pair sources (Bell-pairs). BSM indicates the Bell-state measurement which is necessary in order to establish entanglement over the entire communication channel.

wards the remote Bell-state measurement (BSM) via a quantum channel (an optical fiber/free space) while the other one is stored in a quantum memory. Photons from the two nodes meet halfway between the nodes and a Bell-state measurement (BSM), which consists of a beam splitter and two single-photon detectors is performed. A successful BSM heralds the establishment of entanglement between the two quantum memories. The pairwise entanglement between the photons and the respective quantum memories in the elementary link is swapped to the entanglement between the two quantum memories at the ends of an elementary link by means of a BSM (Bell-state measurement). Thus, the entanglement is extended over the entire elementary link. Therefore, the main role of quantum memory is to store and preserve entangled photons and hold them until the entanglement is also created across the adjacent link. The minimum lifetime of the quantum memory has to be the time it takes for the photons to travel halfway toward the remote BSM station and for the heralding signal about the successful entanglement operation to travel back. The whole procedure must be concatenated over multiple elementary links in order to extend the entanglement further. However, this is not as straightforward in practice. Due to the probabilistic nature of the BSM or the source, normally one needs to repeat the process many times before the entanglement between two nodes is successfully established. This requires an even longer storage time for the quantum memory, especially for a long chain of elementary links in a quantum network containing many quantum repeater nodes.

1.2. LONG-LIVED QUANTUM MEMORIES FOR QUANTUM REPEATERS

In this thesis, I will particularly focus on one of the building blocks of the quantum repeater namely the quantum memory. A quantum memory is a device that can take in quantum information (or quantum state), store (and preserve) it, and emit it after a certain time [16, 17]. Quantum information or quantum states generally refers physical

information contained in the state of a quantum system. In our case a quantum bit (or qubit). The qubit a two-level quantum system that is described by: $\alpha|0\rangle + e^{i\theta}\beta|1\rangle$, where $|0\rangle$ and $|1\rangle$ represent two orthogonal states, θ is the phase, and $|\alpha|^2 + |\beta|^2 = 1$. In order to maintain the “quantumness", the quantum state should remain “pure" against the external (or “environmental") perturbation, known as decoherence. Decoherence induces bit flips or phase flips which transform the pure quantum state into a non-pure “mixed" state. The purity of a quantum state is necessary to perform quantum computing on quantum information encoded in it. The longer the purity of a quantum state will remain, the more useful it will be. Therefore, the need of having a long-lived quantum memory is perceived.

Quantum memories can be used to store intermediate results of a quantum computation where they can improve gate operation time. It is one of the most important elements of quantum computing based on the linear optics scheme [18]. Quantum memories are also an important constituent in quantum repeaters [13, 19] for long-distance quantum communication where they are used for signal synchronization. Other applications of quantum memories include storing quantum information for optical quantum processing [20], and the implementation of a deterministic single-photon source [21] to name a few.

As discussed in the previous section, quantum memories play a vital role in long-distance quantum communication in order to distribute quantum information in certain quantum repeater protocols [14, 22, 23]. Highly multimode, efficient, and long-lived quantum memories are necessary to construct a multiplexed quantum repeater that allows achieving useful communication rates. Memories that can store many photons simultaneously in different degrees of freedom (temporal, spectral, and spatial), increase the entanglement distribution rate of repeater-based quantum communication channels [15, 24]. In particular, it is possible to employ spectrally-multiplexed states together with memories with fixed storage time, supplemented with feed-forward selection, shifting, and filtering of spectral modes [24, 25] to achieve this goal.

1.3. ENSEMBLE-BASED OPTICAL QUANTUM MEMORIES

Arguably the simplest way to create a quantum memory is to use optical fibers which serve as simple delay lines. This approach is often used for photon synchronization purposes [26]. The storage time of an optical delay line is limited by the propagation loss in the fiber for a specific wavelength of the photon, and it is determined by the length of the fiber, which sometimes can be a practical limitation. Alternatively, light can also be injected into a cavity with a high-quality factor and later can be recalled through an electro-optical switch [27]. One can also use individual systems such as trapped ions [28] or single atoms in high finesse cavities [29]. On the other hand, in the atomic ensemble approach, a large collection of atoms or an atomic ensemble can be used to efficiently store the quantum states of light as a collective excitation of many atoms. In contrast to optical delay lines or cavity-enhanced interaction of light with single atoms, the atomic ensemble-based approach makes it miuch easier to achieve strong and controllable coupling between the atoms and the photons due to its large optical thickness .

Atomic ensembles are also very promising candidates for multiplexed quantum memories. Quantum storage of light was first demonstrated in rubidium and cesium vapors [30, 31]. A usual difficulty in such a system is the decoherence and doppler broadening due to atomic collisions. To overcome this, one solution is to cool and trap the atom, using a magneto-optical trap (MOT) [32] or optical lattices [33]. But this comes with the drawback of higher complexity of the experiment. Hence, among all the possible candidates, rare-earth-ion-doped (REID) crystals [34–36] are among the most promising candidates for optical quantum memories. They offer many interesting and unique spectroscopic properties such as long optical and spin coherence time, a broad absorption spectrum, etc [25, 37–39].

1.4. THESIS SYNOPSIS

The remainder of this chapter briefly summarizes and describes my work during the Ph.D. period and my contribution to each of the papers/articles, that are at the heart of the different chapters of this thesis. The objective of my Ph.D. project was to develop a multimode, long-lived and efficient quantum memory for a quantum repeater. The subsequent chapters of this thesis encompass my work on the creation of a solid-state quantum memory made in a thulium-doped yttrium gallium garnet (Tm: YGG) crystal.

This thesis contains 6 chapters:

- In this chapter (**Chapter 1**), we discuss the importance of ensemble-based solid-state quantum memories in quantum repeater architectures. We also briefly discussed the significance of long-lived multimode quantum memory toward creating an efficient multiplexed quantum repeater architecture.
- In **chapter 2**, I will introduce on the basic tools and knowledge required to understand spectroscopic studies and storage demonstration performed in a Tm: YGG crystal. More specifically, I will discuss the benefits of multiplexing and the frequency multiplexed quantum repeater architecture, rare-earth-ion-doped materials as potential quantum memory platforms, their properties and related spectroscopic tools to characterize them, and lastly the atomic frequency comb-based quantum memory protocol, which has been used throughout in this thesis for quantum storage of light.
- **Chapter 3** introduces Tm:YGG as a potential quantum memory platform. The characteristic properties of this crystal and the motivation behind our investigations are laid out. This chapter characterizes optical decoherence and magnetic field dependent spectral diffusion in a thulium-doped crystal featuring milliseconds long optical coherence time and long-lived Zeeman (spin) sub-levels. This is crucial in order to create an efficient and long-lived quantum memory.
- **Chapter 4** focuses on understanding, improving and optimizing the optical pumping process for creating efficient atomic frequency comb-based memories in Tm:YGG.

This includes adiabatic pulse shaping for pump pulses, modeling frequency-dependent rate equations for optical pumping in a three-level system of Tm:YGG to understand spectral hole burning, and the time evolution of spectral features in the context of magnetic field-dependent spectral diffusion.

- In **chapter 5**, we use a cryogenically cooled thulium-doped YGG crystal as a quantum storage device. We show that Tm:YGG's optical coherence time T_2 can reach 1.1 ms, which is one of the longest T_2 reported for any rare-earth crystal, and we demonstrate storage of laser pulses of up to 100 μsec. We confirm the possibility for feed-forward-based spectral mode mapping, and we also show that quantum correlations between members of photon pairs persist throughout storage, i.e. that our memory can operate in the quantum regime.

- In **chapter 6**, we investigate the experimental limits imposed by our memory system which indicates routes for improvement in memory parameters. In particular,we discuss the possibility to use a monolithic impedance-matched cavity quantum memory to improve the storage efficiency. We show that absorption profiles for the created spectral features in the Tm:YGG crystal are modified when embedded into a cavity and we simulate the impedance-matching criteria for our system. We discuss the measurements and our effort toward building an efficient alignment-free cavity quantum memory in Tm:YGG crystal.

- Lastly, in **chapter 7** I conclude my thesis with a general discussion on the results and provide an outlook on potential future developments.

BIBLIOGRAPHY

[1] J. P. Dowling and G. J. Milburn, "Quantum technology: the second quantum revolution", Philosophical Transactions of the Royal Society of London. Series A: Mathematical, Physical and Engineering Sciences **361**, 1655–1674 (2003).

[2] M. Nielsen, *A & chuang, il quantum computation and information*, 2000.

[3] H. J. Kimble, "The quantum internet", Nature **453**, 1023–1030 (2008).

[4] S. Wehner, D. Elkouss, and R. Hanson, "Quantum internet: a vision for the road ahead", Science **362**, 10.1126/science.aam9288 (2018).

[5] N. Gisin, G. Ribordy, W. Tittel, and H. Zbinden, "Quantum cryptography", Reviews of modern physics **74**, 145 (2002).

[6] J. F. Fitzsimons, "Private quantum computation: an introduction to blind quantum computing and related protocols", npj Quantum Information **3**, 1–11 (2017).

[7] E. O. Ilo-Okeke, L. Tessler, J. P. Dowling, and T. Byrnes, "Remote quantum clock synchronization without synchronized clocks", npj Quantum Information **4**, 1–5 (2018).

[8] J. Shi and S. Shen, "A clock synchronization method based on quantum entanglement", Scientific Reports **12**, 1–6 (2022).

[9] J. Brendel, N. Gisin, W. Tittel, and H. Zbinden, "Pulsed energy-time entangled twin-photon source for quantum communication", Physical Review Letters **82**, 2594 (1999).

[10] R. L. Rivest, A. Shamir, and L. Adleman, "A method for obtaining digital signatures and public-key cryptosystems", Communications of the ACM **21**, 120–126 (1978).

[11] P. W. Shor, "Algorithms for quantum computation: discrete logarithms and factoring", in Proceedings 35th annual symposium on foundations of computer science (Ieee, 1994), pp. 124–134.

[12] C. H. Bennett and G. Brassard, *Proceedings of the ieee international conference on computers, systems and signal processing*, 1984.

[13] L.-M. Duan, M. D. Lukin, J. I. Cirac, and P. Zoller, "Long-distance quantum communication with atomic ensembles and linear optics", Nature **414**, 413–418 (2001).

[14] C. Simon, H. De Riedmatten, M. Afzelius, N. Sangouard, H. Zbinden, and N. Gisin, "Quantum repeaters with photon pair sources and multimode memories", Physical review letters **98**, 190503 (2007).

[15] E. Saglamyurek et al., "A multiplexed light-matter interface for fibre-based quantum networks", Nature communications **7**, 1–7 (2016).

[16] W. Tittel, M. Afzelius, T. Chaneliere, R. L. Cone, S. Kröll, S. A. Moiseev, and M. Sellars, "Photon-echo quantum memory in solid state systems", Laser & Photonics Reviews **4**, 244–267 (2010).

[17] A. I. Lvovsky, B. C. Sanders, and W. Tittel, "Optical quantum memory", Nature photonics **3**, 706–714 (2009).

[18] P. Kok, W. J. Munro, K. Nemoto, T. C. Ralph, J. P. Dowling, and G. J. Milburn, "Linear optical quantum computing with photonic qubits", Reviews of modern physics **79**, 135 (2007).

[19] N. Sangouard, C. Simon, H. De Riedmatten, and N. Gisin, "Quantum repeaters based on atomic ensembles and linear optics", Reviews of Modern Physics **83**, 33 (2011).

[20] E. Knill, R. Laflamme, and G. J. Milburn, "A scheme for efficient quantum computation with linear optics", nature **409**, 46–52 (2001).

[21] S. Chen, Y.-A. Chen, T. Strassel, Z.-S. Yuan, B. Zhao, J. Schmiedmayer, and J.-W. Pan, "Deterministic and storable single-photon source based on a quantum memory", Physical review letters **97**, 173004 (2006).

[22] H. Krovi, S. Guha, Z. Dutton, J. A. Slater, C. Simon, and W. Tittel, "Practical quantum repeaters with parametric down-conversion sources", Applied Physics B **122**, 52 (2016).

[23] S. Guha, H. Krovi, C. A. Fuchs, Z. Dutton, J. A. Slater, C. Simon, and W. Tittel, "Rate-loss analysis of an efficient quantum repeater architecture", Phys. Rev. A **92**, 022357 (2015).

[24] N. Sinclair et al., "Spectral multiplexing for scalable quantum photonics using an atomic frequency comb quantum memory and feed-forward control", Phys. Rev. Lett. **113**, 053603 (2014).

[25] M. F. Askarani et al., "Long-lived solid-state optical memory for high-rate quantum repeaters", Phys. Rev. Lett. **127**, 220502 (2021).

[26] O. Landry, J. A. W. van Houwelingen, A. Beveratos, H. Zbinden, and N. Gisin, "Quantum teleportation over the swisscom telecommunication network", JOSA B **24**, 398–403 (2007).

[27] T. Pittman, B. Jacobs, and J. Franson, "Single photons on pseudodemand from stored parametric down-conversion", Physical Review A **66**, 042303 (2002).

[28] L.-M. Duan and C. Monroe, "Colloquium: quantum networks with trapped ions", Reviews of Modern Physics **82**, 1209 (2010).

[29] H. P. Specht, C. Nölleke, A. Reiserer, M. Uphoff, E. Figueroa, S. Ritter, and G. Rempe, "A single-atom quantum memory", Nature **473**, 190–193 (2011).

[30] M. D. Eisaman, A. André, F. Massou, M. Fleischhauer, A. S. Zibrov, and M. D. Lukin, "Electromagnetically induced transparency with tunable single-photon pulses", Nature **438**, 837–841 (2005).

[31] B. Julsgaard, J. Sherson, J. I. Cirac, J. Fiurášek, and E. S. Polzik, "Experimental demonstration of quantum memory for light", Nature **432**, 482–486 (2004).

[32] T. Chanelière, D. Matsukevich, S. Jenkins, S.-Y. Lan, T. Kennedy, and A. Kuzmich, "Storage and retrieval of single photons transmitted between remote quantum memories", Nature **438**, 833–836 (2005).

[33] R. Zhao, Y. Dudin, S. Jenkins, C. Campbell, D. Matsukevich, T. Kennedy, and A. Kuzmich, "Long-lived quantum memory", Nature Physics **5**, 100–104 (2009).

[34] B. Jacquier et al., *Spectroscopic properties of rare earths in optical materials*, Vol. 83 (Springer Science & Business Media, 2005).

[35] R. Macfarlane and R. Shelby, "Coherent transient and holeburning spectroscopy of rare earth ions in solids", in *Modern problems in condensed matter sciences*, Vol. 21 (Elsevier, 1987), pp. 51–184.

[36] T. Zhong and P. Goldner, "Emerging rare-earth doped material platforms for quantum nanophotonics", Nanophotonics **8**, 2003–2015 (2019).

[37] T. Böttger, C. W. Thiel, Y. Sun, and R. L. Cone, "Optical decoherence and spectral diffusion at 1.5 μm in $Er^{3+}:Y_2SiO_5$ versus magnetic field, temperature, and Er^{3+} concentration", Phys. Rev. B **73**, 075101 (2006).

[38] R. W. Equall, Y. Sun, R. L. Cone, and R. M. Macfarlane, "Ultraslow optical dephasing in Eu^{3+}:Y_2 SiO_5", Phys. Rev. Lett. **72**, 2179–2182 (1994).

[39] M. Zhong, M. P. Hedges, R. L. Ahlefeldt, J. G. Bartholomew, S. E. Beavan, S. M. Wittig, J. J. Longdell, and M. J. Sellars, "Optically addressable nuclear spins in a solid with a six-hour coherence time", Nature **517**, 177–180 (2015).

2

Rare Earth Ion Doped Crystals for Frequency Multiplexed Quantum Repeaters

Rare-earth-ion-doped materials provide a promising platform for creating good quantum memories. In the context of frequency-multiplexed quantum repeaters, their large ensembles of stationary ions with inhomogeneously broadened absorption lines and easily addressable spin and optical transitions with long coherence times make for a suitable platform to create an efficient light-matter interface. In this chapter, first, we discuss the essential quantum memory requirements to use in frequency-multiplexed quantum repeater architecture and provide background on what makes a good optical quantum memory. Second, we discuss the important optical properties of rare-earth ions in view of quantum memory. Then, we introduce several useful and widely-employed spectroscopic tools and techniques, which will prepare the readers for the spectroscopic investigations described in subsequent chapters. Finally, we delve into the atomic frequency comb (AFC) quantum memory protocol and its characteristics to provide the necessary background for the quantum storage demonstrations performed in chapters 3 and 5.

2.1. FREQUENCY MULTIPLEXED QUANTUM REPEATERS

In the previous chapter, we discussed how a quantum repeater can ultimately overcome the distance barrier in order to distribute entanglement in globe-spanning quantum communication. There we have considered a highly idealized setting of a quantum repeater, where the main components, namely the entangled photon pairs sources, the quantum memory, and the Bell-state measurements consisting of beam splitters and photon detectors were assumed to be noise-free and free of errors. However, in practice, this is definitely not the case. Limited detector efficiency, detector dark counts (i.e. a click in a detector when no photon is detected), and noise from the source (which arises from the emission of multiple-photon pairs when the source is probabilistic in nature) need to be considered when constructing a quantum repeater. These imperfections deteriorate the repeater performances in terms of entanglement distribution rate as well as the fidelity of the quantum state. A lot of improvements were proposed over the years and a very promising approach is to incorporate multiplexing [1, 2]. It helps to achieve a reasonably higher entanglement distribution rate against small rates caused by the need to wait for feed-forward information.

Multiplexing boosts the entanglement distribution rate in a quantum repeater. It overcomes the problem of having a small success probability of generating entanglement in an elementary link by attempting to generate entanglement multiple times in a single round. This can be done using various degrees of freedom of the photons such as temporal modes (time bin), spectral modes (frequency bin), or spatial modes (orbital angular momentum states of photons). In this thesis, we will focus on spectral multiplexing [3, 4].

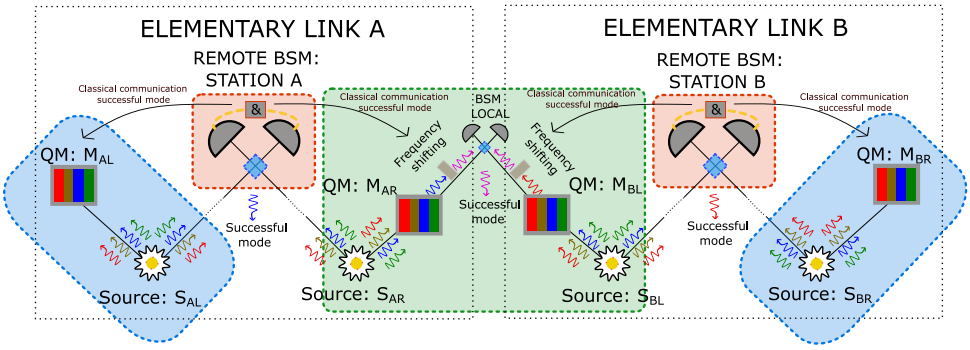

Figure 2.1: **Frequency multiplexed quantum repeater architecture:** A quantum repeater based on absorptive quantum memories (QM) and entangled photon-pair sources (Bell-pairs). BSM indicates the Bell-state measurement which is necessary to establish entanglement in a heralded manner across elementary links and to extend it over the entire communication channel. The figure is adapted from [5].

In the **frequency multiplexed quantum repeater architecture** proposed by Sinclair et al. [3] and described in Figure 2.1, each elementary link is composed of two frequency-multiplexed entangled photon pair sources (PPE) capable of generating entangled photon pairs at different spectral modes (frequency bins), two multimode quantum mem-

ories (QM) capable of storing photons simultaneously in different spectral modes, a frequency-resolved Bell-state measurement (BSM) at the center of each elementary link capable of heralding the entanglement between two frequency-multiplexed quantum memories, and a non-frequency multiplexed BSM that allows extending entanglement across neighboring elementary links. In this scheme, a frequency multiplexed source generates many pairs of entangled photons in different spectral bins. One member per pair from each spectral mode is simultaneously stored in a multimode quantum memory and the second member from each spectral mode is sent over a 'quantum channel' to the center of the link where it meets a member of an entangled pair generated at the other end of this link. The two photons' joint state undergoes a Bell-state measurement (BSM) on each spectral mode, and the result of a successful BSM is communicated over a 'classical channel' back to the end-points to herald the establishment of entanglement of two adjacent quantum memories in an elementary link (feed-forward based mode mapping). Finally, to establish entanglement between the endpoints of the entire repeater link, the stored photons (which occupy random spectral modes) are recalled from the neighboring memories and subjected to a local BSM at the intersection of neighboring elementary links. The local BSM must be preceded by adjustable frequency shifts and spectral filtering to guarantee indistinguishability.

On the other hand, a repeater that employs **temporal multiplexing** assumes all qubits to feature the same spectrum (spectral modes) but to arrive at different times in the memory and at the remote BSM (i.e. in different temporal modes). In contrast to the spectral multiplexing strategy, an on-demand quantum memory is employed in this repeater scheme. So all the stored qubits in the memory are recalled on demand, which requires varying the storage time in order to satisfy indistinguishability for joint Bell-state measurement.

There are several factors or a set of figures of merit to consider when building a quantum memory device, including fidelity, bandwidth, multiplexing capacity, efficiency, storage time, operational wavelength, etc. All of these performance parameters define the state-of-the-art and guide development. It is important to note that the figures of merit which quantify the memory performance often depend on the task. Below we introduce these figures of merit:

- **Fidelity** is a measure of how well the quantum state is preserved in the quantum memory. In other words fidelity quantifies how closely the output quantum state from the quantum memory is to the input quantum state; it is defined as the overlap of the quantum state of the re-emitted photon $|\psi_{\text{out}}\rangle$ with the input photon $|\psi_{\text{input}}\rangle$. Assuming both states are pure, fidelity is defined as $|\langle\psi_{\text{input}}\,|\,\psi_{\text{output}}\rangle|^2$. This is often called conditional fidelity because it is conditional on the re-emission of a photon. In terms of density matrices, it can be written as

$$F = tr(\rho\rho^{'}). \tag{2.1}$$

  where ρ and $\rho^{'}$ are the density matrices of the input quantum state and the output quantum state.

For a device to be identified as a “quantum" memory, the fidelity must exceed the limit of a “classical" counterpart of the memory for single qubits, which corresponds to 2/3 [6].

- **Efficiency:** A quantum memory’s efficiency is the probability of re-emission given that a photon arrived at the memory. It describes the combined probability of storage and retrieval from the quantum memory.

  Although unit efficiency is desired, in practice, it is impossible to reach unit efficiency. In a quantum repeater-based entanglement distribution protocol, a highly efficient quantum memory translates into a higher entanglement establishment rate. It is shown in [7] that quantum memories with 90% efficiency are sufficient to build a practical quantum repeater that would outperform the direct transmission through optical fibers.

- **Storage time:** Storage time of a quantum memory is defined as the time difference between the absorption and re-emission of the photons carrying the quantum state. In temporally multiplexed quantum repeater-based entanglement distribution protocol, the entangled states must be stored in the quantum memories until entanglement is established in the neighboring links. In frequency multiplexed quantum repeater protocol, the minimum storage time of the quantum memory has to be equal to the time it takes for the photons to travel toward the center of the elementary link and for the feed-forward signal of the successful BSM operation to travel back. Long storage time makes long transmission distance possible and could hold the system longer for synchronization. For example, 500 μs of storage time is sufficient enough for a 100 km long elementary link length. For the memories that we consider in this thesis, the storage time is inherently connected with efficiency due to time-dependent decoherence. The longer the storage time, the smaller the collective atomic coherence. Thus, the atoms may not all coherently participate in re-emission, thus reducing the retrieval probability.

- **Bandwidth:** The Bandwidth of a quantum memory is the maximum spectral width over which the memory can store the quantum state efficiently. It dictates the communication rates achievable in a quantum repeater. High bandwidth quantum memory with multi-mode capacity is necessary since it improves the quantum information transmission rate. Since larger bandwidth corresponds to a shorter duration of qubits in time, the higher the bandwidth of the memory, the higher the entanglement distribution rate. Quantum memories with several GHz orders of bandwidths are desirable to align with classical communication standards.

- **Multiplexing capacity:** Sometimes referred to as multimodality or multimode capacity. It bounds the number of qubits that can be stored simultaneously in the quantum memory. Even though spectral multiplexing has been given more focus in this thesis, the multiplexing can also be achieved in other degrees of freedom such as temporal multiplexing - with a train of input photonic states, spatial multiplexing - where orbital angular momentum states are utilized. The temporal multiplexing capacity is approximately equal to the ratio of the storage time to the qubit duration. In other words, it is the ratio between the memory bandwidth to

the spectral width of the qubit [8]. The spectral multiplexing capacity is approximately the ratio between the total memory bandwidth (or the absorption window) to the bandwidth per spectral channel. It is upper bounded by the inhomogeneous broadening of the transition for storage.

- **Operation wavelength:** The operating wavelength of the quantum memory depends on the available transition of the material. Various materials have been explored and used as optical quantum memories, with operating wavelengths ranging from visible to telecom-wavelength. It is desirable to have quantum memories which can operate in the telecom-wavelength range because they can be integrated easily with the existing low-loss telecommunication infrastructure but it is not clear yet which wavelength is the best choice. Furthermore, the operating wavelength of a quantum memory also depends on the available photon sources and detectors.

- **Complexity and practicality:** In practice, it is desirable to have a quantum memory that has minimal complexity and should not require bulky and expensive resources. The integration of quantum memories with the existing photonic fiber-optic communication technologies needs to be simple. For that purpose, fiber-integrated, telecom wavelength-compatible quantum memories are suitable. In addition to these requirements, robustness and compactness are other important factors. Hence, the development of solid-state quantum memory, as opposed to laser-cooled atoms, or warm atomic vapor memories, is highly desirable.

2.2. RARE-EARTH-ION-DOPED (REID) CRYSTALS FOR QUANTUM MEMORY

According to the International Union of Pure and Applied Chemistry (IUPAC), in the periodic table, rare-earth elements belong to a class of 15 elements (from Lanthanum (atomic number 57) to Lutetium (atomic number 71)) known as **lanthanides**, including scandium and yttrium. Despite the name, most of the rare-earth elements are not really rare, but they tend to occur together in nature and are difficult to separate. The first rare earth element, yttrium, was named after the village in Sweden where it was found, Ytterby. Some of the other rare-earth elements were also named in a similar manner or after the scientists who discovered or elucidated them. When doped into inorganic crystals, these atoms usually become triply positively charged ions whose common property is their partially filled $4f$ electronic shell. The trivalent lanthanide ions have a Xenon-like electronic shell structure -$1s^2 2s^2 2p^6 3s^2 3p^6 4s^2\ 3d^{10} 4p^6 5s^2 4d^{10} 5p^6$- plus N additional electrons on the $4f$ shell, where N varies from 0 for lanthanum to 14 for lutetium. The electrons in these shells remain spatially separated from the electrons involved in bonding to the host crystal. Moreover, the asymmetries in the crystal field structure cause mixing of the wave functions for electrons of this shell that weakly permit transitions that would otherwise be forbidden via selection rules. The $4f^N - 4f^N$ transitions are those utilized for absorptive optical quantum memories. The rare-earth elements, which are listed in Table 2.1:

Rare-earth-ions (REIs) have very similar properties. Due to their unique spectro-

Table 2.1: List of rare-earth elements with their electronic configuration in the tri-positive state and the corresponding ground state label in the Russell-Saunders notation.

Atomic number	Rare-earth element	Electronic configuration of the trivalent rare earth ion (RE^{3+})	Ground state (Russell-Saunders notation)
21	Sc Scandium	$3d^0$	$^1S_0$
39	Y Yttrium	$4d^0$	$^1S_0$
57	La Lanthanum	$4f^0$	$^1S_0$
58	Ce Cerium	$4f^1$	$^2F_{5/2}$
59	Pr Praseodymium	$4f^2$	$^3H_4$
60	Nd Neodymium	$4f^3$	$^4I_{9/2}$
61	Pm Promethium	$4f^4$	$^5I_4$
62	Sm Samarium	$4f^5$	$^6H_{5/2}$
63	Eu Europium	$4f^6$	$^7F_0$
64	Gd Gadolinium	$4f^7$	$^8S_{7/2}$
65	Tb Terbium	$4f^8$	$^7F_6$
66	Dy Dysprosium	$4f^9$	$^6H_{15/2}$
67	Ho Holmium	$4f^{10}$	$^5I_8$
68	Er Erbium	$4f^{11}$	$^4I_{15/2}$
69	Tm Thulium	$4f^{12}$	$^3H_6$
70	Yb Ytterbium	$4f^{13}$	$^2F_{7/2}$
71	Lu Lutetium	$4f^{14}$	$^1S_0$

scopic characteristics, the rare-earth-ion-doped crystals have attracted a lot of attention in the past decade as promising candidates for many optical applications including fluorescent lamps, solid-state lasers [9], optical amplifiers [10] in fiber optics, in quantum computing [11, 12], optical data storage [13] and quantum memories [14]. This is often because of their very long coherence lifetimes at cryogenic temperature [15–18].

The similarity among rare-earth elements comes from the fact that the $4f$ shells are not completely filled and the $4f$ electrons do not take part in binding and chemical reactions. The $5s$ and $5p$ electrons have lower energies than the $4f$ electrons therefore electrons fill the $5s$ and $5p$ before the $4f$ shell (**Aufbau principle and Hund Rule**). On the other hand, the $4f$ shell has a lower principal quantum number which keeps its radial charge distribution closer to the nucleus than the $5s$ and $5p$ shells (shown in Figure 2.2). Thus, the $4f$ electrons are shielded by electrons in the $5s$ and $5p$ closed shells from interacting with ligand electrons and lattice vibrations. This is called the **screening effect**, which prohibits the interaction of $4f$ electrons with the dynamic crystal environment, and leads to very sharp spectral lines, e.g. optical transition linewidths in the sub-kHz range which corresponds to milliseconds-long optical coherence time [16, 18, 21]. By employing dynamical decoupling, hyperfine transitions' decoherence could be reduced to observe long spin coherence times of around 6 hours at cryogenic temperatures [17]. As a result, the rare-earth ions exhibit unique characteristics which make them valuable for many optical applications such as solid-state lasers [9], optical amplifiers [10], and optical data storage [13].

Figure 2.2 shows a plot of the theoretical probability distribution of the outer electronic shells of Gd^+, calculated using the Hartree Fock method. The $4f$ shell is seen to

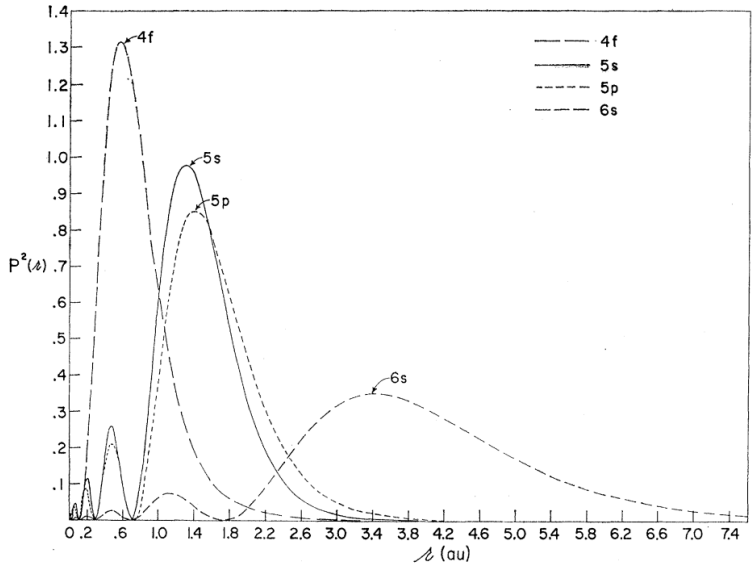

Figure 2.2: **Electron distribution for Gd^+**: The radial charge density as a function of radius r for the $4f$, $5s$, $5p$ and $6s$ shells of Gd^+, calculated by Freeman and Watson [19]. In the trivalent state of rare-earth ions, the $6s$ shell is completely empty but the $5s$ and $5p$ shells are fully populated.

Interaction type	Energy (GHz)
Configuration splitting $4f^N$ to $4f^{N-1}5d^1$	10^6
Splitting within the $4f^N$ configuration:	
- Non central electrostatic field	10^5
- Spin-orbit coupling	10^4
- Crystal-field interaction	10^3
- Hyperfine splitting	$10^{-2} - 1$
- Superhyperfine interaction (ion-ligand)	$10^{-3} - 10^{-1}$

Figure 2.3: **Typical energy scales involved in the rare-earth level structure:** Table adapted from [20]. The splittings down to the spin-orbit coupling are properties of the free ion, while the hyperfine splitting and superhyperfine splitting concern the spin Hamiltonian.

be closer to the nucleus than the $5s$ and $5p$ shells. For this reason, the electronic level structure of rare-earth ions can be approximated by the free-ion energy levels. The interaction with the host crystal ("crystal field") can be treated as a perturbation of the free ion.

The total Hamiltonian of any rare-earth ion can be divided into three terms, ordered with decreasing energy scales

$$\mathcal{H} = \mathcal{H}_{FI} + \mathcal{H}_{CF} + \mathcal{H}_{spin} \tag{2.2}$$

where $\mathcal{H}_{FI}$ is the free-ion Hamiltonian, $\mathcal{H}_{CF}$ the crystal-field Hamiltonian, and $\mathcal{H}_{spin}$ the spin Hamiltonian. A typical energy scale involved in the rare-earth level structure is shown in Figure 2.3. In the next paragraph, we will focus on each term of the Hamilto-

nian separately.

2.2.1. ENERGY LEVELS

The electronic configuration of an atom is determined by four quantum numbers (n, l, m_l, m_s): its principal quantum number n, its angular momentum quantum number l ($0 \leq l \leq n$ - 1), its magnetic quantum number m_l ($-l \leq m_l \leq l$) and its spin quantum number m_s = $\pm 1/2$. Each (n, l) energy level is called a configuration. Here we focus of the $4f$ configuration with n = 4 and l = 3 of REI-doped system. Thulium atoms (Tm) have the atomic number 69. They lose usually 3 electrons and become Tm^{3+} when bonded to oxygen. The electronic configuration of Tm^{3+} is [Xe]$4f^{12}$, i.e. there are twelve electrons in the $4f$ shell. For the understanding of the energy levels, there are many interactions that should be considered in the Hamiltonian, which can be written as

$$\mathcal{H} = [\mathcal{H}_0 + \mathcal{H}_C + \mathcal{H}_{SO}] + \mathcal{H}_{CF} + [\mathcal{H}_{HF} + \mathcal{H}_Q + \mathcal{H}_{eZ} + \mathcal{H}_{nZ}] \tag{2.3}$$

where, $\mathcal{H}_{FI} = \mathcal{H}_0 + \mathcal{H}_C + \mathcal{H}_{SO}$ and $\mathcal{H}_{spin} = \mathcal{H}_{HF} + \mathcal{H}_Q + \mathcal{H}_{eZ} + \mathcal{H}_{nZ}$. Further detailed analysis can be found in [9, 22].

Free-ion Hamiltonian $\mathcal{H}_0$: The free-ion Hamiltonian $\mathcal{H}_0$ is the sum of the kinetic energy and the potential energy of the electrons in the field of the nucleus. The Hamiltonian describing an N-electron ion without any external field can be decomposed as follows:

$$\mathcal{H}_0 = -\sum_{i=1}^{N} \frac{\hbar^2}{2m} \nabla_i^2 - \sum_{i=1}^{N} \frac{Ze^2}{r_i} \tag{2.4}$$

It is purely radial and hence does not affect the energy level structure. Any nonspherical electronic interactions are taken as perturbations to the spherically symmetric potentials. Central field approximation is used which is a conventional approach to solve the Schrodinger equation for N-electron atomic system and to evaluate the energy levels.

The Coulomb interaction Hamiltonian ($\mathcal{H}_C$): The Coulomb repulsion between pairs of electrons can be written as

$$\mathcal{H}_C = \sum_{i<j}^{N} \frac{e^2}{r_{ij}} \tag{2.5}$$

The repulsive interaction between the electrons removes the degeneracy of the $4f$ electrons in the ground and excited terms which are labeled as ^{2S+1}L, each of which is $(2S+1)(2L+1)$-fold degenerate. For example, $\mathcal{H}_C$ breaks the degeneracy $4f^N$ level into 14!/(14-N)!N! levels. But note that, this rule does not apply for Lu^{3+} since N is equal to 14 for its $4f^N$ orbital. The total orbital angular momentum L, total spin angular momentum S, and the net angular momentum J determine the spectral terms of the ground and excited states. While J and S are specified numerically, L is conventionally specified with letters in the following manner; L = 0, 1, 2, 3, 4, 5, ... ≡ S, P, D, F, G, H,... $\mathcal{H}_C$ term dominates the Hamiltonian in light atoms whose radius is small hence the electrostatic interaction is strong.

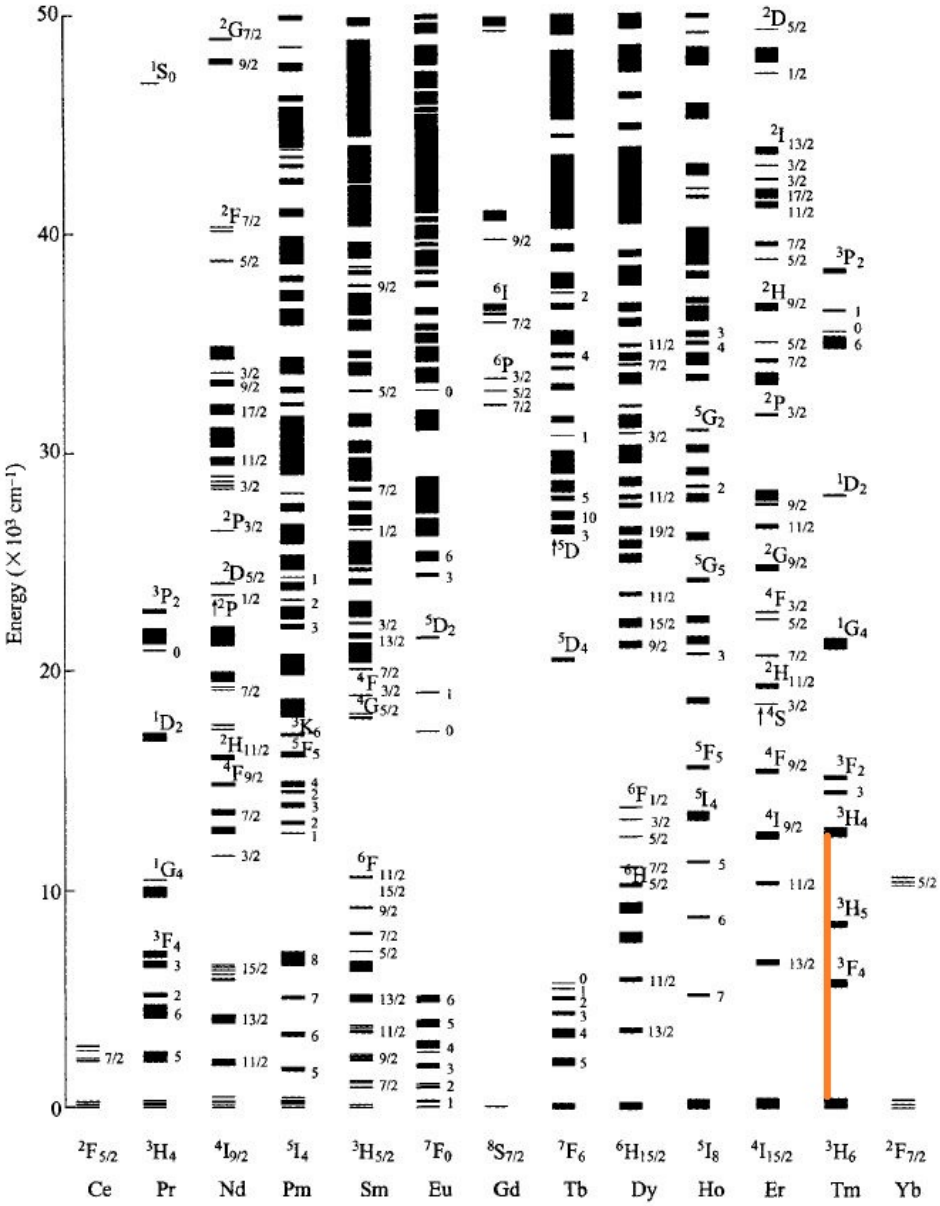

Figure 2.4: Dieke diagram of energy levels of different REI elements doped into Lanthanum Fluoride. The transition energies are calculated from free ion and crystal field terms of the ion Hamiltonian. The orange arrow indicates the optical transition in thulium for this work. The figure is reproduced from [9].

The spin-orbit interaction Hamiltonian $\mathscr{H}_{SO}$: The motion of electrons in the orbit around the nucleus creates a magnetic field that interacts with the electron spins, which

can be written as

$$\mathcal{H}_{SO} = \sum_{i=1}^{N} \xi(r_i)\, \boldsymbol{l}_i \cdot \boldsymbol{s}_i \tag{2.6}$$

It is called the spin-orbit interaction ($\mathcal{H}_{SO}$) and splits the Coulomb interaction energy term into manifolds, where each level is a $(2J+1)$ degenerate multiplet labeled in **the Russell-Saunders notation** ${}^{2S+1}L_J$. The LS coupling scheme applies, however, better for light atoms than heavy atoms. When the atomic number Z increases, the spin-orbit coupling increases much faster than the Coulomb interaction. In rare-earth ions, they are typically of the same magnitude. As a consequence, L and S are not good quantum numbers anymore and the LS coupling scheme should be replaced by the so-called intermediate coupling scheme which includes the mixing of energy terms with different L and S by the spin-orbit interaction [9]. The final energy levels are $(2J+1)$ degenerate multiplets characterized by quantum number J only. Nevertheless, rare-earth energy levels are usually still labeled using the Russell-Saunders notation ${}^{2S+1}L_J$. This remains accurate for low energy states which are relatively pure in L and S, as ground multiplets are usually greater than 90% pure LS states. This is not accurate anymore to describe high-energy states as discussed in [23]. In the many-electron free ion case when the $4f$ shell is less than half full, the ground state manifold can be built with the Hund rule, where $J = L - S$. In Tm^{3+} the ground state manifold is ${}^3H_6$.

Among the three interactions mentioned above the spin-orbit term is relatively small and can be treated as a perturbation. However, the Coulomb interaction term can not be neglected as this repulsion term couples pairs of electrons, and the motion of each electron depends on the other $N-1$ electrons. Due to the screening effect, any other interactions with the ions can be considered as perturbations of the free ion case, which is represented by the Hamiltonians on the right bracket.

The crystal field interaction Hamiltonian $\mathcal{H}_{CF}$: When embedded in a crystal, the rare-earth ion's environment produces electric fields which break the spherical symmetry of the electronic structure developed. The electric field of the crystalline environment splits the ionic energy levels. Nevertheless, the interaction of the electrons with the crystal field ($\mathcal{H}_{CF}$) is weaker than the spin-orbit interaction thus the effect is mostly localized as perturbations within the single manifolds. It partially or completely removes the degeneracy on each J manifold which can then be split into a maximum of $2J+1$ levels, written as ${}^{2S+1}L_J$ (n), n = 0,...,2J+1. The number of crystal field levels, as well as the magnetic properties of rare-earth ions, depends on the number of electrons in the $4f$ shell. If it is an odd number, the ion, called **Kramers ion**, has a larger magnetic moment due to the unpaired electron. For example Er^{3+} ion, which has 11 electrons in the $4f$ shell. Ions with an even number of electrons are called **non-Kramers ions**. For example Tm^{3+}, which has 12 electrons in the $4f$ shell. For those in sites with lower than axial symmetry, it results in a "*quenching*" of the angular momentum. In non-Kramers ions, all crystal field levels are split while a 2-fold degeneracy remains in the case of Kramers ions.

The hyperfine interaction Hamiltonian $\mathcal{H}_{HF}$: This is the interaction between the nuclear spin momentum I and the effective magnetic field induced by the electronic

angular momentum S. For singlets, the first-order hyperfine interaction vanishes, and only the second-order effect is considered. The splittings of energy levels due to this Hamiltonian are often referred to as the *hyperfine splittings*.

Often the interaction between the nuclear spin and the magnetic field induced by the spin of the electron is referred to as hyperfine interaction ($\mathcal{H}_{HF} \propto \vec{S}\cdot\vec{I}$) whereas the interaction between the electronic spin of the ion and the magnetic field produced by the nuclear spin of the host element is referred to as *superhyperfine interaction* ($\mathcal{H}_{SHF} \propto \vec{S}\cdot\vec{I_{host}}$).

The quadrupole interaction Hamiltonian $\mathcal{H}_Q$: The quadruple interaction is due to the effect on a nuclear spin (with $I \geq 1$) caused by the interaction between the angular momentum of the electron $\vec{L}$ and the nuclear quadruple momentum $\vec{Q}$ i.e $H_Q \propto \vec{Q}\cdot\vec{L}$. The quadrupole interaction term is similar to the second-order nuclear hyperfine interaction term. The two Hamiltonians can be written together as an effective Hamiltonian

$$\mathcal{H}_{eff} = -g_J^2\mu_B^2 \boldsymbol{H}\cdot\Lambda\cdot\boldsymbol{H} - \left(2A_{\mathbf{J}}g_J\mu_B\boldsymbol{H}\cdot\Lambda\cdot\boldsymbol{I} - \mathcal{H}_Z\right) - \left(A_{\mathbf{J}}^2\boldsymbol{I}\cdot\Lambda\cdot\boldsymbol{I} + \mathcal{H}_Q\right) \tag{2.7}$$

where $\boldsymbol{H}$ is the applied magnetic field, $\boldsymbol{I}$ is the nuclear angular momentum operator, g_J is the Lande g-factor and μ_B is the Bohr magneton, and $A_{\mathbf{J}}$ is the magnetic hyperfine constant. Here Λ is the tensor describing the second-order interactions in the system. The first term in the equation is the *quadratic electronic Zeeman shift*, the second term is called the *enhanced nuclear Zeeman Hamiltonian* due to the enhancement of coupling to the second order hyperfine interaction and the last term is the *effective quadrupolar Hamiltonian* which is the combination of the second order hyperfine and pure quadrupole interactions. This term is also known as the *pseudo-quadrupolar interaction*.

The Zeeman interaction Hamiltonian $\mathcal{H}_Z$: The last two Hamiltonians, **electronic Zeeman effect** $\mathcal{H}_{eZ}$ and **nuclear Zeeman effect** $\mathcal{H}_{nZ}$ exist only when an external magnetic field is applied. The external field lifts the $\pm$ degeneracy in the hyperfine levels and for Kramers ions, it splits each level into two. The magnitude of the splitting is directly proportional to the amplitude of the applied field. $\mathcal{H}_{eZ}$ represents the interaction between the spin of the electron and an externally applied magnetic field. $\mathcal{H}_{nZ}$ represents the interaction due to the interaction between the nuclear spin and an externally applied magnetic field. Non-Kramers ions such as Tm^{3+} can exhibit an enhancement in the nuclear Zeeman interaction, due to the second-order perturbation created by the electronic Zeeman and hyperfine interactions also known as *pseudo-nuclear Zeeman interaction*.

2.2.2. HOMOGENEOUS AND INHOMOGENEOUS BROADENING

Generally, a spectral linewidth for a given optical transition of a two-level system originates from two main contributions: homogeneous and inhomogeneous linewidth broadening. The homogeneous broadening is due to the intrinsic properties of rare-earth ions. This is mainly because of the finite lifetime of the excited state but can also include other decoherence phenomena which broaden the observed linewidth. While the extrinsic properties such as strain and stress in the crystalline environment usually lead to inho-

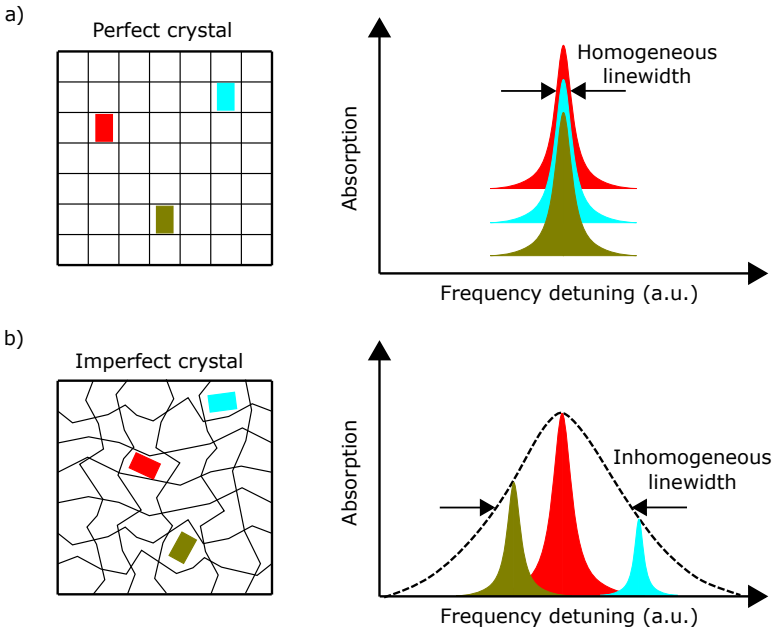

Figure 2.5: a) Homogeneous linewidth: absorption profile of a perfect crystal doped with REIs. b) Inhomogeneous linewidth: absorption profile of an imperfect crystal doped with REIs. The imperfections may be caused by, for example, stress and strain in the host crystal. The extreme case of an imperfect crystal can be seen as an amorphous lattice that possesses a large inhomogeneous linewidth. The figure is reproduced from [24, 25].

mogeneous broadening.

Homogeneous broadening accounts for the linewidth of the transition of each individual rare-earth ion. It refers to the spectral linewidth of a single ion's absorption and emission. This is the result of the broadening of the optical transition due to the finite lifetime of the excited state. Homogeneous linewidth can be affected by decoherence phenomena happening in the crystalline environment of the REI spin, for example, the ion-phonon interaction, the ion-ion interaction, fluctuating nuclear or electron spins, the ion spin-nuclear spin interaction, etc. In short, homogeneous broadening arises from dynamic processes and the dephasing of ions at the electronic levels. Hence it is the same for all ions. It can be defined as

$$\Gamma_h = \frac{1}{2\pi T_1} + \frac{1}{\pi T_2^*} = \frac{1}{\pi T_2} \tag{2.8}$$

where T_1 is the **population decay time/excited state lifetime**, T_2^* is the **pure dephasing time (ensemble-averaged transverse dephasing time)** and T_2 is the **optical coherence time**. The T_1 lifetime describes how long the atom stays in the excited state before it decays to the ground state, while the coherence time T_2 describes how long the superposition state keeps its phase information. Since the phase information is lost if the system decays to its ground state, the population lifetime T_1 sets the upper limit of the coher-

ence time, $T_2 \leq 2T_1$. The screening effect due to the $5s$ and $5p$ shell minimizes the broadening of the absorption line by diminishing the phonon-ion interaction in the crystalline lattice at liquid helium temperatures. Phonon interaction dominates at higher temperatures and broadens the linewidth.

Inhomogeneous broadening: When doped into a perfect inorganic crystal, each individual rare-earth ion has a well-defined and identical center frequency and a narrow homogeneous linewidth. However, because of the size mismatch between the dopant ions and the host ions, the doping distorts the crystal lattice randomly and the individual ions are located in slightly different local environments and experience different crystal fields. This causes a static random shift of the resonance frequency of the ions, resulting in an absorption profile that is much wider than the homogeneous linewidth, Γ_h. This is referred to as the inhomogeneous linewidth Γ_{inh}.

Such static resonance frequency shifts can have several origins. The magnetic dipole-dipole interaction shifts the transition frequency of a REI spin and causes inhomogeneous broadening of the REI ensemble. Dipole interactions are of two types: either with the nuclear spins of the host crystal or with paramagnetic impurities. It can be shown that dipolar coupling leads to a Lorentzian lineshape. Its fullwidth-at-half-maximum (FWHM) linewidth is called the **dipolar linewidth**. Another less intuitive broadening mechanism is the frequency shift caused by inhomogeneous electric field gradients in the crystal (due to **charge defects**) [20]. Figure 2.5 illustrates how this inhomogeneous broadening happens. The inhomogeneous linewidth varies from host to host and depends on many factors, such as doping concentration, crystal quality, external static pressure, etc. Typically the inhomogeneous linewidth can be from a few tens of MHz to a few THz. For the crystal used in this thesis, 1% Tm^{3+}:YGG, the typical inhomogeneous linewidth is 50-60 GHz. Since the inhomogeneous linewidths ($\approx$ GHz) are typically much wider than the homogeneous linewidths ($\approx$ kHz), it is possible to address different ensembles of ions individually using a narrow-linewidth laser at different frequencies, e.g., by spectral hole burning, to be discussed in the subsequent chapter. This offers attractive possibilities for data storage [13], which is also the topic of discussion in the next chapter.

2.2.3. SPIN RELAXATION AND SPECTRAL DIFFUSION

Optical dephasing/decoherence mechanisms in the time domain translate into linewidth broadening in the frequency domain. Therefore, the decoherence mechanisms that cause the reduction of the optical coherence time T_2 will broaden the homogeneous linewidth Γ_h. Two main processes responsible for optical dephasing are **phonon-ion interactions** and **spin-flips**. Phonon-ion interactions lead to the relaxation of the population from spin levels through interaction with lattice phonons, which is known as **spin-lattice relaxation**. This can occur via direct (resonant) or indirect (Raman) processes. The REI spins are also affected due to the spin-spin interactions with the host ions. Any spin changes of the surrounding ions (spin-flips) will affect the optical coherence time of the target REI spin through spin-spin interactions. Because of these processes, the dephasing behavior of the target REI spin will change with time, which is known as **spectral diffusion**. Taking spectral diffusion into account the effective homogeneous linewidth

can be written as [26, 27]

$$\Gamma_{h(eff)} = \Gamma_{population} + \Gamma_{spin-phonon} + \Gamma_{spin-spin} + \Gamma_{TLS} + \Gamma_{ISD} \tag{2.9}$$

where the contribution of each term to the effective homogeneous linewidth $\Gamma_{h(eff)}$ is explained below:

- **Population lifetime limited linewidth $\Gamma_{population}$:** The natural spectral linewidth $\Delta\nu$ of a dipolar emission is "Fourier" limited to $\frac{1}{2\pi\tau}$, due to the finite lifetime τ, of the excited state, owing to the energy-time uncertainty principle. This is the fundamental limit of the spectral linewidth.

- **Spin-phonon interaction limited linewidth $\Gamma_{spin-phonon}$:** A theory for spin-lattice relaxation at low temperatures, e.g. at or below liquid helium temperatures, was first developed by Orbach in 1961 [28]. The treatment is based on the assumption that relaxation is facilitated by fluctuations in the crystal's electric field, which is caused by phonons. Orbach's treatment distinguishes between Kramers ions (e.g. Er^{3+}) and non-Kramers ions (e.g. Tm^{3+}). When out of thermal equilibrium, spins relax by exchanging energy with a thermal bath at temperature T_0. There are two thermal baths with which spins can exchange energy: either they relax by emitting microwave photons- known as **radiative relaxation**, or they relax by emitting phonons- known as **non-radiative relaxation** [29].

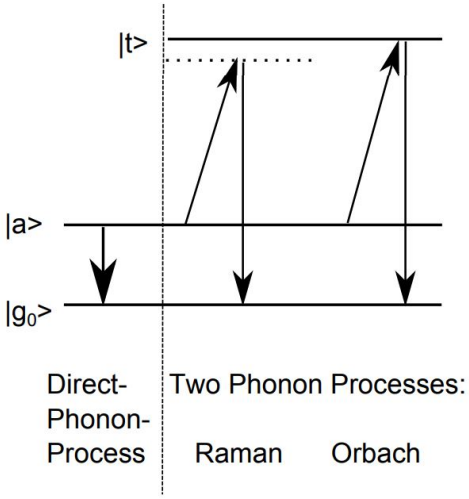

Figure 2.6: **Different phonon processes** facilitating transitions between $|a\rangle$ and $|g_0\rangle$ (figure adapted from [30]), each of the processes are described in detail in the main text.

Let us consider two Zeeman energy-levels (spin states) $|g_0\rangle$ and $|a\rangle$) under a magnetic field H with Zeeman energy $\hbar\omega = g_{eff}\mu_B H$. The populations of each level are called n_g and n_a respectively. They are coupled to a bath of infinite heat capacity

such that its temperature is always at T_0. Note that in the case of phonons, this assumption is not always valid. In fact, the heat capacity of phonons is often smaller than the one of the spins and this can lead to an effect called phonon bottleneck, where the phonon temperature increases due to spin relaxation.

1. Direct process: We first consider the direct process where each spin exchanges one resonant phonon or photon with the bath. The population difference between the two spin levels evolves according to the following differential equation:

$$\frac{d\left(n_g - n_a\right)}{dt} = (w_- + w_+)\left[\left(N_g - N_a\right) - \left(n_g - n_a\right)\right] \tag{2.10}$$

where w_+ and w_- are the transition rates from $|g_0\rangle$ to $|a\rangle$ and from $|g_0\rangle$ to $|a\rangle$ respectively and N_g and N_a are the equilibrium level populations. The transition rates are related to Einstein coefficients with

$$\begin{aligned} w_+ &= B\rho \\ w_- = A + B\rho &= B\rho e^{\frac{\hbar\omega}{k_B T_0}} \end{aligned} \tag{2.11}$$

where A is the coefficient of spontaneous emission, B is the coefficient of stimulated absorption or emission, ρ is the energy density of the bath, and k_B is the Boltzman constant.

$$\rho d\omega \propto \frac{\omega^3}{v^3} \frac{d\omega}{\exp\left(\hbar\omega / k_B T_0\right) - 1} \tag{2.12}$$

v is either the velocity of light ($\approx 3 \times 10^8$m/s) or the velocity of phonons ($\approx 3 \times 10^3$m/s). The solution of Equation 2.10 is thus

$$n_a - n_g = (N_a - N_g) + [(n_a - n_g)_{t=0} - (N_a - N_g)]e^{-t/T_1} \tag{2.13}$$

$$\frac{1}{T_1} = w_+ + w_- = A + 2B\rho \propto \frac{\omega^3}{v^3} B \coth \frac{\hbar\omega}{2k_B T_0} \tag{2.14}$$

Here T_1 is the spin state lifetime.

The rate of direct phonon processes for non-Kramers ions, Eq.2.14 modifies to [29]

$$1/T_1 \propto H^2 T_0 \tag{2.15}$$

for $g\mu_B H << k_B T_0$

$$1/T_1 \propto H^3 \coth\left(\frac{g\mu_B H}{2k_B T_0}\right) \tag{2.16}$$

otherwise.

For Kramers ions, the unpaired electron makes them more susceptible to interactions with the environment. This leads to different phonon coupling strengths and different dependencies of the relaxation rates on external factors such as the magnetic field. However, the processes themselves are the same, and Eq.2.14 transforms to [29, 30]

$$1/T_1 \propto H^4 T_0 \tag{2.17}$$

for $g\mu_B H << k_B T_0$

$$1/T_1 \propto H^5 \coth\left(\frac{g\mu_B H}{2k_B T_0}\right) \tag{2.18}$$

otherwise.

The characteristic temperature and magnetic field dependencies of the direct phonon process (Eq.2.16 and 2.18) can serve to identify Kramers ions and non-Kramers ions. Generally, the direct-phonon process is dominant at low temperatures. At higher temperatures, phonons with higher energy are available and multi-phonon processes become important. The specific temperature at which higher-order processes dominate relaxation strongly depends on the host material.

1.1 Radiative relaxation: The radiative relaxation rate by direct absorption and emission of photons from the electromagnetic radiation field in free space can be written as

$$\frac{1}{T_1} = \frac{\mu_0}{4\pi}\frac{2(g\mu_B/\hbar)^2}{3}\frac{\hbar\omega^3}{c^3}\coth\frac{\hbar\omega}{2k_B T_0} \tag{2.19}$$

In free space, it can be neglected. However, photon emission can be greatly enhanced via the coupling of the spin to a high-quality-factor microwave resonator.

1.2 Non-radiative relaxation: Because radiative relaxation is negligible, spin relaxation in crystals occurs dominantly by the exchange of phonons with the lattice. We now describe qualitatively the mechanism leading to spin relaxation by phonon emission in REIs. Lattice ion vibration leads to a modulation of the crystal field, which couples to the REI magnetic moment via the spin-orbit interaction.

2.Two-phonon processes: In addition to the direct phonon process, REI spin relaxation can occur via two-phonon processes. Two-phonon processes are explained by second-order perturbation theory. Here the spin-lattice potential acts twice upon the involved states and two phonons induce a transition between the initial and final state. Therefore an intermediate level $|t\rangle$ via which the transition takes place must be involved. Figure 2.6 shows the distinction between **direct phonon processes**, **resonant two phonon processes (Orbach processes)**, and **off-resonant two phonon processes (Raman processes)**.

There are two fundamentally different two-phonon processes, distinguished by whether the intermediate level can be populated (**Orbach process**), which is mostly the case if $k_B T_D > \Delta_t$, or the intermediate level is not populated (**Raman process**), and the transitions occur via a virtual level. This process is dominant if $k_B T_D < \Delta_t$. Δ_t is the energy difference between the initial state $|a\rangle$ and the intermediate state $|t\rangle$. T_D is the Debye temperature and $\omega_{max} = k_B t/\hbar$ the largest available phonon frequency in the host material.

2.1 Orbach process: The Orbach process involves a third level $|t\rangle$. If the phonon energy density is higher at its energy Δ_t compared to the Zeeman energy $\hbar\omega$, it will be more likely that, in order to relax from $|a\rangle$ to $|g_0\rangle$, a phonon is first absorbed such that $|a\rangle$ is excited to $|t\rangle$ and then state $|t\rangle$ emits a phonon and relaxes to $|g\rangle$.

The Orbach relaxation rate is

$$\frac{1}{T_1} = R_O \Delta^3 + \frac{1}{e^{\Delta / k_B T_0} - 1} \tag{2.20}$$

2.2 Raman process: The Raman process is a two-phonon process that involves a continuum of states within the phonon energy density. Unlike the Orbach process, it involves virtual phonon states which are not specifically resonant with transitions of the magnetic ion. From this virtual level, a phonon can be emitted again such that the electron spin relaxes to $|g_0\rangle$. This relaxation can be modeled by two separate mechanisms and the Raman relaxation rate has thus two contributions

$$\frac{1}{T_1} = R_R T_0^9 + R_R^{/} (\frac{\hbar\omega}{k_B})^2 T_0^7 \tag{2.21}$$

It is important to note that both two-phonon processes are independent of the magnetic field and can be distinguished using their temperature dependence.

Multi-phonon processes that include the interaction with more than two phonons can be treated in the same way as direct and two-phonon processes. However, we will not consider those cases since we restrict ourselves to applications implemented at and below liquid helium temperatures at which they play an insignificant role.

- **Linewidth limited by spin-spin interaction $\Gamma_{spin-spin}$:** This phenomenon refers to the mutual spin-spin coupling, which can be either the electronic spin-spin or the nuclear spin-spin couplings. When two neighboring REI spins are resonant, they exchange their energy mediated by magnetic dipole-dipole interaction which results in a spin flip-flop. But when two neighboring electronic or nuclear spins are off-resonant with each other, the energy difference between them is supplied by the host nuclear spin. This causes fluctuations of the magnetic field in the surrounding environment of the REI spin, which results in linewidth broadening. For Kramers ions (e.g Er-doped materials), due to their large magnetic dipole moment, spin flip-flops can often degrade the coherence time. To get around this problem a high magnetic field is required to polarize ("freeze") the environmental spins. For non-Kramers ion (e.g Tm-doped materials), on the other hand, due to their quenched electronic spin, flip-flops do not pose a serious threat. Instead, nuclear spin flip-flops can cause linewidth broadening. There are ways to minimize the detrimental effect due to spin flip-flops. Since the magnetic dipole-dipole interaction strength decreases with distance r as r^{-6}, low REI spin concentration and less magnetic impurities in the material help to mitigate the effect of spin flip-flops. Choosing a host material whose elements have small nuclear magnetic moments also helps.

- **Linewidth limited by two-level systems (TLS) interaction Γ_{TLS}:** In a disordered crystal structure, a major contributing mechanism to homogeneous linewidth broadening is the coupling between energy levels of rare-earth ions with Two Level Systems (TLS). In a crystal lattice, phonons represent the quantized lattice vibrational

modes but in an amorphous lattice (irregular crystalline structures, glasses), phonons are replaced by localized vibrational low-energy modes. They can exhibit a double-well-like potential energy structure and, therefore, can be treated as a two-level system (TLS). One or many ions can tunnel between these two energy minima in configuration space, introducing TLS broadening.

- **Linewidth limited by instantaneous spectral diffusion Γ_{ISD}:** Instantaneous Spectral Diffusion, or ISD in short, is a decoherence effect, caused by the presence of intense light. ISD can take place when the optical excitation of a neighboring ion causes magnetic or electric field fluctuations in the REI crystalline environment. It can also be identified as an ion-ion interaction or due to phonon-induced interactions which results in a transition frequency shift of the REI spin, leading to the broadening of the homogeneous linewidth. By lowering the concentration of the dopant ion in the crystal, or by lowering the intensity of the light, one can significantly diminish the influence of ISD.

The next section will provide the background to understand the interaction between light and matter which can help us to probe and measure the underlying decoherence mechanisms discussed above.

2.3. SPECTROSCOPIC TOOLS AND SPECTRAL TAILORING

Light provides us with a unique tool to investigate the properties of matter and to understand the underlying mechanisms that lead to them. This section will discuss various spectroscopic methods and their ability to measure different material properties. The main goal is to provide a set of measurements that allows one to quantify the ability to perform spectral tailoring. This kind of measurement for a broad range of environmental parameters such as temperature, magnetic fields, etc. It is then possible to determine the nature of the underlying processes leading to the observed properties.

2.3.1. SPECTRAL HOLE BURNING

For the investigation of the spectroscopic properties of materials with inhomogeneously broadened absorption lines, we implement a widely known spectroscopic tool known as **spectral hole burning** (SHB). Using a narrowband laser that is resonant with the transition of interest, it is possible to excite a spectrally narrow sub-ensemble of the two-level atoms and transfer the atomic population from the ground to the excited state [31]. This procedure is known as **optical pumping**. Since absorption is proportional to the population difference between the ground and excited state, such an atomic excitation causes a decrease in absorption at the frequency of excitation. This results in a **spectral hole** in the inhomogeneously broadened absorption profile. After the spectral hole has been created, it can be probed by frequency-sweeping the laser over the spectral region of the created spectral hole. In this way, the width and the area of the spectral hole can be measured.

Depending on the lifetime into which the atomic population has been transferred during optical pumping, the spectral hole will decay with different decay constants. If

the lifetime of the spectral hole is on the order of excited level lifetime, it is referred to as a **transient spectral hole**. If the spectral hole is long-lived (>ms), as in the case of most Zeeman or hyperfine or superhyperfine states, it is referred to as a **persistent spectral hole**.

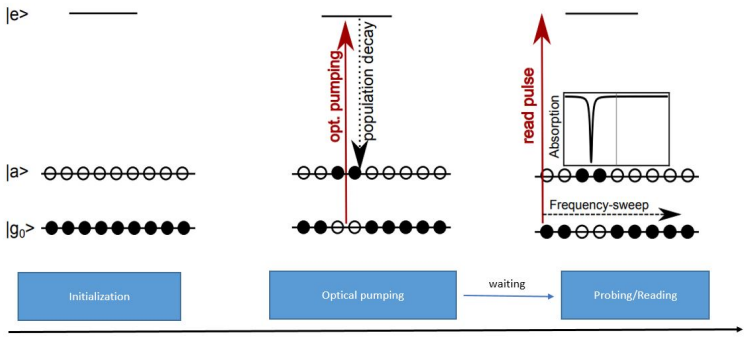

Figure 2.7: **Experimental hole burning sequence:** Frequency-selective optical pumping moves population from $|g_0\rangle$ to $|e\rangle$. It subsequently decays into $|a\rangle$. This creates a spectral hole in the desired transition. After a waiting time, the spectral hole is read by a laser pulse that is swept in frequency over the extent of the spectral hole (Figure is adapted from [30]).

Spectral hole burning is often used to extract the lifetimes of energy levels that are involved in the transition. By measuring the area of the spectral hole, which is proportional to the amount of atomic population absent from the ground state, the lifetimes of the various levels that lie between the excited state and the ground state can be obtained. In case only two levels $|g_0\rangle$ and $|e\rangle$ are involved, the area of the spectral hole will decay exponentially with time. Additional energy levels will produce a multi-exponential decay. The decay times of the individual exponential functions directly correspond to the population lifetimes of the involved energy levels. As an example, for a 3-level system as depicted in Figure 2.7, the decay of the spectral hole area with time τ can be fit to [32]

$$A(\tau) = e^{-\tau/T_e} + \frac{\beta}{2}\frac{T_a}{T_a - T_e}\left(e^{-\tau/T_a} - e^{-\tau/T_e}\right) \tag{2.22}$$

where, T_e and T_a are the lifetimes of the excited state $|e\rangle$ and auxiliary level (shelving-level) $|a\rangle$, β is the branching ratio, i.e. the fraction of the population that decay into $|a\rangle$ from the excited state $|e\rangle$.

Moreover, it is also possible to measure the width of the spectral hole Γ_{hole}. When, extrapolated to zero time delay $\tau = 0$ and minimum burning power, the measured hole width is a convolution between the linewidth of the laser and the homogeneous linewidth [33]. For increasing laser intensity I, the measured hole width Γ_{hole} will increase as $\Gamma_{hole}(\tau) = \Gamma_{hole}(\tau = 0)(1+\sqrt{1+\Omega^2 T_1 T_2})$ [34], where $\Omega = M\sqrt{I}/\hbar$ is the Rabi frequency, T_1 the excited state lifetime, and T_2 is the optical coherence lifetime. This so-called **power**

broadening arises since, with more laser power, ions that are slightly off-resonant with the laser can be excited and take part in the spectral hole.

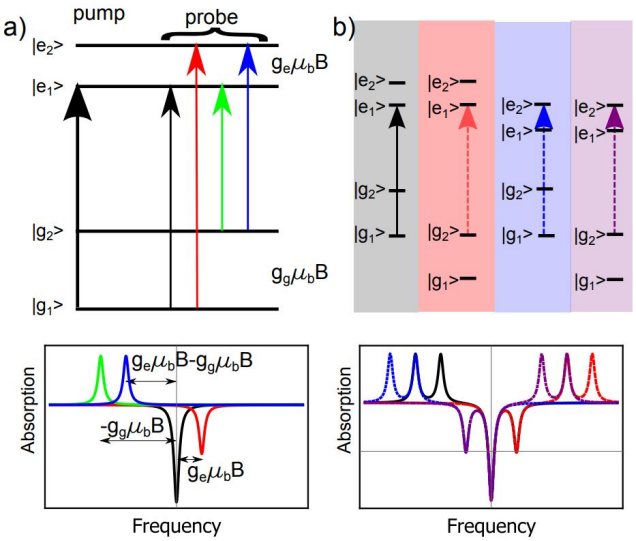

Figure 2.8: **Persistent spectral hole burning:** a) The solid thick arrow shows the frequency of the pump laser that is assumed to be resonant with $|g_1\rangle \rightarrow |e_1\rangle$ transition (denoted as "pump"), and the thin arrows show all other transitions in an ensemble of atoms without inhomogeneous broadening (denoted as "probe"). Two anti-holes are created due to the overpopulated transitions (excess of atomic population in the ground-state sub-level $|g_2\rangle$) and a side-hole is created due to the depleted transition (lack of atomic population in $|g_1\rangle$). b) Due to the inhomogeneous broadening the pump (burning) laser is simultaneously resonant with four transitions, which generates a symmetric hole-burning spectrum with respect to the central hole. Such hole and anti-hole patterns occur only when the inhomogeneous broadening is much larger than the energy splitting between spin sub-levels ($\Gamma_{in} \gg \Delta_g, \Delta_e$). Note that each of the four classes of ions creates one central hole, one side-hole, and two anti-holes similar to a). The sum of all these is indicated in the lower panel of b). The figure is adapted from [30].

To gain more insight into persistent spectral hole burning, let us consider a simple 2×2 energy level structure with two sub-levels in the excited state multiplet and two ground state multiplet. Let us first consider an ensemble of atoms without inhomogeneous broadening. As shown in Figure 2.8a, assume that the burning laser is resonant with the $|g_1\rangle \rightarrow |e_1\rangle$ transition, and the target atoms decay into $|g_2\rangle$ via $|e_1\rangle$. A lack of absorption of the $|g_1\rangle \rightarrow |e_1\rangle$ transition results in the creation of a depleted region in the absorption line, observed as a spectral hole (the **central hole**). Another population-depleted region (or a transparency) can be also seen as a **side-hole** in $|g_1\rangle \rightarrow |e_2\rangle$, which is detuned by Δ_e from the central hole. Also, the overpopulation in the ground-state sub-level $|g_2\rangle$ leads to two regions of increased absorption, which can be seen as **anti-holes**, detuned by Δ_g and Δ_g - Δ_e with respect to the central hole, respectively. See the lower panel of 2.8a for the hole configuration. In addition to the lifetime measurements, persistent spectral hole burning therefore also allows one to measure the energy splitting for both the ground and excited state levels. In an inhomogeneously-broadened media, the burning laser frequency is simultaneously resonant with many more transitions, which

results in a symmetric hole pattern as shown in Figure 2.8b.

2.3.2. TWO-PULSE PHOTON ECHO

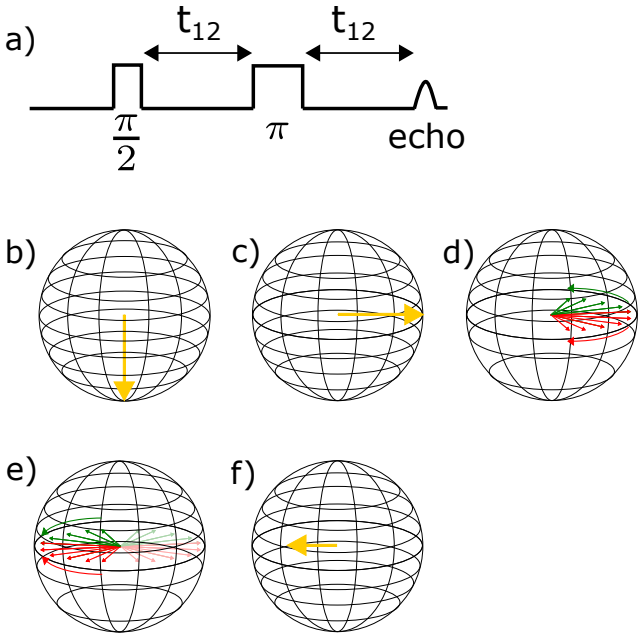

Figure 2.9: A two-pulse photon echo pulse sequence is shown in a). The Bloch sphere representation of the two-pulse photon echo is depicted from b) to f). In b), atoms are in the ground state. In c), the first $\frac{\pi}{2}$ pulse moves atoms to a superposition of the ground and excited state. In d), atoms start dephasing. In e), the π pulse is applied in order to rephase atoms. In f), complete re-phasing results in a coherent emission, a photon echo. (Figure is adapted from [25])

The most commonly used method to quantify atomic coherence in rare-earth-ion-doped crystals is the two-pulse photon echo (2PPE) technique. A photon echo is generated when an ensemble of atoms oscillates coherently, i.e. in-phase, and gives rise to strong coherent radiation. A simple way to generate a photon echo is to use a two-pulse photon echo sequence consisting of two laser pulses interacting with the medium. First, a $\pi/2$ pulse excites a subset of atoms into a superposition of the ground and excited state. Initially, all the atoms will be in phase but each atom has a slightly different resonance frequency so they will dephase. After a certain waiting time t_{12}, a π pulse is applied that reverts the phase angle of the atomic evolution by π. Atoms that have acquired a negative phase difference relative to the laser will now acquire a positive phase and vice versa. Then, after a time $2t_{12}$ from the initial $\pi/2$ pulse, atoms will again start oscillating in phase and cause a coherent emission of the photon echo. Since the coherent phase evolution is perturbed by many processes, such as electric field fluctuations, magnetic field fluctuations, phonons in the environment, and spontaneous decay of population, the intensity of the echo intensity will decay exponentially with increasing time. This

can be fitted using the following equation

$$I_{echo} = I_0 \exp\left\{-2\left(\frac{2t_{12}}{T_2}\right)\right\} \tag{2.23}$$

and the coherence time T_2 can be extracted.

2.3.3. SPECTRAL DIFFUSION AND TWO-PULSE PHOTON ECHO

Spectral diffusion refers to the time-dependent random change in an ion's transition frequency. It is caused by dynamic processes in the ion's environment such as lattice vibrations, two-level systems, or the flipping of neighboring spins, etc. The timescales of those processes can be vastly different. Since all ions in the material are affected by spectral diffusion, the homogeneous linewidth appears to increase over time. For example, the width of a spectral hole seems to broaden with time since the transition frequencies of the ions contributing to the hole are perturbed by spectral diffusion.

Because processes contributing to spectral diffusion occur at different rates, spectral diffusion can perturb the phases of ions in a superposition in a time-dependent way. This effect manifests itself in two-pulse echo decays as a non-exponential shape. In the presence of spectral diffusion, the two-pulse photon echo decays are usually fitted using a generalized version of Equation 2.3.2, also known as Mims decay [35]:

$$I_{\text{echo}} = I_0 \exp\left\{-2\left(\frac{2t_{12}}{T_M}\right)^m\right\} \tag{2.24}$$

Here, T_M is called the effective phase memory time of the system, i.e. the time over which the intensity decays to $1/e^2$ of its initial intensity, and m is called the Mims exponent that describes the non-exponential decay caused by spectral diffusion.

2.3.4. THREE-PULSE PHOTON ECHO

Since spectral diffusion occurs over timescales that are much longer than optical coherence time T_2, it cannot be measured using a 2PPE. We, therefore, need to modify the sequence of pulses. The so-called 3PPE technique is very similar to that discussed above, however, the π pulse is now split into two $\pi/2$ pulses.

In 3PPE, three optical $\pi/2$ pulses are used. The first two pulses that are separated by t_{12} in time create a population grating (a spectrally periodic structure) in the ground and excited state, and the third pulse, after a wait time t_{23}, probes the grating and stimulates a coherent emission, after a time t_{12}. This is because the third pulse transfers the population difference back into a superposition, which then rephases and causes a photon echo to be emitted. The 3PPE pulse sequence and the phase evolution of ions on the Bloch sphere are illustrated in Fig. 2.10. The 3PEE technique provides access to spectral diffusion at long time scales.

In the presence of spectral diffusion, the three-pulse photon echo intensity decay function is given by

$$I(t_{12}, t_{23}) = I_0 \exp\left\{-\frac{2t_{23}}{T_1}\right\} \exp\{-4t_{12}\pi\Gamma_{\text{eff}}(t_{12}, t_{23})\} \tag{2.25}$$

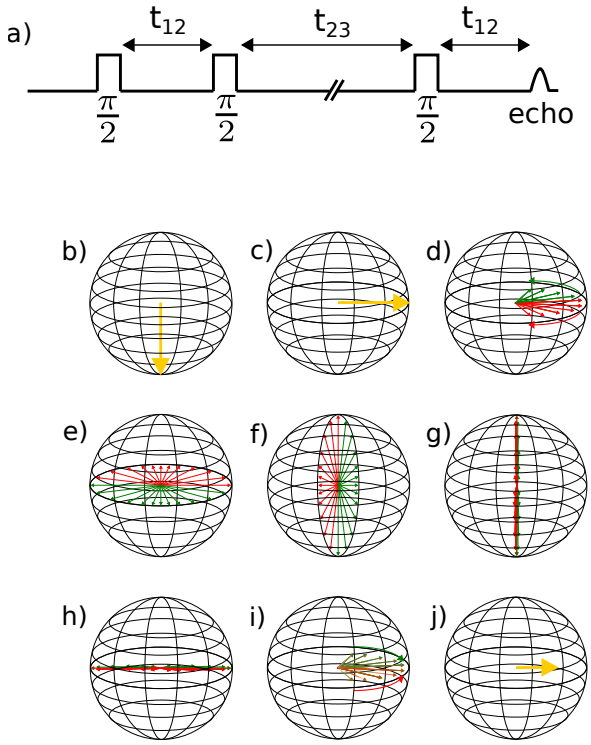

Figure 2.10: A three-pulse photon echo pulse sequence is shown in a). The Bloch sphere representation of the three-pulse photon echo is depicted from b) to j). In b), atoms are in the ground state. In c), the first $\frac{\pi}{2}$ pulse moves atoms to a superposition of ground and excited state. In d), atoms start dephasing. In e), atoms are dephased. In f), the second $\frac{\pi}{2}$ pulse is applied to move the atoms to the ground and excited state depending on their frequency detunings and hence phase. In g), a population grating is created in the ground and excited states. In h), the third $\frac{\pi}{2}$ pulse is applied to stimulate the re-emission. In i), atoms are rephasing. In j), the complete rephasing leads to the emission of a photon echo. (Figure is adapted from [25])

where the first factor exp(-2t_{23}/T_1) describes the population decay during t_{23} and the second factor exp(-4 $t_{12}\pi\Gamma_{\text{eff}}$) describes the effect of decoherence during the t_{12}. Γ_{eff} is the time-dependent "effective" homogeneous linewidth. The functional form of Γ_{eff} is written as [15, 36]

$$\Gamma_{\text{eff}}(t_{12}, t_{23}) = \Gamma_0 + \frac{1}{2}\Gamma_{\text{SD}}\left[Rt_{12} + \left\{1 - \exp\left(-Rt_{23}\right)\right\}\right] \tag{2.26}$$

where Γ_0 is the homogeneous linewidth in the absence of spectral diffusion, Γ_{SD} is the FWHM of the maximum broadening of the optical transition linewidth, and R is the rate of the spectral diffusion. A detailed description of 2PPE and 3PPE, performed in a thulium-doped crystal is discussed in the subsequent chapter.

Because of the inherent properties of the two-pulse photon echo technique, it is suitable for classical light storage. But two- and three-pulse photon echo protocols are not appropriate for quantum memory due to spontaneous emission produced by excited-

level population decay that decreases the fidelity of the quantum information encoded into the emitted photon [37, 38]. The atomic frequency comb quantum memory protocol (employed in this thesis) [39, 40] is a way to achieve the storage and re-emission of individual photons without the addition of noise.

2.3.5. THE ATOMIC FREQUENCY COMB (AFC) QUANTUM MEMORY PROTOCOL

To create a quantum memory for light, numerous protocols such as electromagnetically-induced transparency (EIT), off-resonant Raman, and controlled reversible inhomogeneous broadening (CRIB)-based protocols and various physical media such as single atoms, warm and cold atomic vapors, or solid-state atomic ensembles have been considered, as reviewed in [14, 41] and [25, 30]. The atomic ensemble-based approaches for quantum memory can be categorized into two schemes: optically controlled quantum memory and engineered absorption-based quantum memory. We consider the two-level atomic frequency comb (AFC) quantum memory protocol, which belongs to engineered absorption-based quantum memory. The AFC protocol was first proposed for quantum state storage and experimentally demonstrated by Afzelius et al. [39] in 2008. As the name suggests, an AFC is a periodic comb-like structure in the frequency domain that can be prepared by optically pumping the atomic population to a shelving level in a frequency-selective way, a process known as spectral tailoring. The protocol takes advantage of the inhomogeneously broadened optical transition and inherently allows multiplexed storage. Rare-earth-doped crystals are suitable media for AFC since they have a naturally broadened absorption line. The working principle of an AFC-based quantum memory is inspired by the conventional stimulated/accumulated photon echo technique where the spontaneous emission from the excited state is excluded. This particular protocol is very well suited for our frequency multiplexed quantum repeater architecture since the AFC protocol is intrinsically multimode in nature and its multimode capacity is independent of the overall optical depth of the storage medium. The interaction between an incoming photon and the AFC leads to absorption followed by a re-emission after a pre-defined storage time, which will be described below.

Initially, all atoms are assumed to be in the ground state (lowest crystal field level), which can be fulfilled by cooling down the atomic ensemble. The atoms are then pumped to a long-lived shelving level by means of frequency selective optical pumping to create a comb-like periodic structure in the frequency domain, described in Figure 2.12a. Before a single photon is absorbed, the joint state of the photon-atomic ensemble system can be represented as follows:

$$|1\rangle_{ph} \otimes \left|g_1, g_2, \ldots, g_j, \ldots, g_N\right\rangle_a \tag{2.27}$$

where the first term represents a single photon state and the second term represents the atomic state with all N atoms forming the atomic ensemble. When a single photon is absorbed by the AFC with peaks of width γ that are separated by Δ, a collective excitation is generated amongst all the atoms which can be written as a superposition of all possible

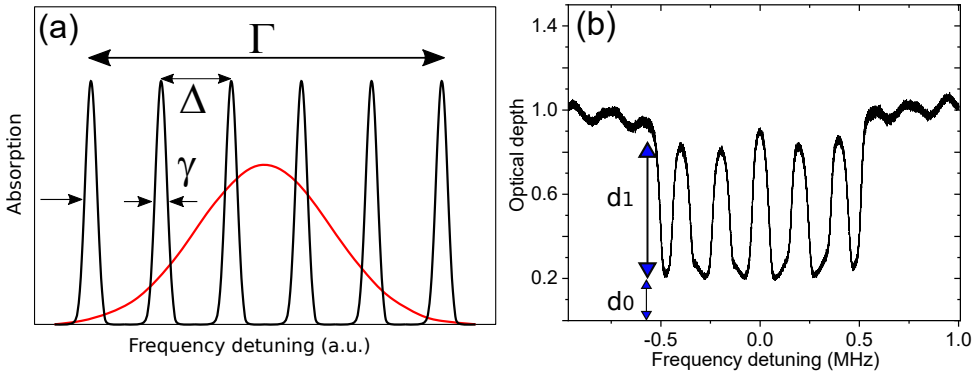

Figure 2.11: (a) The red Gaussian envelope represents the incoming signal photon's spectral width, which is absorbed by the AFC structure of width Γ. γ corresponds to the linewidth of each AFC tooth, and Δ is the peak spacing. The figure is reproduced from [25] (b) AFC of 1 MHz bandwidth tailored for 5 μs storage time. The calculated efficiency is approximately 1%.

states in which one atom is excited. The resulting state can be described by a Dicke state:

$$|0\rangle_{ph} \otimes \left(|\Psi(t)\rangle = \frac{1}{\sqrt{N}} \sum_{j=1}^{N} C_j e^{-i2\pi\delta_j t} e^{ikz_j} \left| g_1, g_2, \ldots, e_j, \ldots, g_N \right\rangle \right)_a \tag{2.28}$$

where $|e_j\rangle$ represents the jth atom being in the excited state, δ_j is the detuning of the atomic transition frequency with respect to the central frequency of the absorbed photon, z_j is the position index of the atomic system measured along the propagation direction of the light, k the wave-vector, C_j the absorption probability amplitude of the jth atom that depends on resonance frequency and position, and t is the elapsed time after the photon is absorbed. We assume that the absorbed photon's bandwidth is greater than the peak spacing Δ but less than the overall width of the frequency comb. Next, the collective excitation rapidly dephases since each atom has a different transition frequency or detuning δ_j. Re-emission of the absorbed photon occurs automatically at a time given by $t = 1/\Delta$ due to re-phasing of the atomic excitation. This is due to the particularly shaped absorption structure, namely the periodicity of the comb which guarantees that $\delta_j = m\Delta$ where m is an integer, and hence for $t = 1/\Delta$, $2\pi\delta_j t = 2\pi m$. This collective re-phasing results in a coherent re-emission, expressed by

$$\begin{aligned} |0\rangle_{ph} \otimes \left(|\Psi(t)\rangle = \frac{1}{\sqrt{N}} \sum_{j=1}^{N} C_j e^{-i2\pi m\Delta t} e^{ikz_j} \left| g_1, g_2, \ldots, e_j, \ldots, g_N \right\rangle \right) \\ \xrightarrow{t=\frac{1}{\Delta}} |1\rangle_{ph} \otimes \left| g_1, g_2, \ldots, g_j, \ldots, g_N \right\rangle_a \end{aligned} \tag{2.29}$$

Thus, the storage time $t = 1/\Delta$ is pre-programmed before absorption and does not allow on-demand retrieval. Since in our approach photons are encoded into different frequency modes, this allows AFCs with fixed storage times to be utilized in frequency multiplexed quantum repeaters. The storage time can further be increased by transferring the optical AFC excitation to a spin-excitation by means of an additional control

pulse and read out on-demand by a second transfer pulse. This is known as the **spin-wave AFC protocol** [40], which is described in Figure 2.12. The storage time in this case is $t = 1/\Delta + (t_2 - t_1)$, where at time t_1 a π pulse maps the optical coherence onto the spin transition and at time t_2, another π pulse the spin-coherence back to the optical transition.

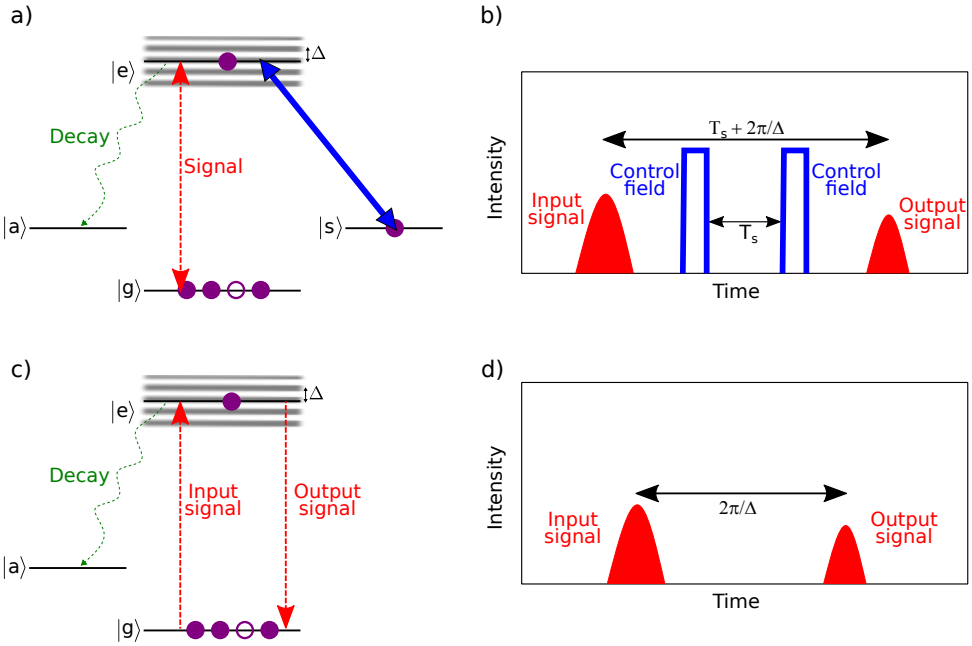

Figure 2.12: a) Energy level structure for the AFC quantum memory protocol. b) Time sequence of storage and retrieval in the spin-wave AFC protocol. c) Energy level structure used for the two-level AFC protocol. d) Time sequence of storage and retrieval process in the AFC protocol. The figure is reproduced from [25].

To obtain longer storage times indicates preparing AFCs with more closely spaced peaks and narrowing the width of each tooth accordingly in order to keep the efficiency the same. However, in practice, there is a limit. AFC storage is fundamentally limited by the optical coherence time, which sets the upper bound for the storage time in a given material and transition. For a given coherence time, the limit in storage time is determined by the closest separation between comb teeth Δ. In the AFC spin-wave protocol, the spin transition is less sensitive to external/environmental perturbations and features longer population and coherence times than the optical transitions. The storage time, in this case, is limited by the spin coherence time of the involved long-lived spin-states.

The forward re-emission efficiency of an AFC with a pre-programmed storage time featuring gaussian-shaped teeth is given by

$$\eta = \left(\frac{d_1}{F}\right)^2 e^{-\frac{d_1}{F}} e^{\frac{-7}{F^2}} e^{-d_0} \tag{2.30}$$

where d_1 is the **optical depth of the comb teeth**, d_0 is the **background or residual optical depth**, and $F = \Delta/\gamma$ is the **comb finesse**, where γ is the **linewidth of each tooth**.

The first term in this expression describes the collective re-emission probability. Higher d_1 means more atoms participate in the collective re-emission process, resulting in higher retrieval probability. On the other hand, increasing the finesse F for a given d_1 reduces this retrieval probability because of larger spacing in the AFC, which effectively decreases the optical depth by creating a larger transmission window. The second term describes the probability of the re-absorption of the re-emitted photon. The third term represents intrinsic dephasing due to the finite linewidth of each AFC tooth. The higher the finesse, the narrower the spectral peaks, and in turn, the more valid the assumption of $\delta_j = m\Delta$. Since the re-emitted photon can be re-absorbed, the maximum achievable retrieval efficiency in the forward direction is limited to 54% [42, 43]. A 100% retrieval efficiency can be achieved if the photon is recalled in the backward direction or the crystal is embedded in an impedance-matched optical cavity [44]. The last term in Eq.2.30 represents irreversible or background absorption due to the non-zero absorption formed by non-participating atoms in the collective re-emission. Since all the terms except the last, are coupled a thorough optimization is required to determine the experimentally accessible AFC parameters that give the best efficiency. Note that, the efficiency bound above does not explicitly account for decoherence. We also need to keep in mind that the minimum AFC tooth width is given by twice the homogeneous linewidth i.e $\gamma = 2\Gamma_h$, in the limit of low optical depth and low optical power. So taking optical coherence time T_2 into account, if we express the efficiency η_{AFC} as a function of the storage time $t = 1/\Delta$ and AFC tooth width γ, there would be a decay of AFC efficiency given by

$$\eta_{\text{AFC}} = \eta_{\text{AFC}}(0)e^{-\frac{\gamma}{\Delta}} = \eta_{\text{AFC}}(0)e^{-\frac{2\Gamma_h}{\Delta}} = \eta_{\text{AFC}}(0)e^{-\frac{4}{T_2\Delta}} \tag{2.31}$$

where we used the definition of the optical coherence time T_2, $\Gamma_h = \frac{2}{T_2}$, and the unit of Δ is defined in Hz, while Γ_h is defined in rad/s. Hence, the time it takes for the AFC efficiency to decrease by $1/e$ is given by $T_M = T_2/4$.

2.4. CHOOSING THULIUM IONS IN GARNET MATERIALS

There can be many host-dopant combinations but depending on the application, different properties of a particular ion host combination become important. For example, erbium dopants have the unique property of a coherent optical telecom wavelength transition at around 1.5 μm. At this wavelength, optical attenuation in standard silica fibers is minimized. Hence, erbium-based lasers, amplifiers, modulators as well as optical memory and a variety of fiber-coupled technologies can be integrated easily with the current fiber-optic communication infrastructure that operates in the telecom band [25]. Similarly, ytterbium dopants are interesting for transduction because of their many ground and excited states hyperfine levels with frequency splittings that can be tuned to match the driving frequency of superconducting qubits [45].

The host crystal is almost as important as the dopant ions. While the transition frequency of a particular dopant ion changes only slightly from host to host, the coherence properties can vary drastically due to different noise environments in different crystals. For example, different symmetries of different crystalline sites play an important role in determining the coherence dynamics of the dopant ion. Examples are the absence of a first-order Stark shift due to a vanishing permanent electric dipole moment in an inver-

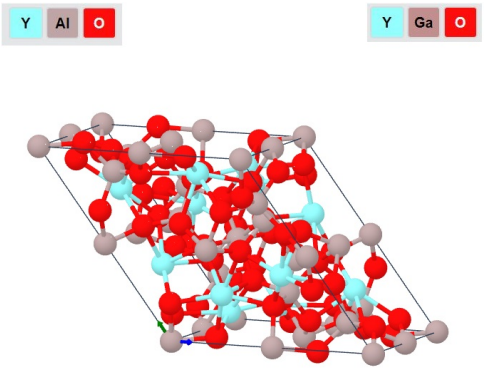

Figure 2.13: Simulated primitive cell of a garnet crystal. Three constituents make up the garnet structure, yttrium pictured in cyan, oxygen pictured in red, and a third species that may include Al, Ga, Fe, etc. shown in brown. The yttrium, or its substitutes, and the additional species bond only to surrounding oxygen in the structure. Image used with permission from the materials projects [49, 50].

sion symmetric crystal can make rare-earth transitions more robust to slowly fluctuating electric fields. Such symmetry exists for instance in yttrium orthovanadate (YVO_4) crystals [45, 46]. Some hosts such as yttrium oxyorthosilicate (YSO) have less abundance of magnetic spins in the crystalline environment, leaving the magnetic dynamics fairly weak when doped with any rare-earth ions [47]. Other crystals like yttrium aluminum garnet (YAG) are interesting because of its thermal properties [48], or lithium niobate $LiNbO_3$ because of its electro-optical and acousto-optical tuning capabilities.

In this thesis, we focus on thulium ions doped into a garnet material - yttrium gallium garnet (YGG) to make long-lived and efficient multimode photonic quantum memories, particularly memories for frequency multiplexed quantum repeaters. The garnet has a cubic crystal structure which is pictured in figure 2.13, where Tm^{3+} substitutes yttrium ions in the lattice without charge compensation. Our selection of Tm^{3+}:YGG can be justified with a few desirable properties of this ion and host combination:

1. Tm^{3+} is a non-Kramers ion, making it less susceptible to magnetic noise.

2. The optical transition of Tm^{3+} ions is close to 795nm wavelength, which can be easily addressed with commercially available diode lasers.

3. Since the host YGG crystal is an isotropic material, there is no preferred axis for light propagation, which allows us to a select subset of Tm ions from potentially useful crystal site orientation.

4. The optical manipulation of populations is quite straightforward in thulium because of its simple three energy levels consisting of an excited state $^3H_4$, a bottleneck level $^3F_4$, and a ground state $^3H_6$.

5. Due to the nuclear spin of 1/2 of ^{169}Tm, it has no additional hyperfine levels, leaving only a pair of degenerate Zeeman sub-levels at zero magnetic field. In the presence of an applied magnetic field, both the ground state and excited state split into

a pair of spin states with a frequency splitting on the order of 10s-100s MHz/T with hundred seconds long lifetimes. This allows efficient optical pumping for creating persistent spectral features in the material.

6. The 1.2ms long optical coherence time T_2 together with a nearly 55 GHz wide absorption profile make Tm^{3+}:YGG a highly desirable candidate for creating a highly-multimode long-lived optical quantum memory.

In the next chapter we will dive into more spectroscopic investigations of Tm:YGG.

BIBLIOGRAPHY

[1] H. Krovi, S. Guha, Z. Dutton, J. A. Slater, C. Simon, and W. Tittel, "Practical quantum repeaters with parametric down-conversion sources", Applied Physics B **122**, 52 (2016).

[2] S. Guha, H. Krovi, C. A. Fuchs, Z. Dutton, J. A. Slater, C. Simon, and W. Tittel, "Rate-loss analysis of an efficient quantum repeater architecture", Phys. Rev. A **92**, 022357 (2015).

[3] N. Sinclair et al., "Spectral multiplexing for scalable quantum photonics using an atomic frequency comb quantum memory and feed-forward control", Phys. Rev. Lett. **113**, 053603 (2014).

[4] E. Saglamyurek et al., "A multiplexed light-matter interface for fibre-based quantum networks", Nature communications **7**, 1–7 (2016).

[5] P.-C. Wang, O. Pietx-Casas, M. F. Askarani, and G. C. Do Amaral, "Proposal and proof-of-principle demonstration of fast-switching broadband frequency shifting for a frequency-multiplexed quantum repeater", JOSA B **38**, 1140–1146 (2021).

[6] S. Massar and S. Popescu, "Optimal extraction of information from finite quantum ensembles", in *Asymptotic theory of quantum statistical inference: selected papers* (World Scientific, 2005), pp. 356–364.

[7] N. Sangouard, C. Simon, H. De Riedmatten, and N. Gisin, "Quantum repeaters based on atomic ensembles and linear optics", Reviews of Modern Physics **83**, 33 (2011).

[8] A. Ortu, J. V. Rakonjac, A. Holzäpfel, A. Seri, S. Grandi, M. Mazzera, H. de Riedmatten, and M. Afzelius, "Multimode capacity of atomic-frequency comb quantum memories", Quantum Science and Technology **7**, 035024 (2022).

[9] B. Jacquier et al., *Spectroscopic properties of rare earths in optical materials*, Vol. 83 (Springer Science & Business Media, 2005).

[10] L. Slooff, A. Van Blaaderen, A. Polman, G. Hebbink, S. Klink, F. Van Veggel, D. Reinhoudt, and J. Hofstraat, "Rare-earth doped polymers for planar optical amplifiers", Journal of applied physics **91**, 3955–3980 (2002).

[11] N. Ohlsson, R. K. Mohan, and S. Kröll, "Quantum computer hardware based on rare-earth-ion-doped inorganic crystals", Optics communications **201**, 71–77 (2002).

[12] T. Zhong and P. Goldner, "Emerging rare-earth doped material platforms for quantum nanophotonics", Nanophotonics **8**, 2003–2015 (2019).

[13] T. W. Mossberg, "Time-domain frequency-selective optical data storage", Optics letters **7**, 77–79 (1982).

[14] W. Tittel, M. Afzelius, T. Chaneliere, R. L. Cone, S. Kröll, S. A. Moiseev, and M. Sellars, "Photon-echo quantum memory in solid state systems", Laser & Photonics Reviews **4**, 244–267 (2010).

[15]T. Böttger, C. W. Thiel, Y. Sun, and R. L. Cone, "Optical decoherence and spectral diffusion at 1.5 μm in $Er^{3+}:Y_2SiO_5$ versus magnetic field, temperature, and Er^{3+} concentration", Phys. Rev. B **73**, 075101 (2006).

[16]R. W. Equall, Y. Sun, R. L. Cone, and R. M. Macfarlane, "Ultraslow optical dephasing in Eu^{3+}:Y_2 SiO_5", Phys. Rev. Lett. **72**, 2179–2182 (1994).

[17]M. Zhong, M. P. Hedges, R. L. Ahlefeldt, J. G. Bartholomew, S. E. Beavan, S. M. Wittig, J. J. Longdell, and M. J. Sellars, "Optically addressable nuclear spins in a solid with a six-hour coherence time", Nature **517**, 177–180 (2015).

[18]M. F. Askarani et al., "Long-lived solid-state optical memory for high-rate quantum repeaters", Phys. Rev. Lett. **127**, 220502 (2021).

[19]A. J. Freeman and R. Watson, "Theoretical investigation of some magnetic and spectroscopic properties of rare-earth ions", Physical Review **127**, 2058 (1962).

[20]M. Le Dantec, "Electron spin dynamics of erbium ions in scheelite crystals, probed with superconducting resonators at millikelvin temperatures", PhD thesis (Université Paris-Saclay, 2022).

[21]T. Böttger, C. W. Thiel, R. L. Cone, and Y. Sun, "Effects of magnetic field orientation on optical decoherence in $Er^{3+}:Y_2SiO_5$", Phys. Rev. B **79**, 115104 (2009).

[22]R. Macfarlane and R. Shelby, "Coherent transient and holeburning spectroscopy of rare earth ions in solids", in *Modern problems in condensed matter sciences*, Vol. 21 (Elsevier, 1987), pp. 51–184.

[23]B. G. Wybourne, "Spectroscopic properties of rare earths", (1965).

[24]G. C. Bjorklund et al., *Persistent spectral hole-burning: science and applications*, Vol. 44 (Springer Science & Business Media, 2012).

[25]M. F. Askarani, "Telecom-wavelength quantum memories in rare earth ion-doped materials for quantum repeaters", (2019).

[26]Y. Sun, C. Thiel, R. Cone, R. Equall, and R. Hutcheson, "Recent progress in developing new rare earth materials for hole burning and coherent transient applications", Journal of luminescence **98**, 281–287 (2002).

[27]C. W. Thiel, T. Böttger, and R. Cone, "Rare-earth-doped materials for applications in quantum information storage and signal processing", Journal of luminescence **131**, 353–361 (2011).

[28]R. Orbach, "Spin-lattice relaxation in rare-earth salts", Proceedings of the Royal Society of London. Series A. Mathematical and Physical Sciences **264**, 458–484 (1961).

[29]A. Abragam and B. Bleaney, *Electron paramagnetic resonance of transition ions* (Oxford University Press, 2012).

[30]T. Lutz, "Engineered impurity-doped materials for quantum information processing applications — nano-structures and disordered materials", PhD thesis (University Of Calgary, 2017).

[31]A. Szabo, "Observation of hole burning and cross relaxation effects in ruby", Physical Review B **11**, 4512 (1975).

[32] C. Thiel, Y. Sun, T. Böttger, W. Babbitt, and R. Cone, "Optical decoherence and persistent spectral hole burning in tm3+: linbo3", Journal of luminescence **130**, 1598–1602 (2010).

[33] M. C. Gupta and J. Ballato, *The handbook of photonics* (CRC press, 2018).

[34] H. de Vries and D. A. Wiersma, "Photophysical and photochemical molecular hole burning theory", The Journal of Chemical Physics **72**, 1851–1863 (1980).

[35] W. Mims, "Phase memory in electron spin echoes, lattice relaxation effects in caw o 4: er, ce, mn", Physical Review **168**, 370 (1968).

[36] C. W. Thiel, N. Sinclair, W. Tittel, and R. L. Cone, "Optical decoherence studies of Tm^{3+} : $Y_3Ga_5O_{12}$", Phys. Rev. B **90**, 214301 (2014).

[37] J. Ruggiero, J.-L. Le Gouët, C. Simon, and T. Chaneliere, "Why the two-pulse photon echo is not a good quantum memory protocol", Physical Review A **79**, 053851 (2009).

[38] N. Sangouard, C. Simon, J. Minář, M. Afzelius, T. Chaneliere, N. Gisin, J.-L. Le Gouët, H. de Riedmatten, and W. Tittel, "Impossibility of faithfully storing single photons with the three-pulse photon echo", Physical Review A **81**, 062333 (2010).

[39] M. Afzelius, C. Simon, H. de Riedmatten, and N. Gisin, "Multimode quantum memory based on atomic frequency combs", Phys. Rev. A **79**, 052329 (2009).

[40] M. Afzelius et al., "Demonstration of atomic frequency comb memory for light with spin-wave storage", Phys. Rev. Lett. **104**, 040503 (2010).

[41] A. I. Lvovsky, B. C. Sanders, and W. Tittel, "Optical quantum memory", Nature photonics **3**, 706–714 (2009).

[42] M. Afzelius, C. Simon, H. de Riedmatten, and N. Gisin, "Multimode quantum memory based on atomic frequency combs", Phys. Rev. A **79**, 052329 (2009).

[43] P. Jobez, N. Timoney, C. Laplane, J. Etesse, A. Ferrier, P. Goldner, N. Gisin, and M. Afzelius, "Towards highly multimode optical quantum memory for quantum repeaters", Phys. Rev. A **93**, 032327 (2016).

[44] M. Afzelius and C. Simon, "Impedance-matched cavity quantum memory", Phys. Rev. A **82**, 022310 (2010).

[45] J. G. Bartholomew, J. Rochman, T. Xie, J. M. Kindem, A. Ruskuc, I. Craiciu, M. Lei, and A. Faraon, "On-chip coherent microwave-to-optical transduction mediated by ytterbium in yvo4", Nature communications **11**, 1–6 (2020).

[46] J. M. Kindem, A. Ruskuc, J. G. Bartholomew, J. Rochman, Y. Q. Huan, and A. Faraon, "Control and single-shot readout of an ion embedded in a nanophotonic cavity", Nature **580**, 201–204 (2020).

[47] E. Fraval et al., "Minimising the decoherence of rare earth ion solid state spin qubits", (2005).

[48] R. Moncorgé, "Current topics in rare-earth lasers", in *Spectroscopic properties of rare earths in optical materials* (Springer, 2005), pp. 320–378.

[49] K. Persson, *Materials data on y3al5o12 (sg:230) by materials project*, An optional note, July 2014.

[50] K. Persson, *Materials data on y3ga5o12 (sg:230) by materials project*, An optional note, July 2014.

3

Optical Coherence and Relaxation Dynamics in a Thulium-doped Yttrium Gallium Garnet Crystal at sub-Kelvin Temperatures for Quantum Memory Applications

Antariksha Das, Mohsen Falamarzi Askarani, Jacob H. Davidson, Neil Sinclair, Joshua A. Slater, Sara Marzban, Charles W. Thiel, Rufus L. Cone, Daniel Oblak, and Wolfgang Tittel

Rare-earth ion-doped crystals with a long optical coherence time are of great interest to serve as multimode, long-lived quantum memories for spectrally multiplexed quantum repeaters. Towards this end, spectroscopic investigations on a yttrium gallium garnet (YGG) crystal, doped with 1% Tm^{3+} and cooled to 500 mK, are presented. In the presence of a magnetic field of a few hundred Gauss, this crystal offers an optical coherence lifetime exceeding one millisecond and a ground-state Zeeman level lifetime as long as tens of seconds. By taking advantage of these two unique spectroscopic properties we implement a persistent atomic frequency comb (AFC) quantum memory protocol to demonstrate multiplexed storage of classical laser pulses in the temporal and spectral domains. Furthermore, we characterize the temporal evolution of spectral holes at different magnetic fields

Parts of this chapter will be submitted to Optical Materials Express.

in the context of long-term spectral diffusion, which is crucial in order to build an efficient long-lived quantum memory. Our results establish a promising photonic quantum memory platform for quantum communication with rare earth ions.

3.1. PREAMBLE

In this chapter, spectroscopic characterization and coherence properties of the $^3H_6 \leftrightarrow {}^3H_4$ transition at 795.325 nm of 1% Tm^{3+}:$Y_3Ga_5O_{12}$ (Tm:YGG) is studied at temperatures as low as 500 mK. The magnetic field dependence of the optical coherence lifetime and spectral diffusion is measured. Photon echo excitation and spectral hole burning methods have been used to fully characterize the material properties. Our result show that optical coherence time exceeding one millisecond and a ground-state Zeeman level lifetime as long as tens of seconds can be obtained in this crystal in the presence of a magnetic field of a few hundred Gauss. Overall, we find that Tm:YGG can be a promising candidate for applications that rely on long coherence times, such as optical quantum memories and photonic signal processing.

3.2. INTRODUCTION

RARE-earth-ion-doped crystals (REIC) [1–4] have been identified as promising candidates for quantum memory applications [5] in a series of recent demonstrations, including storage of quantum states with long storage times [6, 7], high efficiencies [8–11], high multimode capacity [12–14] and entanglement storage [15, 16] etc. The frequency multiplexed quantum repeater architecture proposed by Sinclair et al. [17] offers a simple and novel objective towards satisfying the stringent criteria to achieve a higher rate of entanglement distribution; it demands a frequency multiplexed optical quantum memory with a few hundred microseconds of storage time [18]. Quantum memories have already been realized using various physical systems such as hot and cold atomic vapor [9–11, 19–21], single-trapped atoms, diamond colour centres [22–26], rare earth-ion-doped solids [2–4], to name a few. In particular, the interest in using rare earth-doped solids for quantum memories is due to the long coherence times [7, 18, 27, 28] observed for both optical and spin transitions. Understanding the spectroscopic properties and decoherence dynamics in a cryogenically-cooled environment is of fundamental interest and a prerequisite for applications of these materials for quantum memories.

Thulium-doped crystals [29–31] are desirable candidates for spectrally-multiplexed quantum memories with fixed storage time, an approach to storage that hinges on the two-level atomic frequency comb (AFC) protocol [32, 33]. These crystals possess the simplest energy level structure that allows for spectral tailoring as needed to create AFCs: Both the ground and excited states split under the application of a magnetic field into two long-lived Zeeman levels, which allows persistent spectral hole burning [34]. Furthermore, the optical coherence time, which determines the maximum storage time, is generally long, e.g. 105μs in Tm:YAG [35].

In this work, we investigate the spectroscopic properties of a 1% thulium-doped ytterbium gallium garnet (Tm^{3+}:$Y_3Ga_5O_{12}$) crystal at temperatures as low as 500 mK. We measure the optical coherence time and the lifetime of all energy levels of Tm^{3+} that are relevant for the AFC protocol by means of two-pulse photon echo (2PPE) and time-

resolved spectral hole burning (SHB) techniques. We find a sub-kHz wide homogeneous linewidth - the third narrowest reported for any optical transition after Erbium and Europium [27, 28] as well as Zeeman levels within the electronic ground state with up to 300 sec lifetime. Furthermore, We observe and model the magnetic field-dependent broadening of spectral holes which is explained qualitatively in the context of spectral diffusion. Despite this behavior, the exceptional homogeneous linewidth together with a 55 GHz broad absorption profile [31] and long-lived atomic levels, makes Tm:YGG a promising candidate for multimode quantum memories that enable spectrally multiplexed quantum repeaters.

Our paper is organized as follows: The first two sections, Section 2 and Section 3, are devoted to discussing the properties of the Tm^{3+}:YGG crystal used in our experiment and the description of the experimental setup. In Section 4, the results of the Zeeman-level lifetimes and the measurements of optical coherence are presented. Then, we study spectral diffusion in the presence of magnetic fields for different timescales. Towards this end, the results of three-pulse photon echo experiments and spectral hole burning measurements are presented and plausible underlying decoherence mechanisms are proposed and discussed. in Section 6, we demonstrate microsecond long storage of 10 subsequent laser pulses and simultaneous storage of 3 different spectral modes using the AFC echo scheme. We terminate the paper with a conclusion and outlook.

3.3. TM:YGG MATERIAL PROPERTIES

For our measurements, we use a 25 mm × 5 mm × 5 mm ($a \times b \times c$) single crystal of 1% Tm^{3+}:$Y_3Ga_5O_{12}$ from Scientific Materials Corp (Bozeman, MT). $Y_3Ga_5O_{12}$ (YGG) is a cubic crystal in which all naturally occurring isotopes of the host ions Y and Ga feature nuclear spin: I = $\frac{1}{2}$ for ^{89}Y and I = $\frac{3}{2}$ for ^{69}Ga and ^{71}Ga. Tm^{3+} ions substitute for Y^{3+} without charge compensation in six crystallographically equivalent but orientationally inequivalent sites of D_2 point symmetry. The transition between the lowest Stark levels of the electronic ground state $^3H_6$ and optically excited state $^3H_4$ occurs at a wavelength of 795.325 nm in vacuum. A simplified energy-level diagram of Tm^{3+}:$Y_3Ga_5O_{12}$ is shown in the inset of Fig. 5.2. Tm^{3+} is a non-Kramers ion with 12 electrons in 4f orbitals, the energy levels are electronic singlets and the angular momentum is quenched by the crystal field, resulting in no first-order hyperfine interaction. Due to the I= $\frac{1}{2}$ nuclear spin of Tm^{3+}, quadrupole, and second-order magnetic hyperfine interactions vanish in the absence of a magnetic field. When an external magnetic field is applied, nuclear Zeeman and electronic Zeeman interactions combine with a second-order hyperfine interaction to split the ground and excited states into a pair ($m_I = \pm\frac{1}{2}$) of sublevels. We refer to these levels as Zeeman sublevels but the splitting mechanism includes all interactions mentioned above. The Zeeman sublevel structure is hidden inside the ~ 56 GHz inhomogeneously broadened line of the $^3H_6 \leftrightarrow {}^3H_4$ transition.

3.4. EXPERIMENTAL DETAILS

A schematic of our setup is schematically presented in Fig.3.1. For our measurements the crystal is mounted on the coldest stage of the adiabatic demagnetization refrigeration (ADR)-based cryostat, providing a temperature below 600 mK. The light propagates

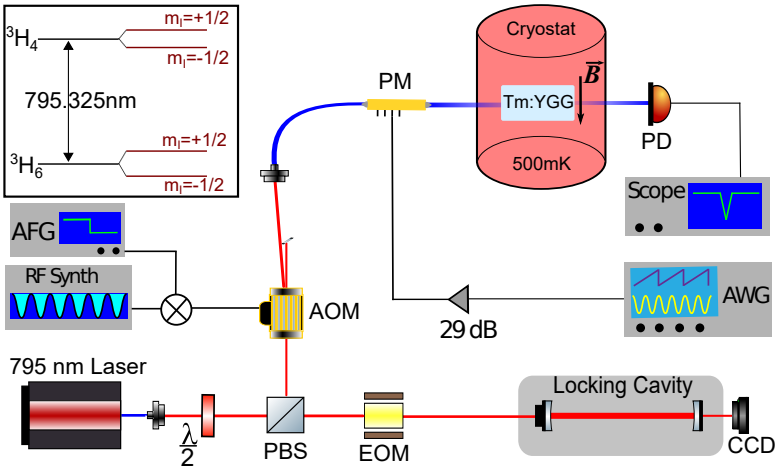

Figure 3.1: **A schematic diagram of the experimental setup:** AFG: arbitrary function generator; RF Synth: radio frequency synthesizer; AOM: acousto-optic modulator; AWG: arbitrary waveform generator; PM: phase modulator; EOM: electro-optic modulator; PD: photo detector; CCD: charge-coupled device camera; ***B***: Magnetic field. Inset: Simplified energy level diagram of the $^3H_6 \rightarrow {}^3H_4$ optical transition of Tm^{3+} in $Y_3Ga_5O_{12}$ crystal. Only the lowest crystal field levels of each electronic manifold are shown.

along the 25 mm-long < 110 > axis of the crystal and its polarization is linear at the crystal input, orthogonal to the < 111 >-direction. The polarization evolves inside the crystal due to birefringence stemming from imperfect crystal growth. A magnetic field is applied parallel to the < 111 >-direction using a superconducting solenoid. The magnetic field strength is detected using a Hall sensor mounted directly above the crystal.

The optical pulse sequence for our measurements is obtained from a continuous-wave external-cavity Toptica DLPro tunable diode laser emitting at 795.32 nm (vacuum) to address the $^3H_6 \rightarrow {}^3H_4$ transition of Tm^{3+} ions in the crystal. A programmable pulseBlaster controls the timing sequence. The light is gated and shaped with a single-pass free-space acoustic-optic modulator (AOM). The 1st order diffracted light beam from the AOM is sent through a series of optical components (waveplates and polarizing beamsplitter) and a phase modulator (PM) where the frequency of the light is shifted through a serrodying signal created by an arbitrary waveform generator (AWG). Optical transmission through the crystal is detected using an amplified silicon photodetector and a digital oscilloscope.

A small fraction of the light from the diode laser is used to frequency lock the laser to a high finesse cavity using the Pound-Drever-Hall method [36]. For good stability, the frequency stabilization setup is kept on a separate optical breadboard and isolated from the main optical setup. After passing through an electro-optic modulator (EOM)—for the creation of frequency sidebands—, the light beam is sent through a series of optical components for proper coupling into the temperature-stabilized high finesse optical cavity which is kept under vacuum. The reflected signal is measured with a photodiode, creating a feedback loop via a PID controller to suppress laser frequency fluctuations. This allows us to obtain a narrow laser linewidth of a few tens of kilohertz.

3.5. SPECTROSCOPIC RESULTS

3.5.1. SPECTRAL HOLE BURNING MEASUREMENTS

In order to determine the lifetime of different energy levels and Zeeman sub-levels of Tm^{3+}:YGG, we employ a widely-used spectroscopic technique known as time-resolved spectral hole burning (SHB). We set up a hole-burning sequence composed of following steps: first, the ions in the crystal are optically pumped from the ground to the excited state with a 50 ms-long monochromatic laser pulse. After a waiting time that varies between a few tens of microseconds to a few hundreds of milliseconds, the hole is read out with an attenuated 8 ms long pulse, frequency chirped over 2 MHz. By measuring the area of the spectral hole with varying waiting times, the lifetimes of the various levels that lie between the excited state and the ground state can be extracted. An example of a decay curve is shown in Fig.3.2a. Fitting this spectral hole decay using a double-exponential decay reveals the $^3H_4$ excited state lifetime $T_1 \approx 2$ ms and the $^3F_4$ bottleneck level lifetime $T_b \approx 55$ ms, which is in accordance with previous results [30].

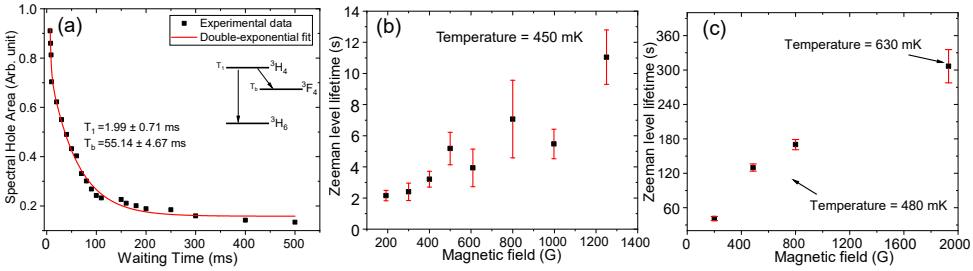

Figure 3.2: **Lifetime measurements:** (a) An example of a transient spectral hole decay which is used to extract the $^3H_4$ excited state level lifetime and $^3F_4$ bottleneck level lifetime. (b) and (c) show the short decay component and long decay component of the Zeeman-level lifetime, respectively.

Next, to measure the ground state $^3H_6$ Zeeman sublevel lifetime, a magnetic field is applied along the < 111 > axis of the crystal with the sample at a temperature of T = 500 mK. Again, by measuring the persistent spectral hole decay as a function of waiting time in presence of a magnetic field, varying from a few hundreds of Gauss to a few thousand of Gauss, we obtain the ground state Zeeman level lifetime as a function of different magnetic field strength, which is shown in Fig.3.2. Due to the D_2 point symmetry of the Tm^{3+} site in YGG lattice, there are six subgroups of magnetically inequivalent Tm^{3+} ions that have different local site orientations. By choosing the propagation direction and optical polarization, different subgroups of ions can be selectively addressed. For our experiment the optical polarization is linear and perpendicular to the < 110 > propagation direction. In presence of the magnetic field only half of the Tm^{3+} ions among six subgroups of magnetically inequivalent Tm^{3+} ions interact with the optical field. Thus, we observe two different sets of Zeeman level lifetimes associated with two different decays due to two magnetically inequivalent subgroups of Tm^{3+} ions [30] as indicated in Fig.3.2b. and Fig.3.2c. respectively. The persistence of Zeeman sublevels allow us to create long-lived spectral holes, which, in turn, allow us to tailor the absorption profile of the crystal to prepare persistent atomic frequency combs (AFC) [32], one of the popular and well-known quantum memory protocol used to store single photons.

3.5.2. OPTICAL COHERENCE TIME MEASUREMENTS

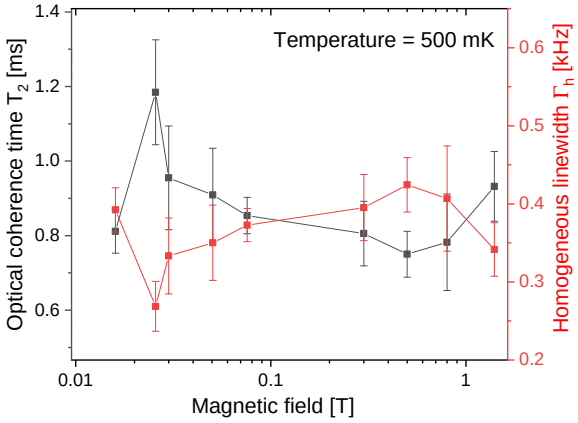

Figure 3.3: **Optical coherence time measurements:** Optical coherence time T_2 as a function of magnetic field strength.

To study the optical coherence properties in Tm^{3+}:YGG, we employ two-pulse photon echo (2PPE) spectroscopy. In a 2PPE sequence, two excitation pulses, separated by a waiting time t_{12} are sent into an inhomogeneously broadened ensemble of resonant Tm^{3+} ions. They prepare a coherent superposition of the ground and excited electronic states. This gives rise to a coherent burst of radiation, or photon echo, at time t_{12} after the second pulse. The variation of the echo intensity as a function of t_{12} can be written as:

$$I(t_{12}) = I_0 e^{-4\pi\Gamma_h t_{12}} \tag{3.1}$$

where I_0 is the initial echo intensity at t_{12}=0 and Γ_h is the homogeneous linewidth, which is inversely proportional to the coherence time T_2 :

$$\Gamma_h = \frac{1}{\pi T_2} \tag{3.2}$$

In order to extract the effective homogeneous linewidth as a function of the magnetic field, we vary the magnetic field from 100 G to 1 kG and measure two-pulse photon echo decays at a temperature of 500 mK and a wavelength of 795.32 nm. We fit all measured photon echo decays using the exponential decay function described in Eq.3.1.

The magnetic field dependence of the coherence time T_2 and of the homogeneous linewidth Γ_h is presented in Fig.3.3. It captures the dominant magnetic field-dependent decoherence processes [29] that limit the performance of the crystal as a quantum memory. We find that the introduction of a few hundred Gauss magnetic fields improves the coherence time T_2 from a zero-field value of 550 μs to a maximum of around 1.1 ms corresponding to a minimum homogeneous linewidth Γ_h of around 0.26 kHz at around 200 G [18]. After that, the measured coherence time T_2 decreases and remains almost steady up to 1 Tesla.

3.6. SPECTRAL DIFFUSION

Spectral diffusion results in a broadening of the homogeneous linewidth Γ_h as a function of time because each Tm^{3+} ion experiences a slightly-different dynamic crystalline environment. Spectral diffusion is expected due to the presence of gallium and yttrium, both of which feature nuclear spins, in the $Y_3Ga_5O_{12}$ lattice. These spins may couple to the Tm3+ ions. The application of a magnetic field generally allows alleviating the impact of spectral diffusion by inducing spin polarization, thus reducing the number of spin flips, and also by increasing the Zeeman-level energy-splitting beyond the phonon energy [1, 37]. Two well-known physical mechanisms that can be accountable for such reduction are spin flips either driven by phonons (spin-lattice relaxation) [38, 39] or spin-spin relaxation through magnetic dipole-dipole interaction [37] that cause pairs of anti-parallel spins to flip simultaneously (spin flip-flops). These correlated spin flips can randomize local spin orientations. The fluctuating magnetic fields within the host YGG crystal can be due to the dynamic interactions between host nuclear spins or paramagnetic impurities. This also suggests more complicated ion-ion coupling or spin-spin interactions [37, 40] that go beyond the work presented here.

3.6.1. THREE-PULSE PHOTON ECHO (3PPE) MEASUREMENTS

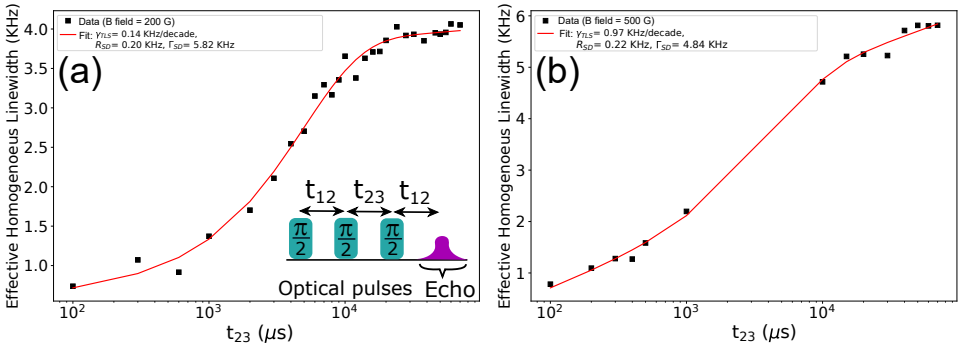

Figure 3.4: **3PPE measurements:** Effective homogeneous linewidth (or the inverse of effective coherence time) as a function of time delay t_{23} at 500 mK temperature for an applied magnetic field (a) 200 G and (b) 500 G. The solid line represents the fit of the data. In the inset, the three-pulse photon echo sequence is shown for delay t_{12} between the 1st and the 2nd pulse and t_{23} between the 2nd and the 3rd pulse.

The effective homogeneous linewidth and the time evolution of spectral diffusion-induced decoherence mechanisms can be extracted from three-pulse photon echo measurements. In a 3PPE sequence, the first two excitation pulses, separated by a waiting time t_{12} are sent into an inhomogeneously broadened ensemble of absorbers to create a frequency-dependent periodic modulation of the population in the ground and excited state levels. Then after a time delay t_{23}, a third pulse is applied that causes the atoms to rephase, which gives rise to the emission of an echo at time t_{23} after the third pulse. To investigate spectral diffusion of Tm^{3+} ions at timescales up to 100 ms, we performed 3PPE measurements at a temperature T = 500 mK and a magnetic field of a few hundreds of Gauss. For our measurements, the separation time t_{12} between the first two pulses is

held constant at 60 μs, and the echo intensity is measured as a function of time delay t_{23} between the second and third pulse, with t_{23} varying between 100 μs and 100 ms. To analyze the 3PPE echo decays, we use the generalized formula proposed by Bottger et al. [37]:

$$I(t_{12}, t_{23}) = I_0 e^{-2t_{23}/T_1} e^{-4\pi t_{12}\Gamma_{\text{eff}}(t_{23})} \tag{3.3}$$

where T_1 is the excited state lifetime and $\Gamma_{\text{eff}}(t_{23})$ is the time-dependent "effective" homogeneous linewidth. It captures the information about all diffusion processes that are influencing the rare-earth spins caused by magnetic dipole–dipole interactions. The functional form of $\Gamma_{\text{eff}}(t_{23})$ is given by

$$\Gamma_{\text{eff}}(t_{23}) = \Gamma_0 + \gamma_{TLS} \log(\frac{t_{23}}{t_0}) + \frac{1}{2}\Gamma_{SD}(1 - e^{-R_{SD}t_{23}}) \tag{3.4}$$

Where Γ_0 is the homogeneous linewidth at the minimum measurement timescale t_0 which is 160 μs for our experiment. Γ_{SD} is the maximum broadening of the homogeneous linewidth (or spectral diffusion linewidth) and R_{SD} describes the characteristic diffusion rate of linewidth broadening. The values of these parameters are determined by the details of the diffusion mechanisms [31]. Here we also consider spectral diffusion due to the thermally activated low-energy dynamic structural fluctuations, often described as two-level systems (TLS) [41, 42]. In Eq.3.4 γ_{TLS} is the TLS mode coupling coefficient.

To characterize the effects of spectral diffusion, we fit the echo decays using Eq.3.3 and extract the effective homogeneous linewidth. The measured variation of effective homogeneous linewidth is plotted as a function of the time-delay t_{23} at T = 500 mK, in presence of 200 G and 500 G magnetic field, which are shown in Fig.3.4. Fitting each curve to Eq. 3.4 as shown by the solid line indicates a homogeneous linewidth Γ_0 of a few hundred Hz and the spectral diffusion broadening saturates to a maximum value of a few kHz. Based on the magnitude of the spectral diffusion parameters, Γ_{SD} and R_{SD} (inset of Fig. 3.4), it is very likely that the dominant source of spectral diffusion stems from nuclear spin flips of neighboring gallium in the host lattice. We also find that the contribution of low-energy TLS modes on linewidth broadening is not very pronounced at this temperature. We find little magnetic field dependence of spectral diffusion parameters in this temporal regime.

More precisely, we burn spectral holes at higher magnetic fields of 1 kG - 6 kG and let them evolve over time. The long-lived Zemman-level lifetimes at these fields allow us to probe the spectral hole for hundreds of seconds.

3.6.2. LONG-TERM SPECTRAL DIFFUSION: MAGNETIC FIELD-DEPENDENT SPECTRAL HOLE BROADENING

In the presence of a magnetic field, spectral diffusion is known to occur over timescales on the order of Zeeman-level lifetimes, which, in our crystal, are many seconds. this is much longer than the maximum three-pulse photon echo measurement timescales. Since many optical signal processing applications rely on spectral features being created and probed over long timescales [1, 3], we investigate spectral diffusion on such timescales.

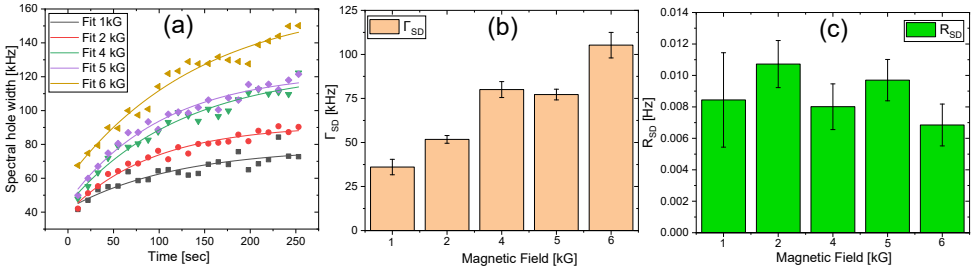

Figure 3.5: **Spectral diffusion:** (a) Spectral hole widths as a function of time at 500 mK temperature where the applied magnetic field is changed gradually from 1 kG - 6 kG. The solid line represents the fitted spectral hole width at different magnetic fields. (b) The variation of the extracted spectral diffusion linewidth Γ_{SD} as a function of the magnetic field strength. (c) The variation of the extracted relaxation rate of linewidth broadening R_{SD} as a function of the magnetic field strength.

To probe spectral diffusion on timescales longer than the characteristic timescales of two-pulse and three-pulse photon echo measurements, we apply a kilo-gauss magnetic field and perform spectral hole burning at a temperature of 600 mK. The burning duration and the waiting time are adjusted to guarantee that the atomic population decays into the desired Zeeman level. Once the hole burning is completed, the spectral hole is read out by a weak probe pulse. Then, we determine the hole widths for a series of different magnetic field strengths from 1 kG to 6 kG. We observe that the spectral hole broadens as a function of time as shown in Fig.3.5a. Since the spectral hole width is proportional to the homogeneous linewidth (assuming no power broadening, $\Gamma_{spectral\text{-}hole} = 2\,\Gamma_{homo}$), the observed behavior can be described by [37]

$$\Gamma_{spectral\text{-}hole}(t) \propto \Gamma_o + \frac{1}{2}\Gamma_{SD}(1 - e^{-R_{SD}t}) \tag{3.5}$$

We find that the spectral diffusion linewidth Γ_{SD} increases gradually from 36 kHz to 105 kHz as the applied magnetic field strength is increased from 1 kG to 6 kG, as shown in Fig.3.5b. We furthermore note that the broadening occurs at an approximately constant rate of 0.01 Hz for different magnetic fields, as indicated in Fig.3.5c. At these time scales, magnetic fields, and temperature, the relaxation rate R_{SD} is much slower than the 3PPE relaxation rate as expected.

The functional dependence of Γ_{SD} on the applied magnetic field can be written as [37],

$$\Gamma_{SD}(B,T) = \Gamma_{max}\,\mathrm{sech}^2(g\mu_b B/2k_B T) \tag{3.6}$$

Here, g indicates the g-factor of spins present in the crystal lattice environment, μ_B is the Bohr magneton, B is the external magnetic field, k_B is the Boltzmann constant, T indicates the temperature, and Γ_{max} is the FWHM of the maximum frequency broadening of the optical transition resulting from the magnetic dipole-dipole interactions.

In Tm^{3+}:YGG, the g-factors of thulium, gallium, and yttrium spins are quite small and the ratio of the thermal distribution of atomic population in Zeeman sublevels re-

mains nearly constant for the temperatures and the magnetic fields used in this work. So the hyperbolic secant term on the R.H.S of the Eq.3.6 is effectively constant. Hence, the spectral diffusion will depend on the magnitude of the created magnetic dipole moment of the Tm^{3+} ions induced by the external magnetic field which is proportional to $\Gamma_{max}(B)$. Below, we list the possible underlying physical processes that lead to variations of the magnetic field at the Tm^{3+} ion locations:

- Ion-ion coupling: Spectral diffusion due to ion-ion interaction can play a role in the observed linewidth, broadening. The low Tm^{3+} ion concentration of 1% in this YGG crystal signifies that the average distance between thulium ions (Tm^{3+}-Tm^{3+} interactions) is unlikely to cause broadening of the observed magnitude but a long-range quadrupole-quadrupole interaction between Tm^{3+} ions may cause this to happen [43–45].

- Phonon-induced spin-flips: As the magnetic field increases, the phonon density of states increases quadratically, leading to an increase in the probability of interaction between phononic modes of the crystalline lattice and the thulium ions [38].

- Spin flip-flops: The observed broadening can also originate from the interaction between thulium ions and neighboring host ions. The neighboring nuclear spins surrounding the Tm^{3+} ion are yttrium Y^{3+} and two isotopes of gallium, ^{69}Ga and ^{71}Ga. Since Y^{3+} nuclear spins are weakly magnetic, one plausible explanation is the presence of a fully concentrated spin bath of gallium nuclear spins, each with a moderate nuclear magnetic moment which can cause the magnetic field variation experienced by the thulium ions.

  An additional contribution is likely a noisy current supply for the superconducting solenoid magnet which may cause magnetic field variations of Γ_{SD}.

3.7. MULTIPLEXED OPTICAL STORAGE

The two-level atomic frequency comb (AFC) is a very well-known established protocol [32] for storage of quantum light in REI doped solids [7, 17, 18]. It relies on shaping of the inhomogeneously broadened absorption profile of an ensemble of absorbers into a series of equally-spaced teeth by means of spectral hole burning (with peak separation Δ). The absorption of a photon by such a comb yields a collective atomic excitation that can be described by a so-called Dicke state:

$$\left(|\Psi\rangle = \frac{1}{\sqrt{N}} \sum_{j=1}^{N} C_j e^{-i2\pi\delta_j t} e^{ikz_j} \left|g_1, g_2, \ldots, e_j, \ldots, g_N\right\rangle\right) \tag{3.7}$$

where $|e_j\rangle$ represents the jth atom being in the excited state, δ_j is the detuning of the atomic transition frequency with respect to the central frequency of the absorbed photon, z_j is the position of the atomic system measured along the propagation direction of the light, k the wavevector, and C_j the absorption probability amplitude of the jth atom. Next, the collective excitation described by the Dicke state will dephase but due to the periodicity of the comb, rephasing of the atomic excitations will occur at time $1/\Delta$,

leading to a photon-echo-like re-emission. The finesse of an AFC is defined as the ratio between the peak separation and the FWHM of the absorption peaks, $F = \frac{\Delta}{\gamma}$.

The multimode capacity of the AFC memory protocol is not dependent on the optical depth of the storage medium, making this protocol a natural choice for multiplexed quantum memories [12, 17]. it provides a large temporal multimode capacity, which can readily be combined with multiplexing in frequency and space. In the time domain, the number of temporal modes that can be stored using the AFC scheme is proportional to the number of comb teeth, which depends on the total bandwidth and the periodicity Δ. In the frequency domain, the number of spectral modes depends on the bandwidth per spectral channel and the total absorption bandwidth of the quantum memory crystal. In the following subsection, we demonstrate a multimode AFC memory both in the temporal and spectral domains. While we perform the experiments using classical optical pulses, it is known that the AFC protocol also allows storing quantum states of light such as qubits with high fidelity [46].

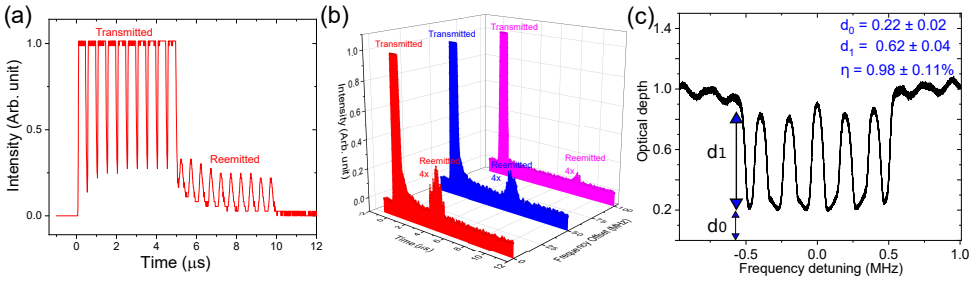

Figure 3.6: **AFC multiplexed storage of optical pulses:** (a) AFC storage of 10 subsequent temporal modes of 200 ns duration during 5 μs. The re-emitted train of pulses can be observed from 5 μs to 10 μs. (b) Frequency-multiplexed AFC quantum memory is used to simultaneously store optical pulses of 1 μs duration in 3 spectral modes, detuned by 50 MHz (in different colors) for 4 μs, 6 μs, and 8 μs storage time respectively. (c) 1 MHz AFC of finesse 2 tailored for 5 μs storage time.

3.7.1. SIMULTANEOUS STORAGE OF SUBSEQUENT TEMPORAL MODES

To demonstrate a multimode AFC storage in time, we prepare a 10 MHz broad AFC with finesse F = 2 by optically pumping Tm^{3+} ions to long-lived Zeeman levels. To avoid the spontaneous emission noise due to population decay from the $^3H_4$ excited-state level, we wait 10 ms (five times longer than the 2 ms lifetime of this level). Then, we create a sequence of 10 subsequent pulses of 200 ns duration and send into the memory. A train of AFC echoes appear after $1/\Delta = 5$ μs storage time. The AFC efficiency is defined as the ratio between the intensity of the AFC echo and the input pulse. The retrieved AFC echoes have an efficiency of around 1% [18]. This value agrees with the theoretical storage efficiency estimated from the Gaussian AFC structure using the formula $\eta = e^{-\tilde{d}}\tilde{d}^2 e^{-7/F^2} e^{-d_0}$ [47]. Here, $\tilde{d} = d/F$, d is the peak absorption depth, d_0 is the background absorption depth, and F is the finesse of the AFC. The reduced efficiency in our experiment is due to the imperfect optical pumping caused by some technical issues such as finite laser linewidth and vibration of the cryostat, which can be especially significant for AFCs with μs long storage times. Note that, the memory efficiency can be

cavity enhanced by exploiting impedance-matching conditions [48].

3.7.2. SIMULTANEOUS STORAGE OF DIFFERENT SPECTRAL MODES

In order to create spectrally-multiplexed AFCs, we utilize two phase modulators (PMs) in series, where one of the PMs generates sidebands spaced by the desired frequency interval between neighboring AFCs while the other PM creates AFCs around each of these frequency bands. Both operations are performed using a technique called serrodyne optical phase modulation [49]. In this way, we program and create simultaneously three 1MHz-wide AFCs with 4, 6, and 8 μs of storage time that are centered at 0, 50, and 100 MHz frequency detuning within the inhomogeneous absorption linewidth of the thulium ions. Each AFC receives an optical pulse whose central frequency is matched with that of the AFC and re-emits the respective echo at the pre-programmed storage time. The spectral read-out of the individual AFC re-emissions is implemented by using a filter cavity at the output of the crystal and by varying the resonant frequency of the cavity to spectrally match each of the frequency modes. This is depicted in Fig.3.6(b).

3.8. DISCUSSION AND CONCLUSION

Our results confirm that Tm:YGG is an interesting material candidate for AFC-based long-lived and multimode quantum memories. In this work, we have demonstrated a multimode optical memory both in the temporal and spectral domains with microseconds long storage times [18], which is a requirement for the construction of multiplexed quantum memories suitable for scalable photonic quantum repeater architectures [17]. We also investigated and discussed plausible reasons for spectral diffusion on short and long timescales. However, more detailed spectroscopic measurements are required to understand the material's full potential, such as if the coherence properties can be further improved by using different magnetic field orientations [44], growing non-birefringent YGG crystals with less impurities and optimizing the material composition for specific quantum memory implementations. For example, it is possible to increase the inhomogeneous broadening by co-doping selected impurities or introducing static crystal strain in order to increase the spectral multiplexing capacity of the memory further. In parallel, optical pumping strategies must be optimized. Furthermore, technical developments such as sub-kHz laser linewidth stabilization; cryostat-vibration isolation of the crystal, and embedding the Tm:YGG crystal in an impedance-matched cavity to enhance the storage efficiency are needed for the creation of desired optical quantum memories that enable long-distance quantum communication.

FUNDING*

We acknowledge funding through the Netherlands Organization for Scientific Research (NWO), the European Unions Horizon 2020 Research and Innovation Program under Grant Agreement No. 820445 and Project Name Quantum Internet Alliance (QIA).

ACKNOWLEDGMENTS*

The authors thank G. C. Amaral, N. Alfasi and T. Chakraborty for experimental help.

BIBLIOGRAPHY

[1] G. Liu and B. Jacquier, *Spectroscopic properties of rare earths in optical materials*, Vol. 83 (Springer Science & Business Media, 2006).

[2] W. Tittel, M. Afzelius, T. Chaneliére, R. Cone, S. Kröll, S. Moiseev, and M. Sellars, "Photon-echo quantum memory in solid state systems", Laser & Photonics Reviews **4**, 244–267 (2010).

[3] C. Thiel, T. Böttger, and R. Cone, "Rare-earth-doped materials for applications in quantum information storage and signal processing", Journal of luminescence **131**, 353–361 (2011).

[4] T. Zhong and P. Goldner, "Emerging rare-earth doped material platforms for quantum nanophotonics", Nanophotonics **8**, 2003–2015 (2019).

[5] A. I. Lvovsky, B. C. Sanders, and W. Tittel, "Optical quantum memory", Nature Photonics **3**, 706–714 (2009).

[6] A. Ortu, A. Holzäpfel, J. Etesse, and M. Afzelius, "Storage of photonic time-bin qubits for up to 20 ms in a rare-earth doped crystal", npj Quantum Information **8**, 1–7 (2022).

[7] Y. Ma, Y.-Z. Ma, Z.-Q. Zhou, C.-F. Li, and G.-C. Guo, "One-hour coherent optical storage in an atomic frequency comb memory", Nature communications **12**, 1–6 (2021).

[8] P. Vernaz-Gris, K. Huang, M. Cao, A. S. Sheremet, and J. Laurat, "Highly-efficient quantum memory for polarization qubits in a spatially-multiplexed cold atomic ensemble", Nature communications **9**, 1–6 (2018).

[9] Y.-W. Cho et al., "Highly efficient optical quantum memory with long coherence time in cold atoms", Optica **3**, 100–107 (2016).

[10] M. Hosseini, B. M. Sparkes, G. Campbell, P. K. Lam, and B. C. Buchler, "High efficiency coherent optical memory with warm rubidium vapour", Nature communications **2**, 1–5 (2011).

[11] X.-H. Bao et al., "Efficient and long-lived quantum memory with cold atoms inside a ring cavity", Nature Physics **8**, 517–521 (2012).

[12] E. Saglamyurek et al., "A multiplexed light-matter interface for fibre-based quantum networks", Nature communications **7**, 1–7 (2016).

[13] T.-S. Yang et al., "Multiplexed storage and real-time manipulation based on a multiple degree-of-freedom quantum memory", Nature communications **9**, 1–8 (2018).

[14] Y. Pu, N. Jiang, W. Chang, H. Yang, C. Li, and L. Duan, "Experimental realization of a multiplexed quantum memory with 225 individually accessible memory cells", Nature communications **8**, 1–6 (2017).

[15]M. F. Askarani, M. G. Puigibert, T. Lutz, V. B. Verma, M. D. Shaw, S. W. Nam, N. Sinclair, D. Oblak, and W. Tittel, "Storage and reemission of heralded telecommunication-wavelength photons using a crystal waveguide", Phys. Rev. Applied **11**, 054056 (2019).

[16]J. V. Rakonjac, D. Lago-Rivera, A. Seri, M. Mazzera, S. Grandi, and H. de Riedmatten, "Entanglement between a telecom photon and an on-demand multimode solid-state quantum memory", Physical review letters **127**, 210502 (2021).

[17]N. Sinclair et al., "Spectral multiplexing for scalable quantum photonics using an atomic frequency comb quantum memory and feed-forward control", Phys. Rev. Lett. **113**, 053603 (2014).

[18]M. F. Askarani et al., "Long-lived solid-state optical memory for high-rate quantum repeaters", Phys. Rev. Lett. **127**, 220502 (2021).

[19]M. Bashkansky, F. K. Fatemi, and I. Vurgaftman, "Quantum memory in warm rubidium vapor with buffer gas", Optics Letters **37**, 142–144 (2012).

[20]J. Guo, X. Feng, P. Yang, Z. Yu, L. Chen, C.-H. Yuan, and W. Zhang, "High-performance raman quantum memory with optimal control in room temperature atoms", Nature communications **10**, 1–6 (2019).

[21]L. Heller, P. Farrera, G. Heinze, and H. de Riedmatten, "Cold-atom temporally multiplexed quantum memory with cavity-enhanced noise suppression", Phys. Rev. Lett. **124**, 210504 (2020).

[22]G. Fuchs, G. Burkard, P. Klimov, and D. Awschalom, "A quantum memory intrinsic to single nitrogen–vacancy centres in diamond", Nature Physics **7**, 789–793 (2011).

[23]Y.-Y. Lai, G.-D. Lin, J. Twamley, and H.-S. Goan, "Single-nitrogen-vacancy-center quantum memory for a superconducting flux qubit mediated by a ferromagnet", Phys. Rev. A **97**, 052303 (2018).

[24]A. Tsukanov, "Quantum memory based on ensemble states of nv centers in diamond", Russian Microelectronics **42**, 127–147 (2013).

[25]K. Nemoto, S. J. Devitt, M. Trupke, A. M. Stephens, M. S. Everitt, K. Buczak, T. Noebauer, J. Schmiedmayer, and W. Munro, "Memory-based quantum repeaters with nv centers", in Cleo: qels_fundamental science (Optical Society of America, 2014), FTu1A–2.

[26]C. E. Bradley, J. Randall, M. H. Abobeih, R. C. Berrevoets, M. J. Degen, M. A. Bakker, M. Markham, D. J. Twitchen, and T. H. Taminiau, "A ten-qubit solid-state spin register with quantum memory up to one minute", Phys. Rev. X **9**, 031045 (2019).

[27]T. Böttger, C. W. Thiel, Y. Sun, and R. L. Cone, "Optical decoherence and spectral diffusion at 1.5 μm in $Er^{3+}:Y_2SiO_5$ versus magnetic field, temperature, and Er^{3+} concentration", Phys. Rev. B **73**, 075101 (2006).

[28]R. W. Equall, Y. Sun, R. L. Cone, and R. M. Macfarlane, "Ultraslow optical dephasing in Eu^{3+}:Y_2 SiO_5", Phys. Rev. Lett. **72**, 2179–2182 (1994).

[29]Y. Sun, C. Thiel, and R. Cone, "Optical decoherence and energy level structure of 0.1% Tm^{+3}: $LiNbO_3$", Physical Review B **85**, 165106 (2012).

[30]C. W. Thiel, N. Sinclair, W. Tittel, and R. L. Cone, "$Tm^{3+}:Y_3Ga_5O_{12}$ Materials for spectrally multiplexed quantum memories", Phys. Rev. Lett. **113**, 160501 (2014).

[31] C. W. Thiel, N. Sinclair, W. Tittel, and R. L. Cone, "Optical decoherence studies of Tm^{3+} : $Y_3Ga_5O_{12}$", Phys. Rev. B **90**, 214301 (2014).

[32] M. Afzelius, C. Simon, H. de Riedmatten, and N. Gisin, "Multimode quantum memory based on atomic frequency combs", Phys. Rev. A **79**, 052329 (2009).

[33] F. Bussières, N. Sangouard, M. Afzelius, H. de Riedmatten, C. Simon, and W. Tittel, "Prospective applications of optical quantum memories", Journal of Modern Optics **60**, 1519–1537 (2013).

[34] M. F. Askarani, T. Lutz, M. G. Puigibert, N. Sinclair, D. Oblak, and W. Tittel, "Persistent atomic frequency comb based on zeeman sub-levels of an erbium-doped crystal waveguide", J. Opt. Soc. Am. B **37**, 352–358 (2020).

[35] R. M. Macfarlane, "Photon-echo measurements on the trivalent thulium ion", Optics letters **18**, 1958–1960 (1993).

[36] E. D. Black, "An introduction to pound–drever–hall laser frequency stabilization", American journal of physics **69**, 79–87 (2001).

[37] T. Böttger, C. W. Thiel, Y. Sun, and R. L. Cone, "Optical decoherence and spectral diffusion at 1.5 μm in Er^{3+} : Y_2SiO_5 versus magnetic field, temperature, and Er^{3+} concentration", Phys. Rev. B **73**, 075101 (2006).

[38] T. Lutz, L. Veissier, C. W. Thiel, R. L. Cone, P. E. Barclay, and W. Tittel, "Modification of phonon processes in nanostructured rare-earth-ion-doped crystals", Phys. Rev. A **94**, 013801 (2016).

[39] L. Veissier, M. Falamarzi, T. Lutz, E. Saglamyurek, C. W. Thiel, R. L. Cone, and W. Tittel, "Optical decoherence and spectral diffusion in an erbium-doped silica glass fiber featuring long-lived spin sublevels", Phys. Rev. B **94**, 195138 (2016).

[40] J. R. Klauder and P. W. Anderson, "Spectral diffusion decay in spin resonance experiments", Phys. Rev. **125**, 912–932 (1962).

[41] J. L. Black and B. I. Halperin, "Spectral diffusion, phonon echoes, and saturation recovery in glasses at low temperatures", Phys. Rev. B **16**, 2879–2895 (1977).

[42] W. Breinl, J. Friedrich, and D. Haarer, "Spectral diffusion of a photochemical proton transfer system in an amorphous organic host: quinizarin in alcohol glass", The Journal of Chemical Physics **81**, 3915–3921 (1984).

[43] L. Veissier, C. W. Thiel, T. Lutz, P. E. Barclay, W. Tittel, and R. L. Cone, "Quadratic zeeman effect and spin-lattice relaxation of Tm^{3+}:yag at high magnetic fields", Phys. Rev. B **94**, 205133 (2016).

[44] J. H. Davidson et al., "Measurement of the thulium ion spin hamiltonian in an yttrium gallium garnet host crystal", Phys. Rev. B **104**, 134103 (2021).

[45] C. W. Thiel, R. M. Macfarlane, Y. Sun, T. Böttger, N. Sinclair, W. Tittel, and R. L. Cone, "Measuring and analyzing excitation-induced decoherence in rare-earth-doped optical materials", Laser Physics **24**, 106002 (2014).

[46] M. l. G. Puigibert et al., "Entanglement and nonlocality between disparate solid-state quantum memories mediated by photons", Phys. Rev. Research **2**, 013039 (2020).

[47] H. De Riedmatten, M. Afzelius, M. U. Staudt, C. Simon, and N. Gisin, "A solid-state light–matter interface at the single-photon level", Nature **456**, 773–777 (2008).

[48] M. Afzelius and C. Simon, "Impedance-matched cavity quantum memory", Phys. Rev. A **82**, 022310 (2010).

[49] D. M. S. Johnson, J. M. Hogan, S.-w. Chiow, and M. A. Kasevich, "Broadband optical serrodyne frequency shifting", Opt. Lett. **35**, 745–747 (2010).

4

QUADRATIC ZEEMAN SPECTRAL DIFFUSION OF THULIUM ION POPULATION IN A YTTRIUM GALLIUM GARNET CRYSTAL

Jacob H. Davidson*, Antariksha Das*, Nir Alfasi, Charles W. Thiel, Rufus L. Cone, Wolfgang Tittel

The creation of well understood structures using spectral hole burning is an important task in the use of technologies based on rare earth ion doped crystals. We apply a series of different techniques to model and improve the frequency dependent population change in the atomic level structure of Thulium Yttrium Gallium Garnet (Tm:YGG). In particular we demonstrate that at zero applied magnetic field, numerical solutions to frequency dependent three-level rate equations show good agreement with spectral hole burning results. This allows predicting spectral structures given a specific hole burning sequence, the underpinning spectroscopic material properties, and the relevant laser parameters. This enables us to largely eliminate power dependent hole broadening through the use of adiabatic hole-burning pulses. Though this system of rate equations shows good agreement at zero field, the addition of a magnetic field results in unexpected spectral diffusion proportional to the induced Tm ion magnetic dipole moment and average magnetic field strength, which, through the quadratic Zeeman effect, dominates the optical spectrum

This chapter is submitted to Physical Review B.

*These authors contributed equally to this work.

over long time scales. Our results allow optimization of the preparation process for spectral structures in a large variety of rare earth ion doped materials for quantum memories and other applications.

4.1. PREAMBLE

The work detailed in this chapter represents an optimization of our process for crafting AFC quantum memories in Tm:YGG. Until recently creating a good AFC with the desired storage time and the best efficiency in our group has been considered as much art as science to correctly optimize the resulting memory. With this work, we gain the ability to work from known parameters such as laser power, laser linewidth, and a programmed sequence of optical pulses in order to predict the eventual shape of an AFC. With that process in hand, we can now optimize the shape of AFC quantum memories in order to maximize storage efficiencies, storage times, multi-mode capacity, or other figures of merit. It is also worth a mention that this process applies to other rare earth ion doped materials as long as spectroscopic properties such as the relevant level lifetimes and branching ratios are well understood.

4.2. INTRODUCTION

RARE-EARTH ion doped crystals (REICs) are interesting materials due to their long-lived excited states and their exceptionally long optical coherence times at cryogenic temperature [1, 2]. In particular, along with the possibility for spectral tailoring of their inhomogeneously broadened $4f^N$-$4f^N$ transitions, this makes them prime candidates for a number of applications in classical and quantum optics. Examples include laser stabilization, RF spectrum analysis, narrow-band spectral filtering, and quantum information storage and processing [2–7].

Thulium-doped Yttrium Gallium Garnet ($Y_3Ga_5O_{12}$, Tm:YGG) is one such material. Its $^3H_6 \leftrightarrow ^3H_4$ transition at 795 nm wavelength features an optical coherence time of more than 1 ms [8–10], which is one of the longest among all studied REICs. In combination with the accessibility of this transition—within the range of commercial diode lasers—this makes it a natural candidate for applications.

The quality of created features and the resulting consequences for associated applications are dependent on the spectroscopic properties of the dopant ions and their numerous interactions with other atomic components in their local crystalline environment [11, 12], the details of the optical pumping process, and the spectral and temporal profile of the applied laser pulses[13, 14]. Deep understanding of the relation between spectroscopic properties, optical control fields, and spectral diffusion dynamics has resulted in improvements of this process in a number of other rare-earth-doped materials including Tm:YAG, Eu:YSO, and Pr:YSO [15–17]. However, this important connection has thus far not been made for Tm:YGG.

In this paper, we track the evolution of population within the electronic levels of Tm^{3+} ions in YGG (see Fig. 4.2 for the simplified level scheme) by semi-continuous monitoring of spectral holes for many sequences of applied spectral hole burning pulses. The characteristic shapes and sizes of these spectral features are matched to a rate equation model that encompasses the ground ($^3H_6$), excited ($^3H_4$), and bottleneck ($^3F_4$) levels in

this material with associated lifetimes and branching ratios. At zero magnetic field, we see good agreement between our numerical model and measured results across many different pump sequences of varying duration, power, and spectral shape. With the addition of an external magnetic field, the agreement with our numerical model disappears as spectral diffusion from local host spins begins to dominate the shape of all spectral features over long timescales. We characterize the nature of this unexpected behavior and expand our model accordingly by adding a spectral diffusion term to account for a quadratic Zeeman interaction with present noisy magnetic fields [18, 19].

The letter is structured as follows: In section 4.3 we describe the experimental setup used to collect our measurements. In section 4.4 we detail the atomic level structure in Tm:YGG and introduce spectral hole burning, the workhorse of our investigations, to select a known set of atomic populations. In section 4.5 we introduce and apply a rate equation model which shows good agreement to the measured spectral hole features. In section 4.6 we detail the use of adiabatic pulses to shape spectral holes at zero magnetic field with the goal of creating high-resolution features. Section 4.7 shows uncontrolled changes to created spectral holes in the presence of magnetic fields and connects these noise effects to the quadratic Zeeman effect. Section 4.8 extends this quadratic Zeeman connection to the characterization of spectral diffusion results that differentiates the measured results from those predicted by our model over longer timescales.

4.3. EXPERIMENTAL SETUP

To measure spectral holes, from population storage in various atomic levels, over different timescales in Tm:YGG we use the setup detailed in Fig. 4.1. A CW diode laser tuned to the ion transition frequency at 795.325nm [20] is locked to a reference cavity resulting in a linewidth of roughly 5kHz [21]. To craft short pulses of high extinction ratio, its continuous wave emission is directed to a free space AOM. The sinusoidal driving signal of the AOM is mixed with a signal modulated by an arbitrary function generator, which allows programmable control of the transmitted pulse amplitude for the first order light.

After the amplitude control, the pulsed light is directed to a fiber-coupled phase modulator driven using arbitrary waveforms for serrodyne frequency shifting and more complex chirped pulse shapes as detailed in section 4.6. The optical signals are then sent through a polarization controller to a 1% Tm:YGG crystal grown by Scientific Materials Corp. and housed in a pulse tube cooled cryostat at 500-700mK. A superconducting solenoid centered on the crystal applies a homogeneous magnetic field from 0-2T(using about 1mA/mT of current) along the crystal's <111> axis. Signals transmitted through the crystal are directed to a fiber-coupled photo diode and recorded for subsequent analysis

Experimental control is handled on a number of different time scales via custom python scripts that ensure signals are created at the correct moment [22]. For sequencing on timescales of longer than a second, the built-in python timing functions are used to adjust the experiment. On all timescales shorter than seconds, timing is handled by preprogramming a pulse generator that produces correctly timed trigger signals for the various devices. Waveforms for the arbitrary voltage signals are generated by custom scripts and uploaded to the respective devices for arbitrary control of instantaneous pulse frequencies and amplitudes.

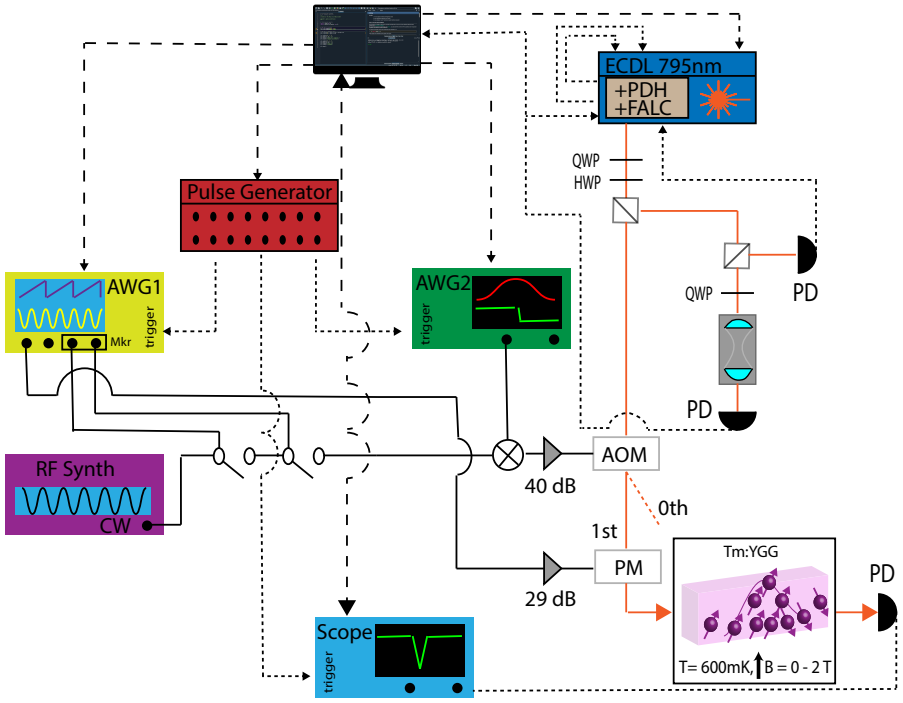

Figure 4.1: Schematic of the experimental setup. A PC programs a sequence on a pulse generator (SpinCore Pulseblaster) with nanosecond timing resolution that produces a set of trigger pulses for all devices. Waveforms written to an arbitrary waveform generator (AWG1,Tektronix AWG 70002A) voltage channel, are subsequently amplified (SHF S126 A), and drive an electro optic phase modulator (PM) to generate side bands on the laser light at arbitrary frequencies. The AWG marker channels drive a set of home-built electrical switches which gate the drive signal of an acousto-optic modulator (AOM) to create short pulses from the laser light. This gated AOM signal is mixed with fast arbitrary voltage pulses(AWG2,Tektronix AFG 3102), amplified (Mini-Circuits ZHL-5W-1+), and sent to an acousto-optic modulator (AOM Brimrose 400MHz) to synthesize controllable-amplitude laser pulses with rise times as short as 2.5ns. We use a single light source (Toptica DL Pro 795nm) for different tasks (optical pumping, pulse generation, etc). The laser frequency is set via a wavemeter (Bristol 871) and locked to a thermally and acoustically isolated high finesse optical cavity (Stable Laser Systems) via the Pound-Drever-Hall method and a fast feedback loop acting on the laser current and piezo voltage (Toptica PDH and FALC Modules). Transmitted signals from the crystal are directed to a variable-bandwidth photodetector (NewFocus 2051) and displayed on an oscilloscope (Lecroy Waverunner 8100A) configured by the PC and synchronized with the experimental sequence by a trigger signal.

4.4. TM:YGG SITE AND LEVEL STRUCTURE

Garnet crystals such as YGG have cubic crystal structure with O_h^{10} space group symmetry, which yields six Tm^{3+} ion substitution sites, each with D_2 point group symmetry[9, 23–25]. The magnetic and optical behavior of Tm^{3+} ions in each of these sites is identical but the crystal structure leads to effective in-equivalence between the sites due to six different orientations that the ion and its entire local environment can take within the lattice [26]. However, for a few specific directions relative to the crystalline axes, ions

at in-equivalent sites can be cast into classes that share the same projections of applied electromagnetic fields ($\vec{E}, \vec{B}$) onto their local site axes.

Given the orientation of our magnetic field, parallel to the crystalline $\vec{B}$ || <111> axis, we cast the ions into two different classes as depicted in Fig. 4.2 a. The ions in each separate class experience different magnetic field projections onto the axes in their local frame. One class features magnetic field projections along the ion's local X and Z axes (blue), and the other projections along the local Y and Z axes (red). This difference becomes evident from a simple spectral hole burning experiment, which we use to introduce the remaining results of the paper.

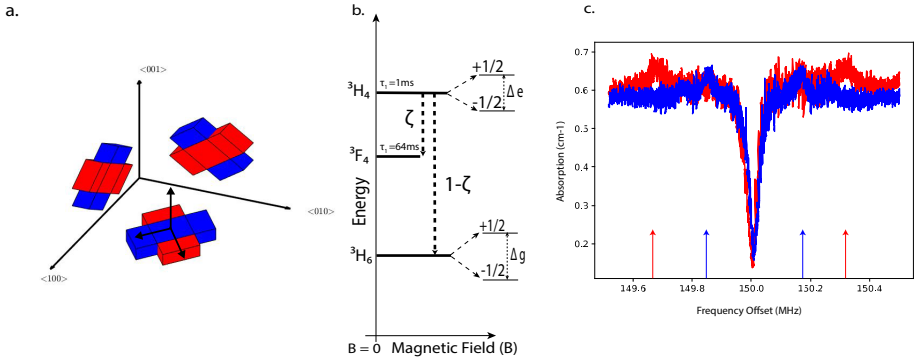

Figure 4.2: **a.** Depiction of the six ion substitution sites relative to the cubic crystal cell. For a magnetic field along the crystalline <111> axis the sites are cast into two classes of different field projection, shown in red and blue. Small black arrows indicate the local site X,Y,Z, axes for the red site in the <100> <010> plane. **b.** Energy level diagram of Tm:YGG. **c.** A pair of hole burning spectra with the main spectral hole pictured in the center. Each hole, shown in an associated color to part **a.**, is burned with a polarization that selects one of the two classes of ions and produces anti-holes with different splitting (indicated by the colored arrows). Additional modulations of the optical depth outside the hole originate from mistakes in the crystal orientation during fabrication.

In spectral hole burning, a long optical pump pulse excites the atomic population in a narrow spectral window within an inhomogeneously broadened absorption line. Excited ions subsequently decay — either back into the original state, or into another energy level that often belongs to the electronic ground state manifold. Scanning a weak laser beam over a spectral interval centered on the frequency of the original pump pulse reveals sections of decreased and increased absorption — so-called spectral holes and anti-holes. Spectral holes occur at frequencies of reduced ground-state population, i.e. with offset $\Delta = 0$ (for the central hole), $\Delta = D_e$ (for the side hole), and anti-holes can be observed whenever the ground-state population is increased, which happens at $\Delta = D_g$ and $\Delta = D_g \pm D_e$. Here, D_g and D_e are ground and excited state splittings. Consult Ref.[13, 27, 28] for more details on spectral hole burning.

In our case, the ground and excited state splittings depend on the magnitude and direction of the applied magnetic field — which vary for each class of Tm ions [26]. At 7.5 mT we recorded a pair of hole-burning spectra, shown in Figure 4.2 c, for orthogonal pumping polarizations. This allowed us to selectively address ions in either of the two classes. We found two sets of anti-holes, each of which split according to the different

field projections experienced by the two classes of Tm^{3+} ions. This ability to select out a single class of ions becomes important in section 4.8 as spectral diffusion depends on the magnetic projection on each specific class of ions.

4.5. MODELING RESULTS USING THREE-LEVEL RATE EQUATIONS

To further understand the effects of a given hole-burning process on our REIC ensemble we turn to solutions of the Maxwell-Bloch equations that describe the interaction of light with one or many atomic systems. These differential equations can be quite difficult to solve, given the complexity that there does not exist a single fixed Rabi frequency to drive all ions [29]. In the limit of excitation pulse lengths much shorter or much longer than T_2 the rate equation approach has been shown to be an effective model [30]. Thus for the case of Tm:YGG, due to the long T_2 and low optical depth we reduce the Maxwell-Bloch equations to a set of rate equations that describe the conserved total atomic population and how it flows through the different available levels as a function of time [14].

Note that in the case of narrowband excitation of an inhomogeneously broadened transition where only a certain portion of atoms are driven, frequency dependence must be added. Following [14] and [15, 31] we describe the dynamics of our atomic ensemble with equations 4.1-4.3.

$$\frac{\partial n_g(t)}{\partial t} = R(\Delta)(n_e - n_g) + \frac{1-\zeta}{T_e} n_e + \frac{1}{T_b} n_b \tag{4.1}$$

$$\frac{\partial n_e(t)}{\partial t} = R(\Delta)(n_g - n_e) - \frac{1}{T_e} n_e \tag{4.2}$$

$$\frac{\partial n_b(t)}{\partial t} = \frac{\zeta}{T_e} n_e - \frac{1}{T_b} n_b \tag{4.3}$$

This system of coupled differential equations describes the relative change of atomic population, $n_{(g,e,b)}(\Delta)$ in three ion levels as a function of time. The branching ratio ζ determines how much population decays from the excited state $|e\rangle$ through the bottleneck state $|b\rangle$ before reaching the ground state $|g\rangle$ with respective level lifetimes T_e and T_b. To drive the system, a frequency-dependent excitation rate $R(\Delta)$ is added which characterizes the applied pulses of light used for hole burning. For Tm:YGG, the level lifetimes and branching ratios are well known at zero magnetic field [20] leaving only one unknown, the frequency-dependent optical pumping rate which has to be matched with measured data.

This pumping rate $R(\Delta)$ is a function of both the individual ion properties and the applied sequence of laser excitation or burning, pulses. Again from [15],

$$R(\Delta) \propto \gamma * \mathbb{F}(\Delta)_{Opt} \tag{4.4}$$

is a convolution of the two factors, the homogeneous linewidth γ of the ionic transition and the Fourier spectrum of the applied pulse sequence $\mathbb{F}(\Delta)_{Opt}$. For the case of Tm:YGG the homogeneous linewidth of the ions is expected to be narrower than 600Hz

[20]. For any $\mathbb{F}(\Delta)_{Opt}$ with features greater than the homogeneous linewidth of the ions this convolution is dominated by the Fourier spectrum of the pumping pulse, which is determined by laser and sequence characteristics such as pump power, pulse duration, pulse spacing, and spectral line-shape.

We perform many different hole-burning experiments with differently timed burning sequences of various powers, durations, and waiting periods. See figure 4.3 a. With these parameters set, and the known lifetimes and branching ratios of Tm:YGG, we numerically solve the rate equations above for all times in the burning sequence after setting the initial conditions before pumping to $n_g = 1$(i.e. after initializing all population in the ground state). An example is shown in Figure 4.3 b, showing the predicted development of a spectral hole over time for some chosen $R(\Delta)$ parameter. The measured evolution of the spectral hole after the same series of pumping pulses and waiting times is shown in Figure 4.3 c where the spectral hole is read out after every burn pulse to capture the evolution.

As the optical depth of a measured spectral hole is proportional to the ground state atomic population left to absorb we normalize the remaining population using the optical depth before any pumping has occurred and match the results generated by experiment and by numerical simulation for a particular burning sequence [14, 15]. Note that since we do not have an analytical function that describes the solution to the system of rate equations, the matching is not a fit that outputs a mean standard error. However, as a "goodness of fit" metric, we calculate the point-wise average difference between the measured and simulated surfaces. Solutions and measurements are shown for a few different times in Figures 4.3 d,e to demonstrate close agreement for matched parameters. More examples of different burning sequences, a discussion of the resulting holes with respect to the level lifetimes, and a note on the power dependence of the laser line shape are included in the supplementary information.

We consider many different $R(\Delta)$ functions to validate our model, only one of which creates the closest match with all the measured results. This allows us to uniquely identify the $R(\Delta)$ parameter as a property of our laser source and its interaction rate with the ions.

All burning sequences assume a source with a Lorentzian-shaped laser line of $\nu = 5$ kHz linewidth and an excitation rate amplitude a, tunable between approximately 300 Hz and 2.5 kHz, via AOM drive power. This yields an $R(\Delta)$ function of the form

$$R(\Delta) = a\frac{\gamma^2}{\gamma^2 + (\Delta - \Delta_o)^2} \quad \text{for} \quad a \in [0.3, 2.5]kHz, \gamma = 0.005MHz, \Delta_o = 150MHz \tag{4.5}$$

where Δ_o is the detuning from the thulium absorption line center.

Thus our model for population change driven by this known optical spectrum allows us to predict the size and shape of any spectral feature resulting from a given burning sequence in this material at zero external magnetic field. This strategy should extend to other materials as long as the relevant branching ratios and lifetimes are known.

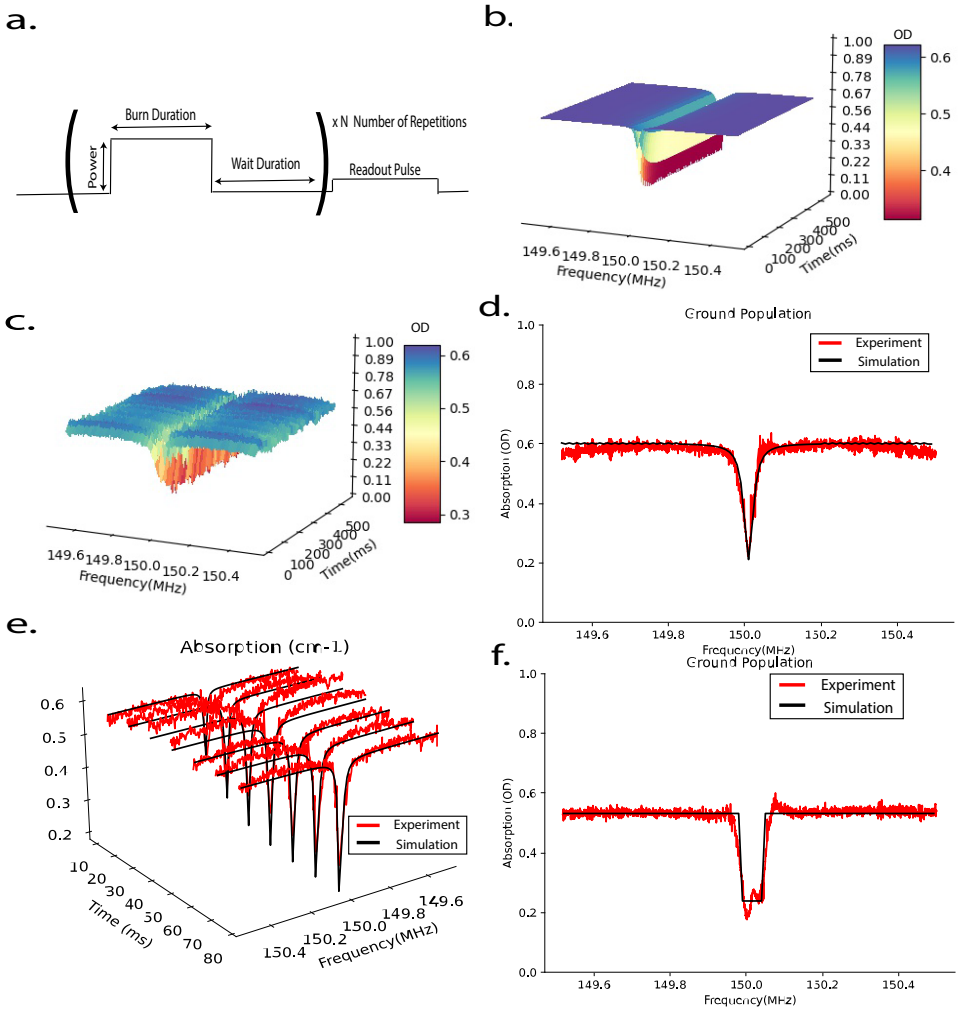

Figure 4.3: **a.** Simple hole-burning sequence used throughout the paper. **b.** Evolution of a spectral hole simulated using Eqs. 4.1-4.3. The hole is detuned by 150MHz from the peak of the Tm absorption line and develops slowly in time. **c.** Measured hole evolution. The hole-burning sequence is as in b. The hole deepens as more burn pulses are applied. **d.** The final hole of both methods(experiment and simulations) after 50 cycles of alternating 1ms long pump pulses and 10ms waiting periods. **e.** Overlaid slices at many times throughout the burning process.**f.** Square-shaped spectral hole generated using hyperbolic secant burn pulses. Modulations at the bottom of the hole are due to imperfections in the burning pulses, and the square line shows a comparison to modeled results from a perfectly square $R(\Delta)$ function of matching bandwidth.

4.6. ADIABATIC PULSE SHAPING

To confirm our measurements, and exclude spectral hole broadening mechanisms from the optical pumping process, we sought to change the spectral shape of our excitation light and create controllable changes to the width and shape of the resulting spectral

holes. We use adiabatic pulse shaping to isolate the shape and width of created spectral features for further optimization while continuing to match to solutions of our predictive model.

An important method for controlling the shape and width of a desired spectral feature stems from an early goal of NMR to design a pulse which creates highly efficient yet highly selective population inversion [32]. The resulting coherent population inversion over a narrow frequency bandwidth is described by a unique analytical solution to the Maxwell-Bloch equations [33]. This method is known as a hyperbolic secant pulse and relies upon slow adiabatic tuning of the amplitude and phase of the driving pulse. This results in the elimination of unwanted frequency components around the desired bandwidth, and the creation of a pulse with a particularly square spectrum [14, 34]. For REICs, hyperbolic secant pulses were first considered for quantum computing in order to create high fidelity π pulses for narrow bandwidth ensembles of ions [17, 35].

The original Maxwell-Bloch solutions call for simultaneous slow modulation of the amplitude and phase, each with a different shape. This is equivalent to modulation of the pulse amplitude and frequency shifting during the duration of the pulse [32]. From a hardware standpoint the problem becomes creating fast electronic control of the amplitude $A(t)$, via AOM voltage, and instantaneous frequency $f(t)$, via phase modulator drive, as in [16]. To account for the separate elements responsible for each modulation, a variable delay was added to the amplitude modulation to ensure that the correct portion of each pulse is temporally aligned with the corresponding frequency shift.

This method of creating spectral features is in contrast to the common method of linearly swept serrodyne modulation [34, 36, 37]. For broadband features both methods are fairly similar, but for creating narrow-band spectral features on the order of the pump laser linewidth, the spectrum of the adiabatic pulse shows much steeper rising and falling edges than that of linearly shifted pulses.

To show the clear difference in spectral hole shape using this method, we carry out the same hole burning experiment as above with the key difference being that each burning pulse is subject to adiabatic amplitude and frequency modulation. The simulated and measured results of these hole burning experiments are compared in Figures 4.3 f. The hole shape clearly changes corresponding to the altered—squarer—excitation spectrum $R(\Delta)$. The shape of the resulting hole spectrum is controllable in terms of width by altering the frequency range and speed of the hyperbolic secant pulse modulations. Though the lower limit of hole width is still related to original laser linewidth, adiabatic modulation suppresses Lorentzian wings of the spectrum, and will allow for added power in the burning process.

4.7. MAGNETIC NOISE

With the ability to control the frequency chirp range and the amplitude and duration of each burning pulse, creation of many possible spectral features, at zero magnetic field, is well understood from the model in Eqs. 4.1-4.3. However, the lifetime of the $^3F_4$ the bottleneck level in Tm:YGG creates an upper limit for burning deep yet sharp holes with a reasonable laser power, see Supplementary Material. To improve the depth and lifetime of the resulting features, we now add a magnetic field to create a longer-lived bottleneck state; a ground state spin level with a lifetime of seconds[26, 38].

It is worth noting at this point that $R(\Delta)$ is the main term that determines frequency dependence in the model. Thus, with applied magnetic field an identical bandwidth of initial population is excited by the same pulse sequences carried out at zero field. Ideally, only the duration of the subsequent decay path from the excited state can change as magnetic fields are applied leading to deeper longer lived spectral holes. However, it will be seen in the following section(s) that though we can initially create spectral features of a shape matching the zero field case, quadratic Zeeman coupling between magnetic field noise and the local spin environment of the Tm ions creates significant changes to these features over long time scales.

With the addition of a magnetic field the ground and excited states of Tm:YGG each split into spin states with a spin-Hamiltonian given by [26]. The created ground state spin level has a much longer lifetime than the $^3F_4$ state previously used as the bottleneck level, prolonging eventual decay to the ground state [39].

A significant portion of the electronic population from the $^3F_4$ level decays to the additional spin level before reaching the original ground state, creating an equivalent three-level system that should be governed by similar rate equations, albeit with extended bottleneck level lifetime [15]. In addition, to ensure that population accumulates in this level, waiting times between burn pulses must be on the order of the $^3F_4$ state lifetime to prevent population storage in the $^3F_4$ state from where it can decay to the original ground state much more quickly. Measuring the created spectral holes over these longer burning and waiting sequences —without significance without applied field— we find important differences compared to the modeling. To assess these differences, spectra in this section and in section 4.8 are taken post-burn sequence on a longer timescale than those presented in the previous sections. More specifically, we measure a created hole periodically every 11 seconds for minutes. Each hole is fitted to a Lorentzian to determine the center, depth, and width of the spectral feature.

As the magnetic field strength is increased we observe a clear impact of magnetic field noise on the width and center frequency of the spectral holes. This is evident from figure 4.4 a. Here the hole is initially centered at the programmed frequency, but the shape and center proceed to change in an uncontrolled manner. The magnitude of these changes falls within the bounds of magnetic field noise caused by variations of the solenoid supply specified by the manufacturer.

To confirm the origin of the measured effect we create a narrow spectral hole at a fixed magnetic field. A short time after burning has been completed, we alter the field by a fixed amount of 1.6 mT, the smallest increment possible with our experimental setup, and measure the subsequent changes to the hole. We expect a splitting and shifting [40] from the linear and quadratic Zeeman terms of the ion spin-Hamiltonian as ions change optical transition frequency in the altered field. The results of these measurements are depicted in Figs. 4.4 b-f. We find that the splitting and shifting of the spectral hole increases notably as the value of the initial magnetic field was changed from 0.1 to 1.5 T, for constant field changes of 1.6mT.

The measured values of the center shift and splitting of the pair of resulting holes are in good agreement with expectations from the quadratic and linear components of the hyperfine tensor for these ions [26]. The supplementary material contains details for calculating the expected shifting from the hyperfine tensors and the applied magnetic

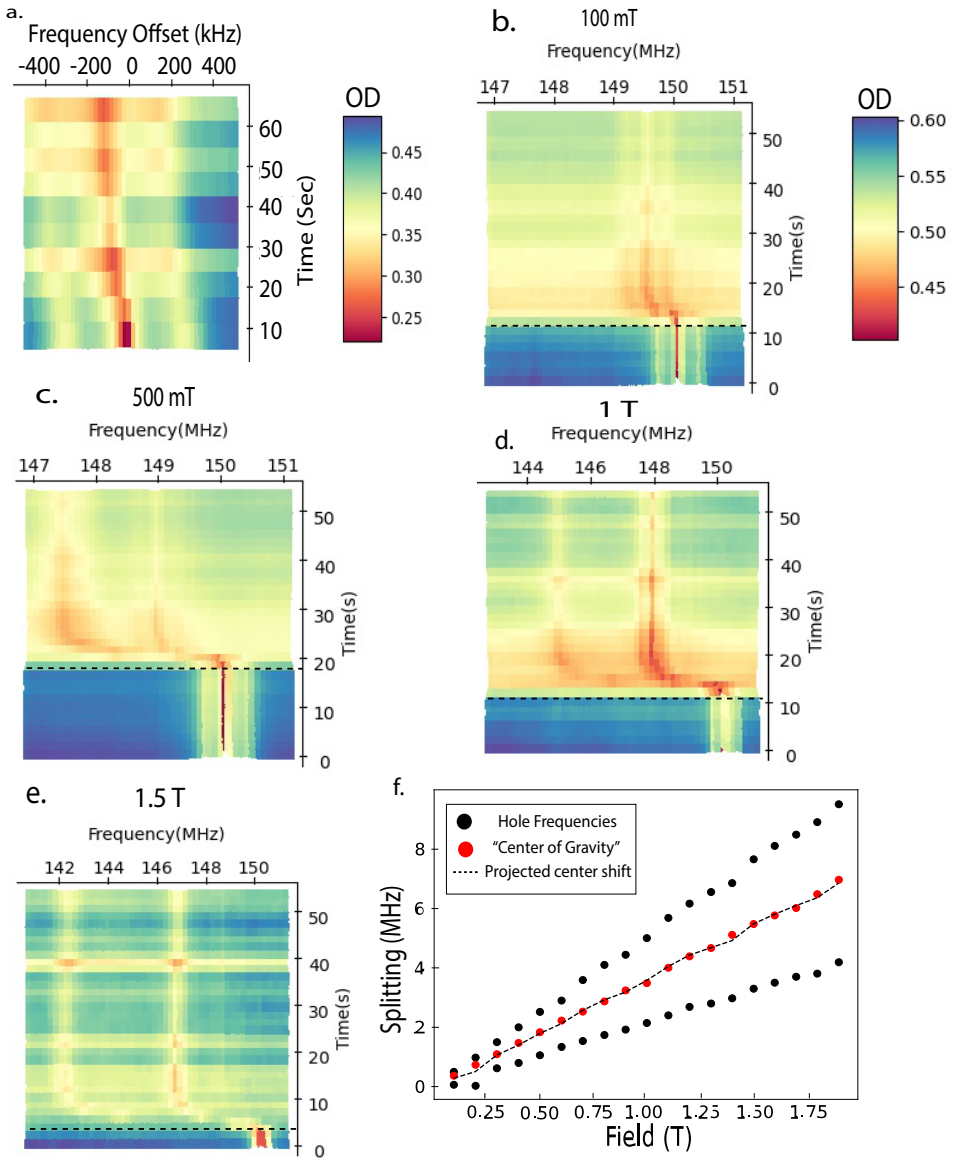

Figure 4.4: **a.** Spectral hole crafted at 1.8 T, and read out repetitively over the course of one minute. **b.-e.** Shifting adn splitting of the hole features for a fixed change of 1.6mT at initial magnetic fields from 0.1,0.5,1,1.5 T. The dashed lines show the moment when the small change in field was made. **f.** Hole center frequency shift and splitting into separate hole features after a fixed change of 1.6mT at initial magnetic fields from 0.1-2 T. The dashed line is the center shift projected by the hyperfine tensors for this magnitude of field change. The magnitude of the center shift and the splitting both grow as expected from [26] for higher absolute fields.

field change. From these measurements, we estimate the field fluctuations in our system to be a factor of 10 smaller than our applied 1.6 mT field change, leading to the shifting of the hole center. The implication is that at high magnetic fields, noise on the order of μT causes many kilohertz of change in the center hole frequency. This result will prove critical for understanding and creating narrow spectral features at high magnetic fields.

4.8. SPECTRAL DIFFUSION

In addition to the central frequency shift, all measured holes are broadened compared to expectations from the burning parameters modeled and tested at zero field, a telltale sign of spectral diffusion [12].

Magnetic field dependent spectral diffusion of spins is well understood in the field of rare earths, although it has more often been considered for the case of Kramers, rather than non-Kramers ions [19]. The problem is often cast in terms of interactions in which nearby spins that have not been excited swap energy with excited members of the ensemble leading to a general loss of coherence and a spreading, or broadening, of spectral features in time [41, 42]. Both magnetic field and sample temperature play enormous roles as they both mediate how much energy is being interchanged directly through spin-spin interaction or through coupling to host phonons[43]. On short to medium timescales the characteristic rate and magnitude of these processes are often measured via two and three-pulse photon echo that allow for spin interactions during their variable delay times[19]. For longer timescales spectral hole burning can accomplish a similar task by mapping the change of the hole shape and size as a function of time, magnetic field, and temperature [12].

By adjusting the polarization of the pump light, we first isolate ions with a particular spin splitting at a certain magnetic field, as discussed in section 4.4. Again, we perform spectral hole burning measurements where burning pulses and waiting periods are timed to guarantee population arrives at the desired spin level. Once hole burning is complete, the hole is read out after varying waiting times using, as above, a weak probe in order to leave the hole unperturbed. We determine (i.e. fit) the widths of all holes for a series of different magnetic field amplitudes. Width change as a function of time can be described by [19]

$$\Gamma_{hole} \propto \Gamma_o + \frac{1}{2}\Gamma_{SD}(1 - e^{-R_s t_{delay}}). \tag{4.6}$$

Here, Γ_o is some initial hole width given by $R(\Delta)$ of the burning process, which broadens in time. The spectral diffusion approaches a maximum value of Γ_{SD} at a characteristic rate given by R_s. The functional form of the magnetic field and temperature dependence for Γ_{SD} and R_s can be used to link spectral diffusion to a specific broadening mechanism [19, 44, 45].

The first portion of evidence for determining the source of the measured diffusion is the different behavior of each magnetic class of ions. Shown in Fig. 4.5 a is the hole width of each such class as a function of time for an applied field of 500mT. For the same external field, each class broadens at a different rate. However, when different fields are applied, such that the Zeeman splittings of each class are roughly equivalent, the broadening occurs at the same rate, see Fig. 4.5 b. This contrast likely rules out contribu-

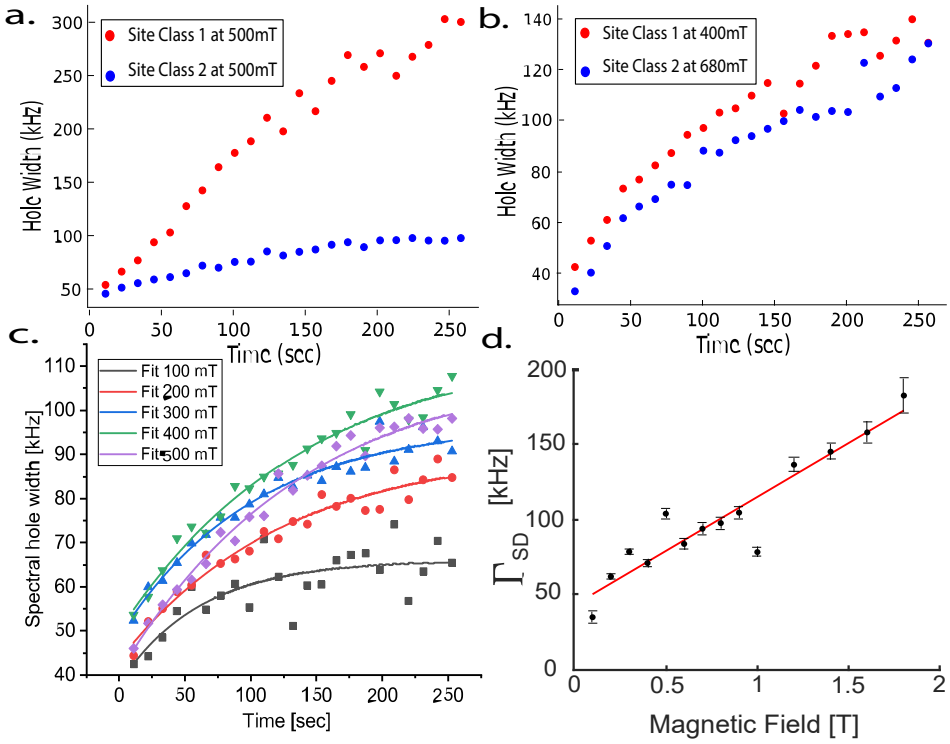

Figure 4.5: **a.** Spectral hole widths for ions in both magnetic classes as a function of time at 500mT. The class of ions with the larger magnetic field projection shows significantly more spectral diffusion. **b.** Spectral hole widths for ions in both magnetic classes as a function of time where the applied magnetic field for each class of ions creates roughly equivalent splitting. The spectral diffusion is comparable. **c.** Fitted Hole width versus time for a single class of ions at a series of different magnetic fields. **d.** Linear fit to the variation of Γ_{SD} as a function of magnetic field.

tions of two-level systems [39] on this time scale, which is likely to be located randomly throughout the material without an orientation-dependent response. Instead, the diffusion appears to depend upon the magnitude of the created magnetic dipole moment of the Tm ions.

To further isolate the cause of the diffusion we analyze the behavior of a single class of ions as a function of the applied field. Utilizing the model in Eq. 4.6 we fit Γ_{SD} and R_s exclusively for each magnetic class of ions where the functional form of Γ_{SD} is given by [19],

$$\Gamma_{SD}(B,T) = \Gamma_{max}\,\mathrm{sech}^2\left(\frac{g_{env}\mu_B B}{kT}\right) \tag{4.7}$$

Here g_{env} is the g-factor of spins in the local crystalline environment, μ_B is the Bohr magneton, B is the applied field, k is the Boltzmann constant, T is the sample temperature, and $\Gamma_{max}(B)$ is the full-width half max of the broadening of the optical transition due to external sources.

Species	Concentration	Effective g factor	Average distance (r)	Average Field (B)
$^{169}Tm^{3+}$	1%	0.0077	17 Å	500 nT
^{71}Ga	40%	0.00071	2.6 Å	15 μT
^{69}Ga	60%	0.00092	2.6 Å	19 μT
^{89}Y	99%	0.00014	4 Å	850 nT

Table 4.1: Magnetic fields experienced at an average Tm ion site due to spin flips of the elemental species in the crystal. Estimated distances are in agreement with measured data from YAG [46]. Only the gallium spins match the order of magnitude of the measured magnetic variations.

For non-Kramer's ions in general, and all atomic species in the YGG host, since the g-factors, g_{env}, are quite small, the thermal distribution of population in various spin levels remains nearly constant for the temperatures and applied fields used in this work, making the sech^2 factor in Eq.3.6 effectively constant as well. Any field dependence of Γ_{SD} can then be attributed to the field dependence of $\Gamma_{max}(B)$. As shown in Fig. 4.5 d we find Γ_{SD} to increase as the magnetic field increases while R_s remains fairly constant for the measured fields. Inspired by [19, 45] we fit this behavior using a functional form of $\Gamma_{max}(B)$ that relates the optical transition broadening to the quadratic Zeeman effect.

$$\Gamma_{max}(B) = g_j^2 \mu_B^2 B \cdot |\mathbf{\Lambda_e} - \mathbf{\Lambda_g}| \cdot B_{Noise} + \Gamma_{max}(0). \tag{4.8}$$

Here, g_j is the electronic g factor for each level, μ_B the Bohr magneton, $\mathbf{\Lambda}_i$, $i \in \{g, e\}$ is the hyperfine tensor for the ground and excited states in the transition, B is the applied magnetic field, and B_{Noise} the width of the field distribution around each experimentally set value due to flips of local host spins or external noise. All factors in this expression are known save this empirical B_{Noise}, which is fit to a value of 87±20 μT using the data of Fig. 4.5 d.

Following calculations from [47] and using a model of the YGG crystal cell from [48] we estimate the magnetic field variation at an average Tm ion site given the concentrations, unit cell dimensions, and corresponding g-factors of each host crystal constituent. Table 4.1 contains estimations of magnetic fields at a potential Tm ion site due to spin flips from each of the crystal constituents. Considering possible contributors, the low Tm ion concentration of this crystal means the average distance to another dopant thulium is likely too small for Tm-Tm interactions to cause noise of this magnitude. Yttrium, though fully concentrated, is also too weakly magnetic. The most likely explanation is the presence of a fully concentrated bath of local gallium spins, each with a moderate nuclear magnetic moment. An additional contribution from a noisy current supply used to power the superconducting solenoid that creates the magnetic field across the crystal, among other factors stemming from geometrical concerns and heterogeneous spin species [49], may explain the mismatch between our rough estimations of spin-flip noise, and the fitted field variations.

4.9. CONCLUSION

We conducted a series of spectroscopic measurements that lead to a detailed understanding of how to create high-resolution spectral features using Tm:YGG. The possibility for controlling pump field amplitude, frequency chirp, pulse duration, and pulse power gives a number of experimental handles with which to optimize the shape of the desired spectral feature. For zero magnetic field, experimental results were shown to be in good agreement with predictions from a three-level, frequency-dependent, rate equation model for various sets of input pulses shorter than the transition lifetime. However, when applying a similar model to a three-level system that includes a ground state spin level split by the magnetic field, magnetic noise, and spectral diffusion dominate the resulting features over long timescales. We attribute large shifts to each ions optical transition frequency due to the quadratic Zeeman effect in combination with time-varying magnetic fields as the likely cause of the diffusion. This in-depth analysis will aid applications that employ spectral features created using Tm:YGG and other rare earth-doped crystals such as spectral hole-based laser stabilization, RF frequency analysis, and optical quantum memories.

4.10. SUPPLEMENTARY MATERIAL

4.10.1. MORE EXAMPLES OF DIFFERENT BURNING SEQUENCES

In the main text, we show examples of modeled and experimentally created spectral holes using a single burning process. However, the good agreement between these two methods extends to a large variety of create procedures. We measured holes created using burn pulses with 5 different optical powers, with 2 different durations, and 4 different waiting times giving us more than 40 individual experiments with which to match behavior and predictions.

4.10.2. HOLES AND LEVEL LIFETIMES

All the cases listed in the previous section showcase the behavior of spectral holes relative to the different level lifetimes. They are worth a deeper look. We measure only a pair of burning times, 100us and 1ms, as burning pulses longer than around 1 ms were observed to heat the crystal, and the Fourier transform. For burning pulses of each length, we examine a set of different waiting times between the pulses of the sequence shown in Fig 4.3 a: 1ms, 10ms, 50ms, and 100ms. Each is selected for a reason. One millisecond is on the order of the excited state lifetime and is much shorter than the bottleneck lifetime. Ten milliseconds is much longer than the excited lifetime and much shorter than the $^3F_4$bottleneck lifetime. Fifty milliseconds is much longer than the excited and on the same order as the bottleneck lifetime, and 100ms is much longer than both lifetimes.

As the waiting time approaches the bottleneck level lifetime the additive nature of multiple burn pulses starts to disappear and the hole depth reaches a much smaller steady state. This can be seen from Fig. 4.6 a-c. When the waiting time exceeds the bottleneck lifetime we are essentially re-pumping the same population with each burn pulse, interacting with a nearly unchanged material absorption profile. For waiting times on the order of the excited state lifetime, we see a slight broadening of the hole due to power broadening as well as frequency shifts caused by excited ions within the pump

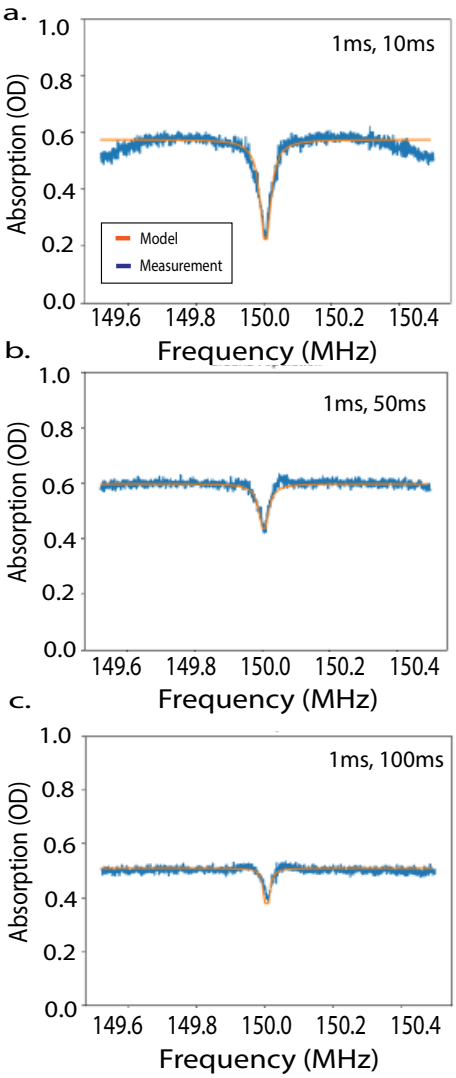

Figure 4.6: Spectral holes after 50 cycles of 1 ms burning separated by **a** 10 ms waits, **b** 50 ms waits, **c** 100 ms waits. The hole decreases in total depth because the population decays from the bottleneck level before the next pumping step.

bandwidth [17, 35]. This indicates that the optimum wait duration using which to create features is longer than the excited state lifetime so that most pumping occurs without the population in the excited state, but still much shorter than the bottleneck level lifetime to allow the population to accumulate in the bottleneck over many successive burning pulses.

4.10.3. POWER DEPENDENCE DUE TO MODEL NON-LINEARITY

Of the many measured data sets, a key portion involves the same optical pumping sequence with a series of different optical powers, See Fig. 4.7. This tuning is done by changing the peak-to-peak amplitude of the AOM driving signal over a range of voltages. Different initial laser line-shapes, $R(\Delta)$ with different amplitudes broaden the resulting holes at different rates. This study allowed us to determine the spectral shape of our applied $R(\Delta)$ function by comparing measured results to the scaling predicted by our model. First, in Fig. 4.7 a-e. we show a series of hole-burning experiments conducted with different optical powers using our un-modulated laser. The clear broadening of the spectral hole is not power broadening as in [14] but rather an effect due to the Lorentzian shape of the applied laser line. With increased amplitude the wings of the Lorentzian shape gain the ability to efficiently change ground state population, broadening the resulting hole. Additionally, Fig. 4.7 b. shows the scaling of a spectral hole for hyperbolic secant modulated pulses using a burning sequence with matching timing as above. As seen in figure 4.7 f-j, the broadening is nearly absent because the pulse modulation reshapes the applied $R(\Delta)$ function into a square shape that does not possess wings that strengthen with added burning power. This is the more desirable scaling, so that added power results in a higher excitation rate and deeper rather than broader spectral holes.

4.10.4. EXPECTED QUADRATIC ZEEMAN SHIFTING BEHAVIOR

First, we can calculate the initial frequency of the inhomogeneous line for some initial field magnitude and orientation. This is given by the difference between the shift of the ground (D_g) and excited(D_e) states.

$$D_J = \frac{g_j \mu_B}{2A_J}[(\gamma_{J,x} - \gamma_n)B_x^2 + (\gamma_{J,y} - \gamma_n)B_y^2 + (\gamma_{J,z} - \gamma_n)B_z^2] \tag{4.9}$$

Here, g_n is the nuclear gyro-magnetic ratio of thulium, β_n is the nuclear magneton, g_J is the electronic g factor for each level, μ_B is the Bohr magneton, and A_J is the hyperfine interaction constant, and $B_{(x,y,z)}$ the field components in the local frame of the ions.

Then the initial hole is at a frequency $\Delta_i = \frac{D_{ei} - D_{gi}}{\hbar}$ Calculating a $\Delta_f = \frac{D_{ef} - D_{gf}}{\hbar}$ using the final field magnitude and orientation we arrive at the projected shift $\Delta_f - \Delta_i$ in hole center frequency due to the quadratic Zeeman effect.

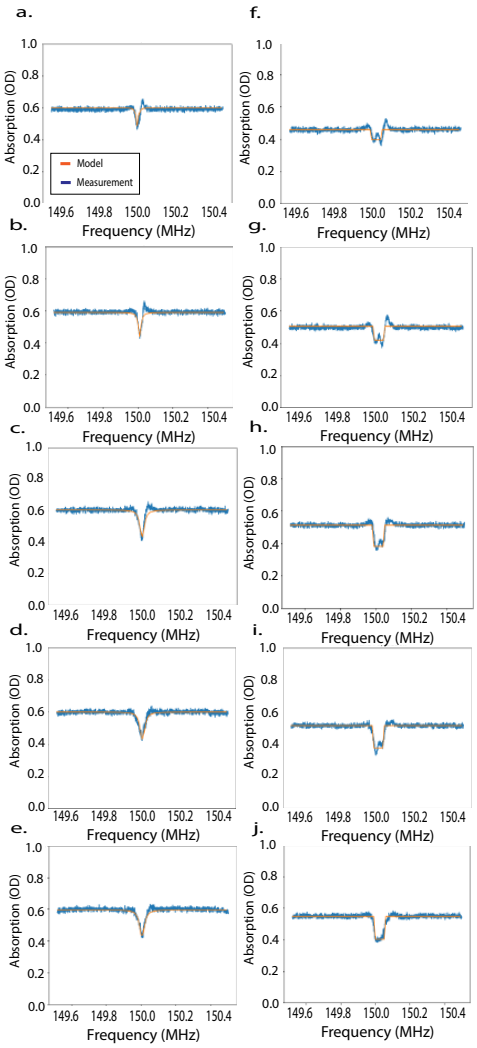

Figure 4.7: **a-e.** A series of spectral holes after 50 cycles of 1 ms burning separated by 50ms waiting between for five linearly increasing optical powers. Points(blue) are measured spectral holes, with line (orange) results of the rate equation model for this sequence and the pumping line-shape. **f-j.** A similar experiment, but each burn pulse is now a hyperbolic secant pulse.

BIBLIOGRAPHY

[1] W. R. Babbitt et al., "From spectral holeburning memory to spatial-spectral microwave signal processing", Laser Physics **24**, 094002 (2014).

[2] W. Tittel, M. Afzelius, T. Chaneliére, R. Cone, S. Kröll, S. Moiseev, and M. Sellars, "Photon-echo quantum memory in solid state systems", Laser & Photonics Reviews **4**, 244–267 (2010).

[3] P. B. Sellin, N. M. Strickland, J. L. Carlsten, and R. L. Cone, "Programmable frequency reference for subkilohertz laser stabilization by use of persistent spectral hole burning", Opt. Lett. **24**, 1038–1040 (1999).

[4] P. B. Sellin, N. M. Strickland, T. Böttger, J. L. Carlsten, and R. L. Cone, "Laser stabilization at 1536 nm using regenerative spectral hole burning", Phys. Rev. B **63**, 155111 (2001).

[5] M. Colice, F. Schlottau, K. Wagner, R. K. Mohan, W. R. Babbitt, I. Lorgere, and J.-L. L. Gouet, "RF spectrum analysis in spectral hole burning media", in Optical information systems ii, Vol. 5557, edited by B. Javidi and D. Psaltis (International Society for Optics and Photonics, 2004), pp. 132–139.

[6] P. Berger, Y. Attal, M. Schwarz, S. Molin, A. Louchet-Chauvet, T. Chanelière, J.-L. L. Gouët, D. Dolfi, and L. Morvan, "Rf spectrum analyzer for pulsed signals: ultra-wide instantaneous bandwidth, high sensitivity, and high time-resolution", J. Lightwave Technol. **34**, 4658–4663 (2016).

[7] A. Kinos et al., *Roadmap for rare-earth quantum computing*, 2021.

[8] M. F. Askarani et al., "Long-lived solid-state optical memory for high-rate quantum repeaters", Phys. Rev. Lett. **127**, 220502 (2021).

[9] C. W. Thiel, N. Sinclair, W. Tittel, and R. L. Cone, "Optical decoherence studies of Tm^{3+} : $Y_3Ga_5O_{12}$", Phys. Rev. B **90**, 214301 (2014).

[10] C. W. Thiel, N. Sinclair, W. Tittel, and R. L. Cone, "Tm^{3+} : $Y_3Ga_5O_{12}$ Materials for spectrally multiplexed quantum memories", Phys. Rev. Lett. **113**, 160501 (2014).

[11] R. MacFarlane, C. Yannoni, and R. Shelby, "Optical line narrowing by nuclear spin decoupling in pr3+: laf3", Optics Communications **32**, 101–104 (1980).

[12] C. Thiel, T. Böttger, and R. Cone, "Rare-earth-doped materials for applications in quantum information storage and signal processing", Journal of Luminescence **131**, Selected papers from DPC'10, 353–361 (2011).

[13] W. Moerner et al., *Persistent spectral hole-burning: science and applications*, Topics in Current Physics (Springer Berlin Heidelberg, 1988).

[14] L. Allen and J. Eberly, *Optical resonance and two-level atoms*, Dover Books on Physics (Dover Publications, 2012).

[15] M. Bonarota, J. Ruggiero, J. .-. L. Gouët, and T. Chanelière, "Efficiency optimization for atomic frequency comb storage", Phys. Rev. A **81**, 033803 (2010).

[16] P. Jobez, N. Timoney, C. Laplane, J. Etesse, A. Ferrier, P. Goldner, N. Gisin, and M. Afzelius, "Towards highly multimode optical quantum memory for quantum repeaters", Phys. Rev. A **93**, 032327 (2016).

[17] L. Rippe, M. Nilsson, S. Kröll, R. Klieber, and D. Suter, "Experimental demonstration of efficient and selective population transfer and qubit distillation in a rare-earth-metal-ion-doped crystal", Phys. Rev. A **71**, 062328 (2005).

[18] L. Veissier, C. W. Thiel, T. Lutz, P. E. Barclay, W. Tittel, and R. L. Cone, "Quadratic zeeman effect and spin-lattice relaxation of Tm^{3+}:yag at high magnetic fields", Phys. Rev. B **94**, 205133 (2016).

[19] T. Böttger, C. W. Thiel, Y. Sun, and R. L. Cone, "Optical decoherence and spectral diffusion at 1.5 μm in $Er^{3+}:Y_2SiO_5$ versus magnetic field, temperature, and Er^{3+} concentration", Phys. Rev. B **73**, 075101 (2006).

[20] C. W. Thiel, N. Sinclair, W. Tittel, and R. L. Cone, "Optical decoherence studies of $Tm^{3+}:Y_3Ga_5O_{12}$", Phys. Rev. B **90**, 214301 (2014).

[21] E. D. Black, "An introduction to pound–drever–hall laser frequency stabilization", American Journal of Physics **69**, 79–87 (2001).

[22] J. H. Davidson, *Custom python scripts available on git hub*, 2021.

[23] J. F. Dillon and L. R. Walker, "Ferrimagnetic resonance in rare-earth doped yttrium iron garnet. ii. terbium substitution", Phys. Rev. **124**, 1401–1413 (1961).

[24] G. Menzer, "Xx. die kristallstruktur der granate", Zeitschrift für Kristallographie - Crystalline Materials **69**, 300–396 (01 Dec. 1929).

[25] Y. C. Sun, "Rare earth materiais in optical storage and data processing applications", in *Spectroscopic properties of rare earths in optical materials*, edited by R. Hull, J. Parisi, R. M. Osgood, H. Warlimont, G. Liu, and B. Jacquier (Springer Berlin Heidelberg, Berlin, Heidelberg, 2005), pp. 379–429.

[26] J. H. Davidson et al., "Measurement of the thulium ion spin hamiltonian in an yttrium gallium garnet host crystal", Phys. Rev. B **104**, 134103 (2021).

[27] R. Lauro, T. Chanelière, and J. L. L. Gouët, "Slow light using spectral hole burning in a tm3+: yag crystal", arXiv preprint arXiv:0902.2657 (2009).

[28] A. Louchet, J. S. Habib, V. Crozatier, I. Lorgeré, F. Goldfarb, F. Bretenaker, J.-L. L. Gouët, O. Guillot-Noël, and P. Goldner, "Branching ratio measurement of a Λ system in Tm^{3+}:YAG under a magnetic field", Phys. Rev. B **75**, 035131 (2007).

[29] Y. Sun, G. M. Wang, R. L. Cone, R. W. Equall, and M. J. M. Leask, "Symmetry considerations regarding light propagation and light polarization for coherent interactions with ions in crystals", Phys. Rev. B **62**, 15443–15451 (2000).

[30] C. W. Thiel, R. M. Macfarlane, Y. Sun, T. Böttger, N. Sinclair, W. Tittel, and R. L. Cone, "Measuring and analyzing excitation-induced decoherence in rare-earth-doped optical materials", Laser Physics **24**, 106002 (2014).

[31] H. Linget, T. Chanelière, J.-L. Le Gouët, P. Berger, L. Morvan, and A. Louchet-Chauvet, "Interlaced spin grating for optical wave filtering", Phys. Rev. A **91**, 023804 (2015).

[32] M. S. Silver, R. I. Joseph, and D. I. Hoult, "Selective spin inversion in nuclear magnetic resonance and coherent optics through an exact solution of the bloch-riccati equation", Phys. Rev. A **31**, 2753–2755 (1985).

[33] F. T. Hioe, "Solution of bloch equations involving amplitude and frequency modulations", Phys. Rev. A **30**, 2100–2103 (1984).

[34] M. Tian, T. Chang, K. D. Merkel, and W. Randall, "Reconfiguration of spectral absorption features using a frequency-chirped laser pulse", Appl. Opt. **50**, 6548–6554 (2011).

[35] I. Roos and K. Mølmer, "Quantum computing with an inhomogeneously broadened ensemble of ions: suppression of errors from detuning variations by specially adapted pulses and coherent population trapping", Phys. Rev. A **69**, 022321 (2004).

[36] L. Johnson and C. Cox, "Serrodyne optical frequency translation with high sideband suppression", Journal of Lightwave Technology **6**, 109–112 (1988).

[37] E. Saglamyurek, N. Sinclair, J. A. Slater, K. Heshami, D. Oblak, and W. Tittel, "An integrated processor for photonic quantum states using a broadband light–matter interface", **16**, 065019 (2014).

[38] C. Thiel, N. Sinclair, W. Tittel, and R. Cone, "Tm3+ : y3ga5o12 materials for spectrally multiplexed quantum memories", Physical review letters **113**, 160501 (2014).

[39] C. W. Thiel, R. M. Macfarlane, Y. Sun, T. Böttger, N. Sinclair, W. Tittel, and R. L. Cone, "Measuring and analyzing excitation-induced decoherence in rare-earth-doped optical materials", Laser Physics **24**, 106002 (2014).

[40] Y. Sun, C. W. Thiel, and R. L. Cone, "Optical decoherence and energy level structure of 0.1% tm^{3+}:$linbo_3$", Phys. Rev. B **85**, 165106 (2012).

[41] J. R. Klauder and P. W. Anderson, "Spectral diffusion decay in spin resonance experiments", Phys. Rev. **125**, 912–932 (1962).

[42] W. B. Mims, "Phase memory in electron spin echoes, lattice relaxation effects in $cawo_4$: er, ce, mn", Phys. Rev. **168**, 370–389 (1968).

[43] L. Veissier, C. W. Thiel, T. Lutz, P. E. Barclay, W. Tittel, and R. L. Cone, "Quadratic zeeman effect and spin-lattice relaxation of Tm^{3+}:yag at high magnetic fields", Phys. Rev. B **94**, 205133 (2016).

[44] R. M. Macfarlane, "Photon-echo measurements on the trivalent thulium ion", Opt. Lett. **18**, 1958–1960 (1993).

[45] T. Lutz, L. Veissier, C. W. Thiel, R. L. Cone, P. E. Barclay, and W. Tittel, "Modification of phonon processes in nanostructured rare-earth-ion-doped crystals", Phys. Rev. A **94**, 013801 (2016).

[46] F. Euler, J. Bruce, and A. F. C. R. L. (U.S.), *Oxygen coordinates of compounds with garnet structure*, Physical sciences research papers (Air Force Cambridge Research Laboratories, Office of Aerospace Research, United States Air Force, 1966).

[47] T. Böttger, "Laser frequency stabilization to spectral hole burning frequency references in erbium-doped crystals: material and device optimization", PhD thesis (Apr. 2002).

[48] K. Persson, *Materials data on y3ga5o12 (sg:230) by materials project*, An optional note, July 2014.

[49] J. H. Van Vleck, "The dipolar broadening of magnetic resonance lines in crystals", Physical Review **74**, 1168 (1948).

5

A LONG-LIVED SOLID-STATE OPTICAL MEMORY FOR HIGH-RATE QUANTUM REPEATERS

Mohsen Falamarzi Askarani*, Antariksha Das*, Jacob H. Davidson, Gustavo C. Amaral, Neil Sinclair, Joshua A. Slater, Sara Marzban, Charles W. Thiel, Rufus L. Cone, Daniel Oblak, and Wolfgang Tittel

We argue that long optical storage times are required to establish entanglement at high rates over large distances using memory-based quantum repeaters. Triggered by this conclusion, we investigate the $^3H_6 \leftrightarrow {}^3H_4$ *transition at 795.325 nm of Tm:*$Y_3Ga_5O_{12}$ *(Tm:YGG). Most importantly, we show that the optical coherence time can reach 1.1 ms, and, using laser pulses, we demonstrate optical storage based on the atomic frequency comb protocol up to 100 µs as well as a memory decay time* T_M *of 13.1 µs. Possibilities of how to narrow the gap between the measured value of* T_M *and its maximum of 275 µs are discussed. In addition, we demonstrate quantum state storage using members of non-classical photon pairs. Our results show the potential of Tm:YGG for creating quantum memories with long optical storage times, and open the path to building extended quantum networks.*

Parts of this chapter is published in Physical Review Letters **127**, 220502 [1]

*These authors contributed equally to this work.

5.1. PREAMBLE

The results of this paper are very promising for extending the storage time of Tm:YGG memories to a value that enables elementary quantum repeater links over many kilometers. To push further, we also demonstrate many of the principles that are required for building a frequency multiplexed quantum repeater. However, the storage efficiency is poor compared to that in the previous chapter. Tying together the improvements of these first two chapters is an ongoing theme that I look to build upon throughout this thesis.

5.2. INTRODUCTION

THE future quantum internet [2, 3] will enable one to share entanglement and hence quantum information over large distances – ultimately between any two points on earth. To overcome attenuation in optical fibers, quantum repeaters are needed [4–8], many of which require quantum memories for light [9]. Such memories allow storing qubits, encoded into photons that have traveled over long distances until feed-forward information becomes available. This information specifies which optical mode—including spectral, spatial, and temporal modes—a qubit should occupy once it has been re-emitted from the memory. Note that the required mode assignment (or mode mapping operation) can happen in a memory-internal manner, e.g. by controlling when a photon is re-emitted (*aka* read-out on demand) [5, 10–12], or externally, e.g. by directing the emitted photon to a specific spatial mode [13] or by shifting its spectrum [7].

To maximize the entanglement distribution rate of a quantum repeater, qubits must be added continuously to the memory – not only once a previously stored qubit has been re-emitted but also while it is still being stored. Such multiplexed storage implies (a) the use of large ensembles of absorbers that enable bi-partite entanglement with many photonic qubits; and (b) that any memory-specific control operation, triggered by the absorption of a newly arriving qubit, must neither affect re-emission nor the possibility for mode mapping of a previously absorbed qubit. Stated differently, any control operation required after absorption of a qubit or a train of qubits must not introduce deadtime that prevents the memory from accepting additional qubits. This would cause a reduction of the memory's time-bandwidth product [14, 15] and, when used as an element of a quantum repeater, a reduction in the entanglement distribution rate (see the supplemental material for an example).

Unfortunately, the latter requirement of qubit independence (b) can be at odds with a high repetition rate. As we show below, one example is that of temporal multiplexing and read-out on demand in the so-called atomic frequency comb (AFC) quantum memory protocol, which requires one to temporarily map qubit states between optical and spin coherence [16]. This leads us to conclude that it is important to optimize the *optical storage time*, i.e. the time during which qubits are stored as optical coherence, which can be excited using visible or near-infrared light. It is important to realize that this conclusion also holds in the case of purely optical storage (no spin mapping), regardless of the degree of freedom used for multiplexing. Triggered by this finding, we investigate thulium-doped yttrium gallium garnet (Tm^{3+}:$Y_3Ga_5O_{12}$ or Tm:YGG) – a rare-earth-ion doped crystal (REIC) whose promising spectroscopic properties have been

demonstrated previously [17, 18], but whose potential for storing photonic qubits has not yet been established. Here we show that its optical coherence time T_2 can reach 1.1 ms, which is one of the longest times reported for any REIC [19, 20]. Motivated by this promising result, we investigate Tm:YGG for AFC-based memory, and demonstrate optical storage of laser pulses up to 100 μs. This is comparable with recent results obtained using Yb:Y_2SiO_5 [21] and Eu:Y_2SiO_5 [22], and exceeds all other reported results of storage of light in optical coherence with any REIC by at least a factor of 10. However, we also find that the memory decay time T_m of around 13 μs is 20 times smaller than the T_2-imposed maximum of 275 μs. Before addressing the reasons for this large gap, we confirm the possibility for spectrally multiplexed storage and feed-forward-based spectral mode mapping [7], which allows using memory materials—including Tm-doped crystals—whose atomic level structure lacks the spin states required for memory-internal temporal mode mapping. Furthermore, we also show that quantum correlations between members of photon pairs persist throughout storage, i.e. that our memory can operate in the quantum regime. We conclude by mentioning reasons for the currently small memory efficiency, leaving more details to the supplemental material.

5.3. THE NEED FOR LONG OPTICAL STORAGE

To support our claim that qubit independence can be at odds with a high repetition rate, let us discuss the example of temporal mode mapping using the AFC spin-wave memory in REICs [12]. As depicted in Fig. 5.1a, a pair of optical control pulses (π-pulses that resonantly couple the excited state $|e\rangle$ with a ground state $|s\rangle$) allows one to reversibly map optical coherence onto a spin transition. In this case, the timing of the second control pulse determines when the photons will be re-emitted from the memory, allowing for readout on demand.

Let us now assume that a first train, R1, of temporally multiplexed qubits has already been absorbed by the memory, that the first control pulse has been applied, and that a second train, R2, of qubits has just been added to the memory (Figs. 5.1b-d). At this point, R1 is stored in terms of spin coherence, and R2 in terms of optical coherence. Unfortunately, the subsequent control pulse, applied to the memory with the goal to map R2 onto spin coherence, simultaneously maps R1 back onto optical coherence. This causes the re-emission of these qubits at a time that is determined by the need to transfer the second train, rather than by feed-forward information that specifies what to do with the first.

Fortunately, this problem can be avoided by storing only one train at a time. But in order to maximize the repetition rate of the repeater (or to minimize the memory's deadtime), this block, and hence the time during which qubits are stored in optical coherence, should be as long as possible – ideally as long as the total storage time. At the same time, long optical storage times allow for maximizing the elementary link length in quantum repeater architectures that do not employ mapping between optical and spin coherence. In turn, this leads to higher entanglement distribution rates as it reduces the number of (currently inefficient) Bell-state measurements that are required to connect neighboring links [7].

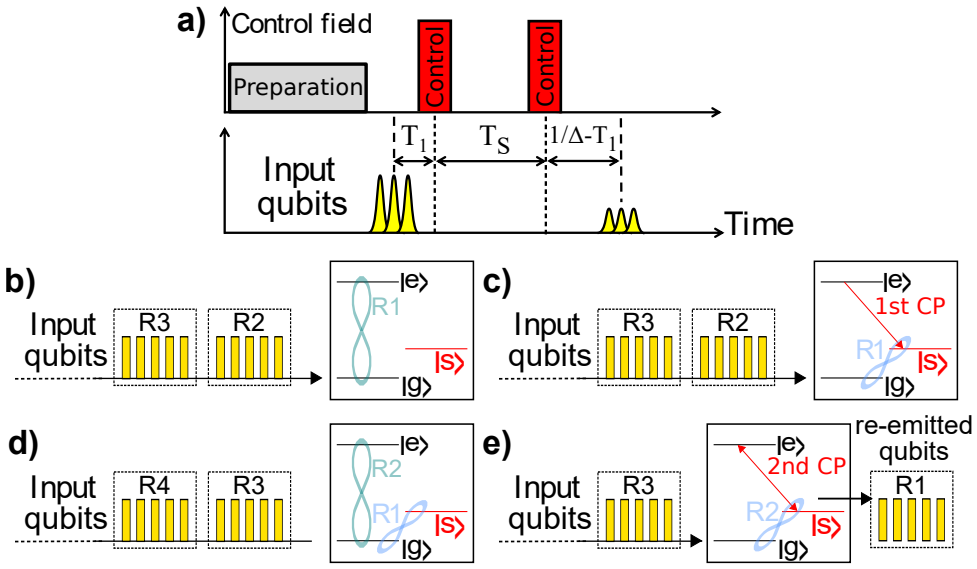

Figure 5.1: **Recall on demand using the AFC spin-wave storage protocol. a.** Pulse sequence. **b - e.** Memory input and output, as well as atomic coherence (indicated by light blue and green figures of eight) for different moments during storage (see text for details). Trains of qubits are labeled R1-R4; CP: Control Pulse. A three-level lambda system is formed by spin states $|g\rangle$ and $|s\rangle$, and by excited state $|e\rangle$.

5.4. TM:YGG AND EXPERIMENTAL SETUP

Due to their unique spectroscopic properties [23], REICs have been broadly explored over the last two decades for quantum technology [24, 25], e.g. as ensemble-based quantum memory for light [9, 26, 27] or for quantum processing [28, 29]. But while significant effort has been spent to increase storage times in spin coherence [30–33]), much less work has been devoted to advancing and better understanding the limitations of storage in optical coherence. To address this shortcoming, we use a 25-mm long, 1% Tm:YGG crystal, mounted inside an adiabatic demagnetization refrigerator cooled to ~500 mK. YGG forms a cubic lattice in which Tm^{3+} replaces Y^{3+} in six crystallographically equivalent sites of local D_2 point group symmetry [34]. An ideal Tm:YGG crystal is optically isotropic. Magnetic fields up to 2 T can be applied along the crystal < 111 > axis, splitting all electronic levels through the enhanced Zeeman interaction into two hyperfine sub-levels [18, 35]. Fig. 5.2 (Inset) depicts a simplified level structure.

We use a tunable continuous-wave diode laser at 795.325 nm wavelength to address the $^3H_6 \leftrightarrow {}^3H_4$ zero-phonon line. Due to the use of a non-polarization-maintaining fiber, the polarization state at the input of the crystal is unknown. Furthermore, it evolves inside the crystal due to birefringence stemming from imperfect crystal growth [17]. The laser is frequency-locked to a high finesse cavity using the Pound-Drever-Hall method, resulting in an instability over ~100 μs below 20 kHz. To intensity- and frequency-modulate the light, we use a single-pass acousto-optic modulator (AOM) (driven by an RF signal generator) and a phase modulator (PM) (driven by an arbitrary waveform generator). After passing through the crystal's < 110 > direction, the light is directed to a photo-

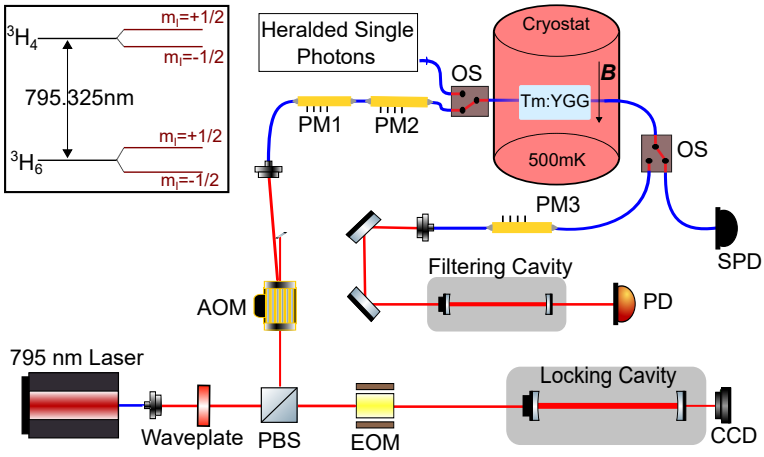

Figure 5.2: **Experimental setup**. AOM: acousto-optic modulator; PM: phase modulator; OS: optical switch; EOM: electro-optic modulator; PD: Classical photodetector; SPD: Single photon detector; CCD: charge-coupled device camera; ***B***: Magnetic field. Inset: Simplified energy level diagram of Tm:YGG showing the $^3H_6 \leftrightarrow {}^3H_4$ zero-phonon line.

detector. This setup is used for AFC creation (see also [36]), initial memory characterization, and storage of optical pulses in a single spectral mode. For frequency-multiplexed storage and feed-forward recall, additional phase modulators are used to add frequency side-bands to the laser light, each of which creates a memory in a different spectral segment, and to frequency shift the light after re-emission so that only the desired spectral mode passes through an optical filter cavity [7]. In addition to laser pulse, we can also send heralded single photons into the memory, see Fig. 5.2.

5.5. MEASUREMENT AND RESULTS

First, as a key property that determines the maximum optical storage time, we characterized the optical coherence time T_2 as a function of magnetic field using 2-pulse photon echoes [37]. As an important difference compared to our previous studies [17, 18], the temperature was lowered from 1.2 K to 500 mK. As shown in Figs. 5.3a,b and predicted earlier [17], this resulted in a very significant improvement of the coherence time from 490 μs to around 1.1 ms – one of the longest reported optical coherence times for any rare-earth crystal and approaching the limit of 2.6 ms imposed by the $^3H_4$ population lifetime [18]).

Next, we investigated the possibility of optical data storage, both using laser pulses as well as quantum states of light. Towards this end, we employed the two-level atomic frequency comb protocol [16]. An AFC is characterized by an absorption profile composed of evenly-spaced teeth in the frequency domain, which can be created using frequency-selective optical pumping of the population from the troughs of the AFC to other atomic levels. Note that Tm:YGG is well suited for this task due to long-lived hyperfine levels within the electronic ground state manifold [18]. Absorption of a photon with wavenumber k by an AFC results in the creation of a collective atomic excitation described by

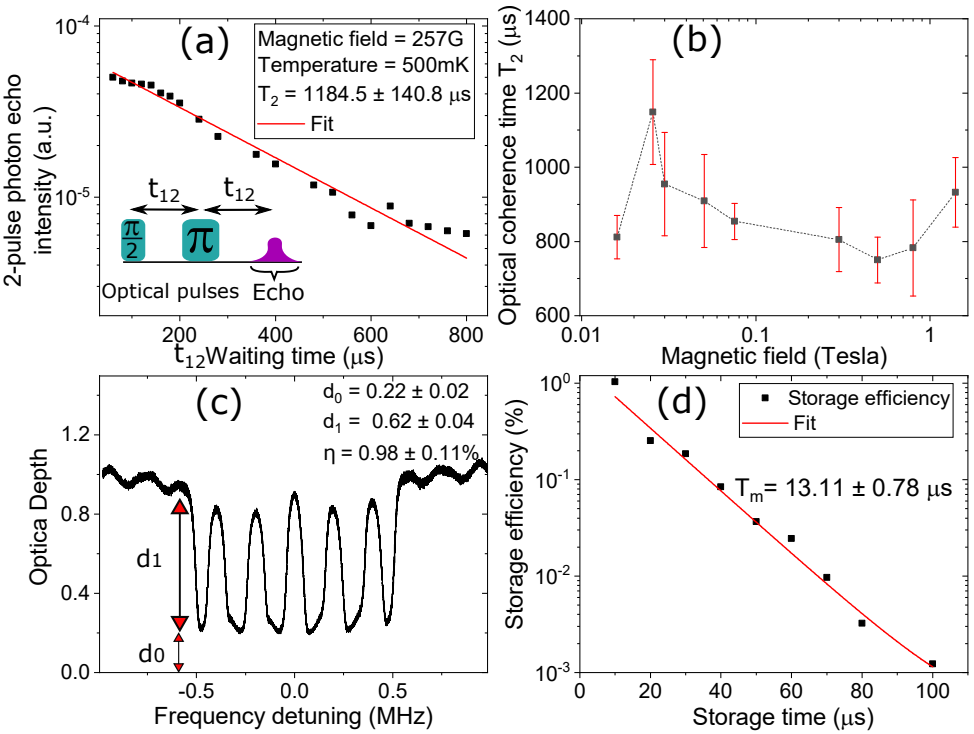

Figure 5.3: **Optical coherence, and optical data storage in a single spectral mode. a.** Exponential decay of the two-pulse photon echo signal as a function of the delay between the two optical pulses. **b.** Optical coherence time T_2 as a function of magnetic field. The dashed line guides the eye. **c.** AFC of 1 MHz bandwidth tailored for 5 μs storage time. The calculated efficiency, η, is approximately 1%. **d.** Measured memory efficiency as a function of storage time using AFCs with finesse 2. In all measurements T~500 mk. The error bars in (a) and (d) are smaller than the data points.

$|\psi\rangle_A = N^{-1/2}\sum_{j=1}^{N} c_j e^{i2\pi\delta_j t} e^{-ikz_j}|e_j\rangle$. Here, N is the number of ions in the AFC, $|e_j\rangle$ a state in which only ion j is excited, δ_j the detuning of this ion's transition with respect to the input photon's carrier frequency, and z_j and c_j its position and excitation probability amplitude, respectively. After initial dephasing, the coherence rephases, resulting in re-emission of the photon after a time τ that is determined by the inverse AFC tooth spacing Δ, where $\tau = 1/\Delta$. See [16, 22] for more details. An example of an Tm:YGG AFC is depicted in Fig. 5.3c.

5.5.1. LONG-LIVED STORAGE OF LASER PULSES

Given the remarkable optical coherence time, it is important to assess how the memory efficiency evolves with storage time. To this end, we used 1 μs-long laser pulses (note that the use of true single photons would not change the results), and created AFCs with finesse F—the ratio between AFC peak spacing Δ and peak width δ—of 2. See [7, 36] for more information. Tooth spacings varied between 100 kHz and 10 kHz, corresponding to storage times between 10 and 100 μs, respectively. The choice of F=2 maximizes the

storage efficiency (see section 2B in the supplemental material), which was limited due to the crystal's small optical depth of around 1. The AFC bandwidth for all storage times was 0.5 MHz except for 100 μs, where it was reduced to 0.2 MHz. Due to the need for highly resolved AFCs with narrow-linewidth teeth, their preparation took 1 s. This time was followed by a waiting time of 20 ms—approximately 15 times the radiative lifetime of the $^3H_4$ level—to avoid detecting spurious photons caused by spontaneous decay of ions excited during the AFC preparation. The magnetic field in all measurements was around 100 G, which maximizes the optical coherence time.

We detected re-emitted pulses after up to 100 μs and found that the memory storage efficiency decreases exponentially as a function of storage time with a decay constant T_m =13.1±0.8 μs (see Fig. 5.3d). This value is much smaller than the ultimate limit T_m^{max} imposed by T_2 of around 275 μs. Possible reasons are listed in the outlook and detailed in the supplemental material.

5.5.2. FREQUENCY-MULTIPLEXED STORAGE WITH FEED-FORWARD MODE MAPPING

To demonstrate spectral multiplexing, we prepared 11 AFCs with F=2, each of 1 MHz bandwidth and spaced by 10 MHz, over a total bandwidth of 100 MHz. Laser pulses of 1 μs duration were created in each spectral mode. They were stored and recalled after 5 μs (see Fig. 5.4a). Note that the individual modes were resolved by changing the resonance frequency of the filtering cavity (see Fig. 5.2). Assuming that five subsequent pulses—each of 1 μs duration—fit into the storage time, this results in a multimode capacity over spectral and temporal degrees of freedom of 55. Note that the storage time—significantly less than our maximum of 100 μs in this and all subsequent measurements—was limited by a trade-off between a more complex AFC tailoring procedure and memory efficiency. Otherwise, all parameters used to create the AFCs remained unchanged.

To implement feed-forward mode mapping, imposed by the use of a multiplexed memory in a quantum repeater, we furthermore demonstrated spectral shifting of the recalled laser pulses such that only the desired spectral mode was subsequently transmitted through a filter cavity with a fixed resonance frequency. Our approach, which is further explained in the supplemental material and in [7], is equivalent to the more well-known case of temporal multiplexing, in which one has to retrieve photons in specific temporal modes. Since the mode mapping in our case is performed in the frequency domain, the storage time of the memory is fixed; it corresponds to the round-trip time from the end of an elementary link to its center and back. The results of our proof-of-principle demonstration are depicted in Fig. 5.4b.

For these measurements, the internal storage efficiency (calculated by comparing the energies of input and re-emitted pulses and after considering coupling loss) was around 1.3%. Note that number of spectral channels can easily be increased with more laser power, allowing for paralleled AFC generation. Given the inhomogeneous broadening of the $^3H_6 \leftrightarrow {}^3H_4$ transition of 56 GHz, this could in principle yield thousands of spectral modes. Furthermore, increasing the storage time by an order of magnitude—still much less then T_m^{max}—would improve the multi-mode capacity by another factor of ten.

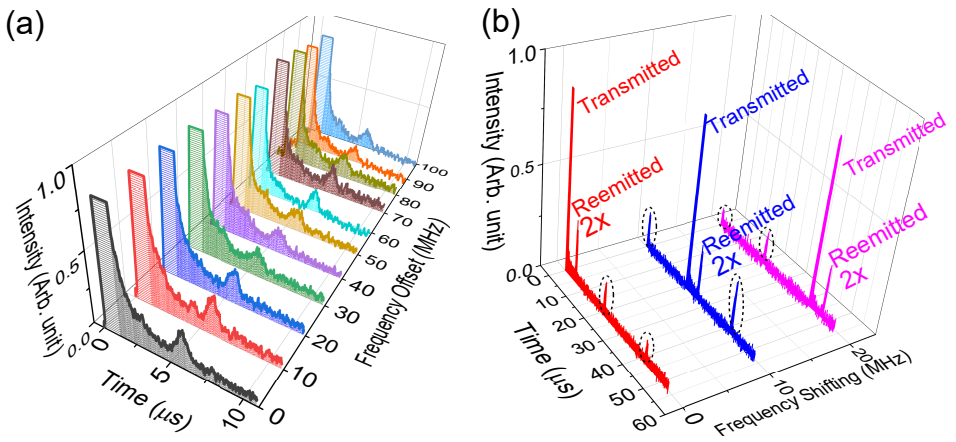

Figure 5.4: **Storage of data in multiple spectral modes. a.** Spectrally-multiplexed AFC quantum memory used to simultaneously store optical pulses in 11 spectral modes for 5 μs. **b.** Feed-forward mapping of spectral modes onto one with zero detuning. Laser pulses in three spectral modes were stored and re-emitted after 5 μs. Frequency shifting using phase modulator PM3 allowed mapping any desired mode onto one with zero detuning. Only this mode was transmitted through the filter cavity. The re-emitted pulses are magnified by a factor of 2, and crosstalk is indicated using dotted circles.

5

5.5.3. STORAGE OF HERALDED SINGLE PHOTONS

Finally, we verified that Tm:YGG, together with the two-level AFC protocol, is suitable for quantum state storage. As described in detail in [38], we created pairs of quantum-correlated photons at 795 and 1532 nm wavelength by means of spontaneous parametric down-conversion of strong laser pulses in a periodically-poled $LiNbO_3$ crystal. The detection of a 1532 nm photon using a superconducting nanowire single-photon detector heralded the presence of a 795 nm photon, which was directed into, stored in, and released after 43 ns from the Tm:YGG memory. Note that the memory creation procedure remained unchanged except that the AFC bandwidth was increased to 4 GHz to better match the photon bandwidth, and that the magnetic field was increased to 3 kG to match the difference in the ground and excited state level splitting with the spacing between a trough and the neighboring tooth in the AFC [39]. The latter also increased the persistence of the AFC, allowing us to repeat the preparation sequence only every 10 s. Together with the preparation time of 1 s, this resulted in a memory availability of around 90%. The photons were then detected using a single-photon detector based on a silicon avalanche photodiode. The system efficiency, assessed by comparing photon detection rates with and without memory was 0.05%. Taking 15% fiber coupling into account, this yields an internal storage efficiency of 0.35%.

To verify that the non-classical correlations with the 1532 nm photons persist throughout the storage process, we measured the 2nd order cross-correlation coefficient $g^{(2)}_{12}(t)$ between the two photons of a pair using time-resolved coincidence detection [36]. Before storage, we found $g^{(2)}_{12}(0\,ns)$= 18±0.02 and, importantly, after 43 ns storage $g^{(2)}_{12}(43\,ns)$= 4.58±0.46 (this value is reduced due to excess loss combined with detector dark counts). See the supplemental material. Both values surpass the classical upper bound of 2, con-

firming the quantum nature of the photon source as well as the memory.

5.6. DISCUSSION AND CONCLUSION

Our investigations have resulted in an optical coherence time T_2 up to 1.1 ms and optical storage times up to 100 μs. However, they also revealed a memory decay time of 13.1 μs – significantly smaller than the limit imposed by T_2, and in general a small recall efficiency. To increase the memory performance to a level that allows its use in a quantum network, several improvements, most, if not all of which are of technical nature, are required. As we describe in more detail in the supplemental material, this includes using a frequency-stabilized laser with narrower linewidth, a cryostat with reduced vibrations, a more stable magnetic field as well as finding parameters (propagation direction and polarization of the light, and external magnetic field) under which spectral diffusion due to ion-ion interactions is reduced and the $^3H_6 \leftrightarrow {}^3H_4$ transition becomes a so-called clock transition [35]. Furthermore, to counter the effects of limited optical depth, the light-atom interaction has to be enhanced using an impedance-matched cavity [31, 40–43]. This also removes the problem of re-absorption of photons that are emitted in forward direction. Furthermore, we can improve the optical pumping by changing the currently sequential excitation of narrow spectral intervals within the inhomogeneously broadened Tm transition by complex hyperbolic secant pulses [22, 44]. This will lead to better confined teeth with a more squarish spectral profile, and hence to a reduced background within the troughs in between these teeth. At the same time, it will also allow creating AFCs with higher finesse, resulting in reduced decoherence during photon storage [22, 45, 46].

Finally, note that despite the currently small multiplexing capability—in particular, compared to the 1060 temporal modes in [47]—our demonstration shows the advantage of using atomic ensembles over single absorbers where it is limited to one. Note as well that coupling of a single spin, e.g. a diamond nitrogen-vacancy center, to neighboring nuclear spins does not solve this issue due to the limited number of interacting neighbors—e.g. 27 in [48]—and the small coupling strength.

We anticipate that further improvements of our work will lead to long-lived, efficient, and multi-mode optical quantum memories that enable the efficient distribution of entanglement across extended quantum networks.

5.7. SUPPLEMENTARY MATERIAL

5.7.1. MEMORY DEADTIME AND REPEATER-BASED ENTANGLEMENT DISTRIBUTION RATE

To show the impact of a memory with dead-time on repeater performance, more precisely the impact on the entanglement distribution rate, we focus on the quantum repeater protocol described and analyzed in [7, 49, 50]. See Fig.S 5.5 for an illustration.

In this approach, a fixed number of qubits in n different spectral modes is created at each node and sent towards the central location of the elementary link that connects to the neighboring node. Each qubit is entangled with a second qubit, also in one of n different spectral modes, whose states are mapped into a quantum memory where they are stored as *optical coherence* (not spin coherence). At the central location, a Bell-state

measurement projects the transmitted qubits pairwise in a spectrally-resolved manner onto a maximally entangled state. This entangles qubits in the two memories–one on either end of the elementary link. After sending information about the channel(s) in which entanglement has been generated back to the two nodes, each node recalls all qubits from its memory and selects, out of the block of n, one (now entangled) qubit whose mode is subsequently shifted to allow for a Bell-state measurement with a qubit from the neighboring elementary link. Given the multi-mode capacity of the assumed memory as well as no dead-time, the next set of qubits can be created by the source and stored in the memory as soon as the creation of the previous set has been terminated.

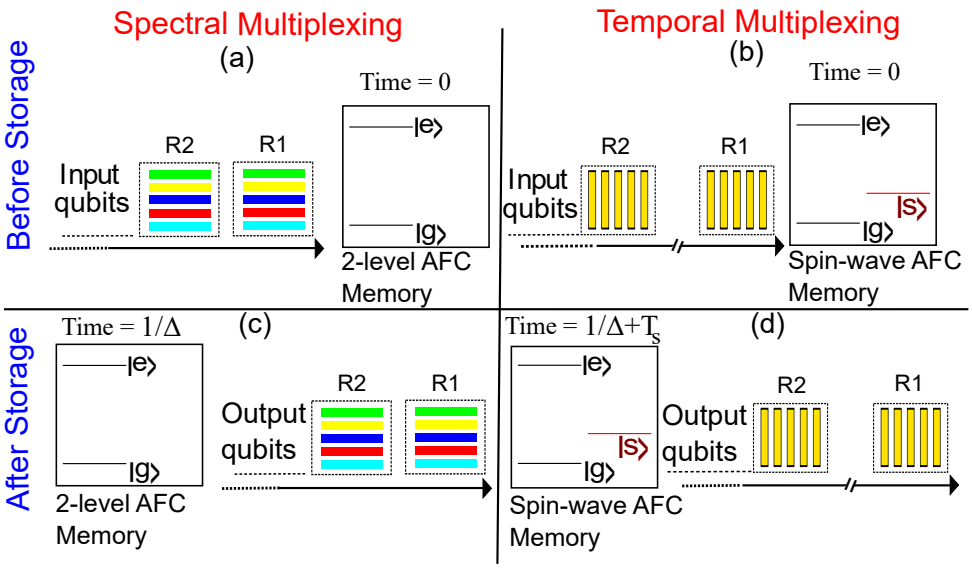

Figure 5.5: Illustration of storage sequence for spectral multiplexing (left-hand column) and temporal multiplexing (right-hand column). (a) and (b) represent the moment before storage, and (c) and (d) after storage. Two subsequent trains (or blocks) of qubits are labeled R1, R2. In (a) and (c), different colors represent different spectral modes. The three-level lambda system needed for read-out on demand is formed by spin states $|g\rangle$ and $|s\rangle$, and by excited state $|e\rangle$. Note how the dead-time of the spin-wave memory imposes a delay time between qubit trains R1 and R2 (in b and d).

Generalizing this approach to temporal modes, we arrive at the following: First, n qubits belonging to n entangled pairs in n subsequent temporal modes are created and sent to the central node of the elementary link. The other qubits of the n pairs are stored one after the other in optical coherence, and once the whole train of qubits has been mapped into the memory, it is transferred “en bloc" onto spin coherence. The outcome of a temporally-resolved Bell-state measurement at the central node then affects when the train of stored qubits is read out in each memory, ensuring that qubits from neighboring elementary links become indistinguishable in the temporal domain and can be subjected to another Bell-state measurement. Unfortunately, the use of spin-states for photon storage implies that the memory is dead after absorption (and spin transfer) of the n qubits. And hence, we face the problem that the entanglement distribution rate is reduced by the ratio between optical storage time and total storage time.

5.7.2. AFC EFFICIENCY, GENERATION, LIMITATIONS AND FUTURE IMPROVEMENT

We found a very promising optical coherence time and demonstrated storage times of up to 100 μs. However, both the storage efficiency at zero storage time as well as its scaling with storage time have to be improved to make Tm:YGG suitable for use in a future quantum repeater. This section deals with issues pertaining to this task.

AFC EFFICIENCY

As derived in detail in [16], the efficiency of an AFC-based memory depends on the optical depth of the teeth after pumping, d, the remaining optical depth within the troughs (which we refer to as the background), d_0, and the finesse, F. Furthermore, the tooth width, δ, affects how the efficiency scales with storage time. Assuming that δ is limited only by the homogeneous linewidth, γ_h, i.e. $\delta = 2\gamma_h$, and using $\gamma_h = 2/T_2$ [22], we find

$$\eta(\tau) = \left(\frac{d}{F}\right)^2 e^{-\frac{d}{F}} e^{-d_0} e^{-4\tau/T_2}. \tag{5.1}$$

For instance, for a finesse of 2, optical depths $d \approx 1$ and $d_0 \approx 0.4$, and T_2=1.1 ms, as in the storage of single photons, we calculate

$$\eta(\tau = 43ns) \approx 10.2\%. \tag{5.2}$$

AFC GENERATION – LEVEL SPLITTING AND TOOTH SEPARATION

Depending on the particular demonstration, we have created our atomic frequency combs using two different regimes: AFC *intrinsic pumping*, and AFC *extrinsic pumping*.

Intrinsic pumping – In the first case, optical pumping results in reduced optical depth in the troughs of the AFC, and an enhancement of the optical depth within the AFC teeth. This happens if the spacing between a trough and the neighboring tooth, Δ_{TT}, equals the splitting between a created hole and the neighboring anti-hole, which itself depends on the difference between the Zeeman splittings of the ground and excited level:

$$\Delta_{TT} = \Delta_{ge} = \Delta_g - \Delta_e = 1/(2\tau)$$

For the $^3H_6 \leftrightarrow {}^3H_4$ transition in Tm:YGG, $\Delta_g \approx 106$ MHz/T and $\Delta_e \approx 63$ MHz/T. Note the last equation sign, which expresses that the inverse storage time $1/\tau$ equals twice the splitting between a trough and the next tooth. Note as well that this case implies that $\Delta_{TT} \ll \Gamma_{AFC}$, where Γ_{AFC} is the AFC width.

The advantages of working in this regime are that the AFC bandwidth is only limited by the inhomogeneous broadening of the transition, e.g. 56 MHz in Tm:YGG; and that the optical depth of the teeth is increased through the pumping procedure. On the flip-side, the maximum finesse is F=2 [39], which limits the efficiency (see Eq. 5.1).

Given the possibility for GHz-wide AFCs, we have used the intrinsic pumping regime in our demonstration of single photon storage. In the case of Tm:YGG, the (enhanced) Zeeman interaction results in $\Delta_{ge} \approx 43$ MHz/T, and the level splitting can easily be matched with the AFC periodicity for storage times in excess of a few tens' of nanoseconds. However, as the storage time approaches microseconds, the requirement for a reduced level

splittings and hence a smaller magnetic field comes at the expense of lower Zeeman-level lifetime and less persistence [51], leaving less time to create and use the AFC.

Extrinsic pumping – As a second option, it is also possible to chose $\Delta_{ge} > \Gamma_{AFC} \gg \Delta_{TT}$ and to pump population outside the AFC.

This regime allows creating AFCs with higher finesse and hence reduced dephasing, albeit with generally small bandwidth. Also, the reduction of the optical depth within the troughs does not result in an increased depth of the teeth, which impacts the storage efficiency. But note that the use of an impedance-matched cavity allows reaching 100% efficiency despite the use of a storage material with limited optical depth (see below).

All AFCs used to store laser pulses were created using magnetic fields between 100 and 250 G. Even though this implies that we operated in the extrinsic pumping regime—the AFC width was at most 0.5 MHz—, we did not take advantage of the possibility to create AFCs with F>2 since this would have decreased the storage efficiency. Indeed, as described by Eq. 5.1, a larger finesse benefits the efficiency only in the case of sufficient optical depth d.

5

AFC LIMITATIONS AND FUTURE IMPROVEMENT

The measured efficiency for 43 ns-long single photon storage, 0.35%, is much smaller than the calculated value of 10.16 % in Eq. 5.2. This discrepancy is due to the existence of sources that cause tooth broadening beyond the value given by T_2. We come to the same conclusion when comparing the decay constant T_m=13.1 μs, extracted from re-emission of stored laser pulses (see Fig. 3d in the main text), with the T_2-limited value of 275 μs.

1. **Laser instability –** Even though our laser is frequency stabilized, its remaining linewidth of around 20 kHz starts impacting the storage efficiency at a few microseconds storage time. To demonstrate efficient storage during 100 μs, a laser linewidth of around 1 kHz is required – a challenge that have been mastered using existing technology [52, 53].

2. **Magnetic field instability –** We also found that magnetic field noise, caused by an unstable current supply, led to spectral diffusion and hence a further degradation of the AFC quality. For a magnetic field of around 200 G and 1 sec AFC creation time, this effect was visible for storage times above 40 μs. Interestingly, the use of larger magnetic fields—desired to improve the AFC persistence—made this problem worse, which we attribute to the quadratic Zeeman effect. The quadratic Zeeman effect was also observed in [54]. The solution to this problem is to use a more stable power supply or a permanent magnet.

3. **Cryostat vibrations –** Even though the 500 mK plate inside the cryostat on which the Tm:YGG crystal was mounted is mechanically isolated from the pulse-tube cooler, vibrations are expected to add additional decoherence. While its magnitude is currently unknown, similar observations have been reported in [21]. Future improvements include the use of a better cryostat, or better vibration isolation of the crystal inside [55].

4. **Spectral diffusion due to ion-ion coupling –** Spectral diffusion due to atom-atom interaction is also likely to play a role in the observed memory decay. For instance, a long-range quadrupole-quadrupole interaction between Tm ions may cause cross-relaxation. The presence of this mechanism has been conjectured in the case of Tm:YAG, which features the same site symmetry as Tm:YGG [56]. Decreasing the Tm doping concentration may help reducing the impact of this interaction.

   An additional cause for perturbation of Tm ions is spin flips in neighboring gallium ions or by two-level systems [17]. To reduce spectral diffusion caused by varying magnetic fields at the Tm sites, we have started investigating the possibility of choosing a magnetic field direction for which the 795 nm Tm transition becomes insensitive to first order to magnetic field fluctuations [35, 57–60].

5. **Imperfect spectral hole burning –** Our spectral tailoring sequence, which relied on sequential optical pumping in one narrow frequency interval after the other, has furthermore resulted in non-ideal tooth shapes, i.e. teeth with significant "wings" that cause rapid dephasing. It has been shown that the use of complex hyperbolic secant pulses allows creating teeth with a more squarish shape, improving the storage efficiency [22, 44].

6. **Insufficient optical depth –** A general issue is that the optical depth of our crystal is insufficient to absorb all photons – a necessary condition for high-efficiency storage. As the tooth width is reduced and the finesse increased, this problem becomes more and more important (see Eq. 5.1).

   First, we note that our AFCs are currently created using uncontrolled, optically and magnetically inequivalent subsets of Tm ions. Using a better—non-birefringent—crystal and selecting a specific polarization state at its input will allow optimizing photon-ion interaction [61], resulting in improved optical depth and memory efficiency.

   Second, and being a more important improvement, the problem of insufficient optical depth can be removed by embedding the rare-earth crystal inside an impedance matched cavity. This has been shown theoretically and in experiment [31, 40–43]. As a first step towards this goal, we have tailored an AFC for 30 μs storage time with F = 4, see Fig.S 5.6. Using the measured values $d_0 \approx 0.005$ and $d \approx 0.03$, we predict an internal efficiency of 18%. This would enable a proof-of-principle demonstration of an elementary quantum repeater link. Naturally, the creation of AFCs with less background will result in a further increase of the efficiency. See [41] for an example reaching 56%.

7. **AFC background –** Remaining optical depth in the troughs of our AFCs resulted in irreversible absorption and hence photon loss. This was due to insufficient long optical pumping, insufficient laser power during pumping, or a combination thereof. To remove this problem, several options exist. First, assuming that we can reduce the magnetic field fluctuations mentioned above, we can operate at a larger magnetic field, thereby increasing the persistence of the AFCs and in turn the time for optical pumping. Second, as has been shown in [46, 62], it is possible to rapidly

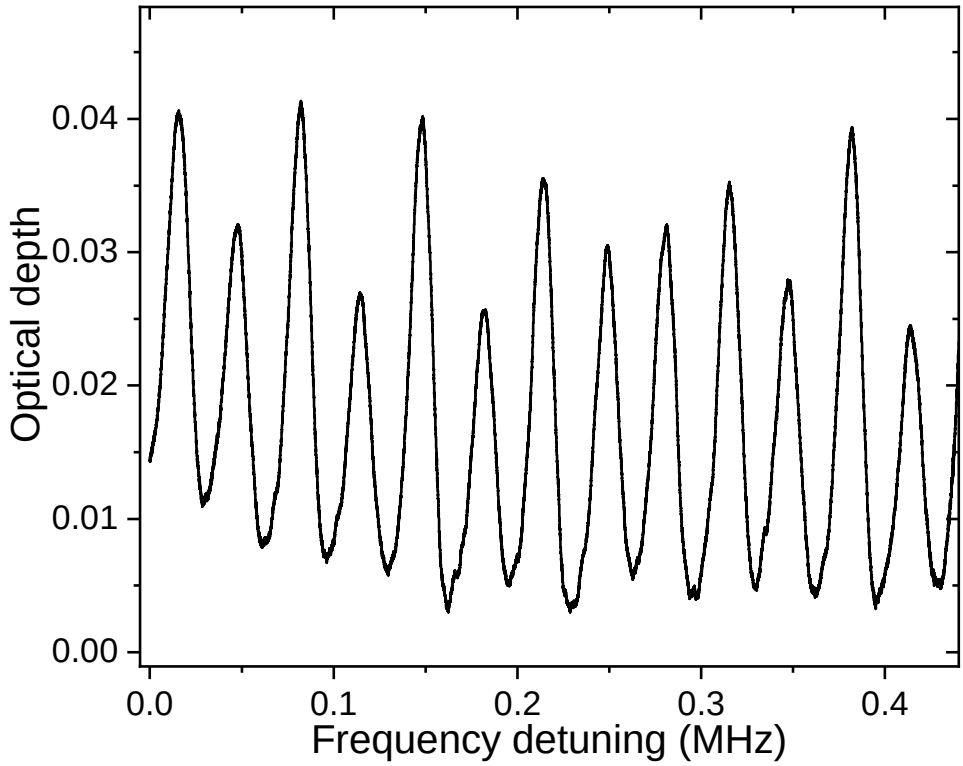

Figure 5.6: A 0.5 MHz AFC for 30 μs storage time with finesse 4

remove atomic population over a large spectral window using intense laser pulses, and then pump population in narrow spectral intervals back.

5.7.3. FEED-FORWARD MODE MAPPING

PROOF-OF-PRINCIPLE DEMONSTRATION

To demonstrate the possibility for feed-forward mapping between different spectral modes, we tailored, with the help of PM2, three AFCs spaced by 10 MHz in which spectrally matched optical pulses were stored. Pulses in different spectral modes were separated by 20 μs in order to make them distinguishable in time – a necessary feature for analysis since the filter cavity after the memory erased all spectral distinguishability.

First, we set the resonance frequency of the filtering cavity such that it allowed transmission of the spectral mode at zero frequency detuning– both for the light that was directly transmitted through the AFC as well as the stored and re-emitted pulse. The measured signal is depicted in Fig. 4b in the main text in red. At the same time, the cavity largely suppressed the pulses at 10 and 20 MHz detuning. However, because the cavity linewidth of 7.5 MHz is comparable with the spectral mode spacing of 10 MHz, small fractions of the neighboring modes leaked through. This crosstalk is visible in the peaks in the red-colored signal trace centered at 20 and 40 μs.

Next, we drove PM3, positioned in-between the memory and the filter cavity, using a 10 MHz serrodyne signal that shifted all pulses emitted by the memory by -10 MHz. Consequently, the signal encoded originally at +10 MHz detuning, depicted in Fig. 4b (main text) in blue, became resonant with the cavity, resulting in its transmission through the cavity and the detection of a large peak at 20 μs followed by a smaller peak—the recalled pulse—5 μs later. As before, some leakage of signals in neighboring modes lead to peaks at 0 and 40 μs.

Finally, the same experiment was repeated with a serrodyne shift of -20 MHz. The result is depicted by the magenta-colored signal trace in Fig. 4b in the main text.

EFFICIENCY CONSIDERATIONS

As described above, feed-forward spectral mode mapping requires frequency shifting and spectral filtering. Below we describe several ways to realize shifting. Note that none is fundamentally limited in its efficiency. The same holds for the transmission through a filter cavity for which values of around 97%–only limited by spatial mode-matching—have been reported (see, e.g.,[63]).

To shift the spectra of the photons emitted from a quantum memory, first, it is possible to use an electro-optic modulator (e.g. a $LiNbO_3$ phase modulator) driven by a linearly rising voltage or a sawtooth function (then referred-to as serrodyne modulation [64, 65]). These methods are employed in the present work and in [7]. Frequency shifts of tens' of GHz can be achieved using commercially available devices, and we have demonstrated internal shifting efficiencies in excess of 90% over such bandwidth (e.g. in [66]). The device efficiency is furthermore affected by lossy coupling into and out of the modulator. In the present demonstration with commercial devices, we have achieved a total shifting efficiency of 0.45 (internal efficiency of 0.9, coupling efficiency 0.5). However, better mode matching between input/output fiber and waveguide of the modulator may make it possible to increase this value by a factor of two.

Another approach takes advantage of sum- or difference-frequency conversion in a nonlinear crystal [67]. It allows frequency shifts beyond 100 GHz, and system efficiencies in excess of 57% have already been demonstrated [68].

Lastly, arrays of coupled electro-optic micro-resonators can be used, see [69]. Frequency shift efficiencies of 99% have been reported for shifts of 28 GHz, and values up to 100 GHz seem feasible. Efficiencies are again limited by input and output coupling loss, with combined values up to 34% having been reported for similar devices [70, 71].

5.7.4. MEASUREMENTS OF THE CROSS-CORRELATION COEFFICIENT $g_{12}^{(2)}(0)$

To store classical optical pulses, we created AFCs with a bandwidth of around 1 MHz. But since the spectrum of the 795 nm photons, created by means of spontaneous parametric downconversion (SPDC), extends after filtering over 10 GHz, we increased the AFC bandwidth to 4 GHz. This resulted in a reduced recall efficiency, even for a storage time of only 43 ns.

The second-order cross correlation function is defined as $g_{12}^{(2)}(t) = P_{12}(t)/P_1P_2$, where P_1 and P_2 denote the individual detection probabilities for the two photons per photon pair, and $P_{12}(t)$ is the probability for a joint (coincidence) detection occurring with time

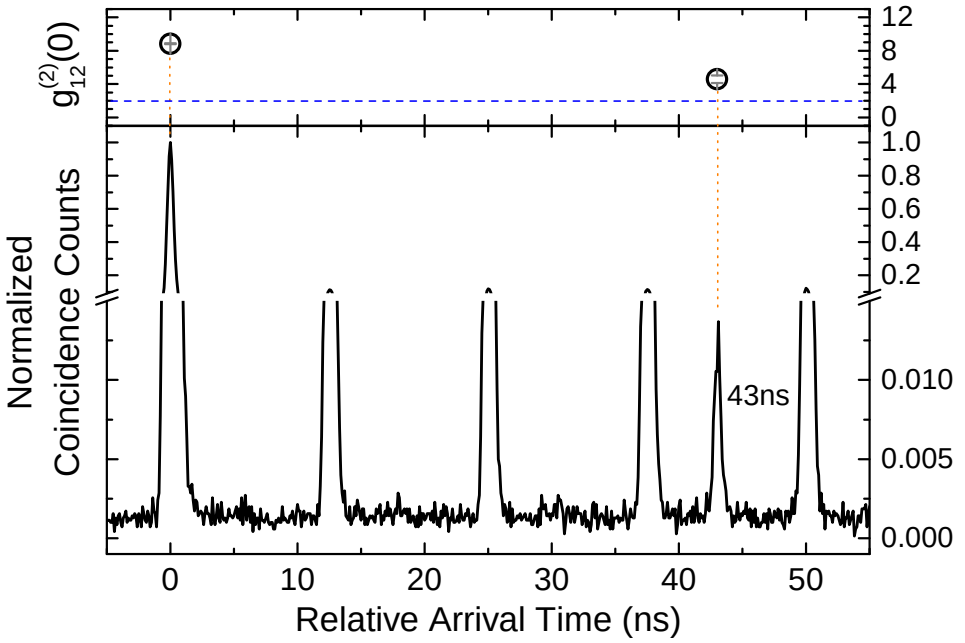

Figure 5.7: The lower and upper panels show, respectively, the coincidence-detection histogram and the 2nd order cross correlation coefficients $g^2_{12}(t)$ for transmitted as well as stored and subsequently re-emitted photons (the storage time was 43 ns). All arrival times are measured with respect to the detection time of the second member of each photon pair (the herald). The blue dashed line indicates the upper bound for classical fields of 2.

difference t. We note that the repetition period T of our pump laser is 12.5 ns, giving rise to "accidental" coincidences at integer multiples of T (see Fig. S5.7). Since these coincidences are proportional to P_1P_2 in the case of spontaneous parametric downconversion, the cross correlation coefficient can be calculated by taking the ratio of "desired" coincidence detections—in our case for t=0 ns and t=43 ns—and accidental detections: $g^{(2)}_{12}(t) = \mathrm{R}(t)/\langle \mathrm{R}(t+12.5\mathrm{ns})\rangle_\mathrm{n}$ where "$\langle..\rangle_\mathrm{n}$" denotes averaging over several repetition periods n. Analysing the coincidence histogram, we find $g^2_{12}(43ns) = 4.58 \pm 0.46$, which surpasses the classical upper bound of 2 by 5.6 standard deviations. This result demonstrates the quantum nature of our memory.

ACKNOWLEDGMENTS

The authors thank M. Grimau Puigibert, T. Chakraborty and O. P. Casas for experimental help and M. Afzelius for discussions. We acknowledge funding through the Netherlands Organization for Scientific Research, the European Union's Horizon 2020 Research and Innovation Program under Grant Agreement No. 820445 and Project Name Quantum Internet Alliance, Alberta Innovates Technology Futures, the National Sciences and Engineering Research Council of Canada, the Alberta Ministry of Jobs, Economy and Innovation's Major Innovation Fund Project on Quantum Technologies. Furthermore, W.T. ac-

knowledges funding as a Senior Fellow of the Canadian Institute for Advanced Research (CIFAR). This material is based in part on research at Montana State University sponsored by Air Force Research Laboratory under agreement number FA8750-20-1-1004.

BIBLIOGRAPHY

[1] M. F. Askarani et al., "Long-lived solid-state optical memory for high-rate quantum repeaters", Phys. Rev. Lett. **127**, 220502 (2021).

[2] H. J. Kimble, "The quantum internet", Nature **453**, 1023–1030 (2008).

[3] S. Wehner, D. Elkouss, and R. Hanson, "Quantum internet: a vision for the road ahead", Science **362**, 10.1126/science.aam9288 (2018).

[4] H.-J. Briegel, W. Dür, J. I. Cirac, and P. Zoller, "Quantum repeaters: the role of imperfect local operations in quantum communication", Phys. Rev. Lett. **81**, 5932–5935 (1998).

[5] L.-M. Duan, M. D. Lukin, J. I. Cirac, and P. Zoller, "Long-distance quantum communication with atomic ensembles and linear optics", Nature **414**, 413–418 (2001).

[6] N. Sangouard, C. Simon, H. De Riedmatten, and N. Gisin, "Quantum repeaters based on atomic ensembles and linear optics", Reviews of Modern Physics **83**, 33 (2011).

[7] N. Sinclair et al., "Spectral multiplexing for scalable quantum photonics using an atomic frequency comb quantum memory and feed-forward control", Phys. Rev. Lett. **113**, 053603 (2014).

[8] L. Jiang, J. M. Taylor, K. Nemoto, W. J. Munro, R. Van Meter, and M. D. Lukin, "Quantum repeater with encoding", Phys. Rev. A **79**, 032325 (2009).

[9] A. I. Lvovsky, B. C. Sanders, and W. Tittel, "Optical quantum memory", Nature photonics **3**, 706–714 (2009).

[10] M. Fleischhauer and M. D. Lukin, "Dark-state polaritons in electromagnetically induced transparency", Phys. Rev. Lett. **84**, 5094–5097 (2000).

[11] B. Kraus, W. Tittel, N. Gisin, M. Nilsson, S. Kröll, and J. I. Cirac, "Quantum memory for nonstationary light fields based on controlled reversible inhomogeneous broadening", PhysRevA.73.020302 **73**, 020302 (2006).

[12] M. Afzelius et al., "Demonstration of atomic frequency comb memory for light with spin-wave storage", Phys. Rev. Lett. **104**, 040503 (2010).

[13] Z.-Q. Zhou, Y.-L. Hua, X. Liu, G. Chen, J.-S. Xu, Y.-J. Han, C.-F. Li, and G.-C. Guo, "Quantum storage of three-dimensional orbital-angular-momentum entanglement in a crystal", Phys. Rev. Lett. **115**, 070502 (2015).

[14] K. F. Reim, J. Nunn, V. O. Lorenz, B. J. Sussman, K. C. Lee, N. K. Langford, D. Jaksch, and I. A. Walmsley, "Towards high-speed optical quantum memories", Nature Photonics **4**, 218–221 (2010).

[15] J.-P. Dou et al., "A broadband dlcz quantum memory in room-temperature atoms", Communications Physics **1**, 55 (2018).

[16] M. Afzelius, C. Simon, H. de Riedmatten, and N. Gisin, "Multimode quantum memory based on atomic frequency combs", Phys. Rev. A **79**, 052329 (2009).

[17] C. W. Thiel, N. Sinclair, W. Tittel, and R. L. Cone, "Optical decoherence studies of Tm^{3+} : $Y_3Ga_5O_{12}$", Phys. Rev. B **90**, 214301 (2014).

[18] C. W. Thiel, N. Sinclair, W. Tittel, and R. L. Cone, "Tm^{3+} : $Y_3Ga_5O_{12}$ Materials for spectrally multiplexed quantum memories", Phys. Rev. Lett. **113**, 160501 (2014).

[19] T. Böttger, C. W. Thiel, R. L. Cone, and Y. Sun, "Effects of magnetic field orientation on optical decoherence in Er^{3+} : Y_2SiO_5", Phys. Rev. B **79**, 115104 (2009).

[20] R. W. Equall, Y. Sun, R. L. Cone, and R. M. Macfarlane, "Ultraslow optical dephasing in Eu^{3+}:Y_2 SiO_5", Phys. Rev. Lett. **72**, 2179–2182 (1994).

[21] M. Businger, A. Tiranov, K. T. Kaczmarek, S. Welinski, Z. Zhang, A. Ferrier, P. Goldner, and M. Afzelius, "Optical spin-wave storage in a solid-state hybridized electron-nuclear spin ensemble", Phys. Rev. Lett. **124**, 053606 (2020).

[22] P. Jobez, N. Timoney, C. Laplane, J. Etesse, A. Ferrier, P. Goldner, N. Gisin, and M. Afzelius, "Towards highly multimode optical quantum memory for quantum repeaters", Phys. Rev. A **93**, 032327 (2016).

[23] G. Liu and B. Jacquier, *Spectroscopic properties of rare earths in optical materials*, Vol. 83 (Springer Science & Business Media, 2006).

[24] C. Thiel, T. Böttger, and R. Cone, "Rare-earth-doped materials for applications in quantum information storage and signal processing", Journal of luminescence **131**, 353–361 (2011).

[25] T. Zhong and P. Goldner, "Emerging rare-earth doped material platforms for quantum nanophotonics", Nanophotonics **8**, 2003–2015 (2019).

[26] F. Bussieres, N. Sangouard, M. Afzelius, H. de Riedmatten, C. Simon, and W. Tittel, "Prospective applications of optical quantum memories", Journal of Modern Optics **60**, 1519–1537 (2013).

[27] K. Heshami, D. G. England, P. C. Humphreys, P. J. Bustard, V. M. Acosta, J. Nunn, and B. J. Sussman, "Quantum memories: emerging applications and recent advances", Journal of Modern Optics **63**, PMID: 27695198, 2005–2028 (2016).

[28] E. Saglamyurek, N. Sinclair, J. A. Slater, K. Heshami, D. Oblak, and W. Tittel, "An integrated processor for photonic quantum states using a broadband light–matter interface", New Journal of Physics **16**, 065019 (2014).

[29] A. Kinos et al., *Roadmap for rare-earth quantum computing*, 2021.

[30] Y. Ma, Y.-Z. Ma, Z.-Q. Zhou, C.-F. Li, and G.-C. Guo, "One-hour coherent optical storage in an atomic frequency comb memory", Nature Communications **12**, 2381 (2021).

[31] P. Jobez, I. Usmani, N. Timoney, C. Laplane, N. Gisin, and M. Afzelius, "Cavity-enhanced storage in an optical spin-wave memory", New Journal of Physics **16**, 083005 (2014).

[32] A. Seri, A. Lenhard, D. Rieländer, M. Gündo ğan, P. M. Ledingham, M. Mazzera, and H. de Riedmatten, "Quantum correlations between single telecom photons and a multimode on-demand solid-state quantum memory", Phys. Rev. X **7**, 021028 (2017).

[33] A. Seri, D. Lago-Rivera, A. Lenhard, G. Corrielli, R. Osellame, M. Mazzera, and H. de Riedmatten, "Quantum storage of frequency-multiplexed heralded single photons", Phys. Rev. Lett. **123**, 080502 (2019).

[34] J. F. Dillon and L. R. Walker, "Ferrimagnetic resonance in rare-earth doped yttrium iron garnet. ii. terbium substitution", Phys. Rev. **124**, 1401–1413 (1961).

[35] J. H. Davidson et al., "Measurement of the thulium ion spin hamiltonian in an yttrium gallium garnet host crystal", Phys. Rev. B **104**, 134103 (2021).

[36] M. l. G. Puigibert et al., "Entanglement and nonlocality between disparate solid-state quantum memories mediated by photons", Phys. Rev. Research **2**, 013039 (2020).

[37] Y. Sun, C. W. Thiel, and R. L. Cone, "Optical decoherence and energy level structure of 0.1%tm^{3+}:$linbo_3$", Phys. Rev. B **85**, 165106 (2012).

[38] M. Grimau Puigibert, G. H. Aguilar, Q. Zhou, F. Marsili, M. D. Shaw, V. B. Verma, S. W. Nam, D. Oblak, and W. Tittel, "Heralded single photons based on spectral multiplexing and feed-forward control", Phys. Rev. Lett. **119**, 083601 (2017).

[39] E. Saglamyurek et al., "Broadband waveguide quantum memory for entangled photons", Nature **469**, 512–515 (2011).

[40] M. Afzelius and C. Simon, "Impedance-matched cavity quantum memory", Phys. Rev. A **82**, 022310 (2010).

[41] M. Sabooni, Q. Li, S. Kröll, and L. Rippe, "Efficient quantum memory using a weakly absorbing sample", Phys. Rev. Lett. **110**, 133604 (2013).

[42] J. H. Davidson, P. Lefebvre, J. Zhang, D. Oblak, and W. Tittel, "Improved light-matter interaction for storage of quantum states of light in a thulium-doped crystal cavity", Phys. Rev. A **101**, 042333 (2020).

[43] M. Sabooni, S. T. Kometa, A. Thuresson, S. Kröll, and L. Rippe, "Cavity-enhanced storage–preparing for high-efficiency quantum memories", New Journal of Physics **15**, 035025 (2013).

[44] M. Bonarota, J. Ruggiero, J. .-. L. Gouët, and T. Chanelière, "Efficiency optimization for atomic frequency comb storage", Phys. Rev. A **81**, 033803 (2010).

[45] L. Rippe, M. Nilsson, S. Kröll, R. Klieber, and D. Suter, "Experimental demonstration of efficient and selective population transfer and qubit distillation in a rare-earth-metal-ion-doped crystal", Phys. Rev. A **71**, 062328 (2005).

[46] B. Lauritzen, N. Timoney, N. Gisin, M. Afzelius, H. de Riedmatten, Y. Sun, R. M. Macfarlane, and R. L. Cone, "Spectroscopic investigations of eu^{3+}:y_2sio_5 for quantum memory applications", Phys. Rev. B **85**, 115111 (2012).

[47] M. Bonarota, J.-L. L. Gouët, and T. Chanelière, "Highly multimode storage in a crystal", New Journal of Physics **13**, 013013 (2011).

[48] M. H. Abobeih, J. Randall, C. E. Bradley, H. P. Bartling, M. A. Bakker, M. J. Degen, M. Markham, D. J. Twitchen, and T. H. Taminiau, "Atomic-scale imaging of a 27-nuclear-spin cluster using a quantum sensor", Nature **576**, 411–415 (2019).

[49] S. Guha, H. Krovi, C. A. Fuchs, Z. Dutton, J. A. Slater, C. Simon, and W. Tittel, "Rate-loss analysis of an efficient quantum repeater architecture", Phys. Rev. A **92**, 022357 (2015).

[50] H. Krovi, S. Guha, Z. Dutton, J. A. Slater, C. Simon, and W. Tittel, "Practical quantum repeaters with parametric down-conversion sources", Applied Physics B **122**, 52 (2016).

[51] E. Saglamyurek, T. Lutz, L. Veissier, M. P. Hedges, C. W. Thiel, R. L. Cone, and W. Tittel, "Efficient and long-lived zeeman-sublevel atomic population storage in an erbium-doped glass fiber", Phys. Rev. B **92**, 241111 (2015).

[52] Y. Zhao, J. Zhang, J. Stuhler, G. Schuricht, F. Lison, Z. Lu, and L. Wang, "Sub-hertz frequency stabilization of a commercial diode laser", Optics Communications **283**, 4696–4700 (2010).

[53] J. Liu, T. Liu, L. Chen, L. Zhang, G. Xu, D. Jiao, and S. Zhang, "A compact sub-hertz linewidth fabry perot cavity frequency stabilized laser for space application", Optics & Laser Technology **136**, 106777 (2021).

[54] L. Veissier, C. W. Thiel, T. Lutz, P. E. Barclay, W. Tittel, and R. L. Cone, "Quadratic zeeman effect and spin-lattice relaxation of Tm^{3+}:yag at high magnetic fields", Phys. Rev. B **94**, 205133 (2016).

[55] A. Louchet-Chauvet, R. Ahlefeldt, and T. Chanelière, "Piezospectroscopic measurement of high-frequency vibrations in a pulse-tube cryostat", Review of Scientific Instruments **90**, 034901 (2019).

[56] C. W. Thiel, R. M. Macfarlane, Y. Sun, T. Böttger, N. Sinclair, W. Tittel, and R. L. Cone, "Measuring and analyzing excitation-induced decoherence in rare-earth-doped optical materials", Laser Physics **24**, 106002 (2014).

[57] R.-C. Tongning, T. Chanelière, J.-L. Le Gouët, and M. F. Pascual-Winter, "Optical clock transition in a rare-earth-ion-doped crystal: coherence lifetime extension for quantum storage applications", in Journal of physics: conference series, Vol. 605, 1 (IOP Publishing, 2015), p. 012037.

[58] D. L. McAuslan, J. G. Bartholomew, M. J. Sellars, and J. J. Longdell, "Reducing decoherence in optical and spin transitions in rare-earth-metal-ion–doped materials", Phys. Rev. A **85**, 032339 (2012).

[59] A. Ruskuc, J. M. Kindem, J. G. Bartholomew, J. Rochman, Y. Q. Huan, and A. Faraon, "Coherent optical and spin dynamics of single 171yb ions embedded in a nanophotonic cavity", in Osa quantum 2.0 conference (2020), QTh6A.7.

[60] A. Ortu, A. Tiranov, S. Welinski, F. Fröwis, N. Gisin, A. Ferrier, P. Goldner, and M. Afzelius, "Simultaneous coherence enhancement of optical and microwave transitions in solid-state electronic spins", Nature Materials **17**, 671–675 (2018).

[61] Y. Sun, G. M. Wang, R. L. Cone, R. W. Equall, and M. J. M. Leask, "Symmetry considerations regarding light propagation and light polarization for coherent interactions with ions in crystals", Phys. Rev. B **62**, 15443–15451 (2000).

[62] M. P. Hedges, J. J. Longdell, Y. Li, and M. J. Sellars, "Efficient quantum memory for light", Nature **465**, 1052–1056 (2010).

[63] G. Kowzan, D. Charczun, A. Cygan, R. S. Trawiński, D. Lisak, and P. Masłowski, "Broadband optical cavity mode measurements at hz-level precision with a comb-based vipa spectrometer", Scientific Reports **9**, 8206 (2019).

5

[64] D. M. S. Johnson, J. M. Hogan, S.-w. Chiow, and M. A. Kasevich, "Broadband optical serrodyne frequency shifting", Opt. Lett. **35**, 745–747 (2010).

[65] R. Houtz, C. Chan, and H. Müller, "Wideband, efficient optical serrodyne frequency shifting with a phase modulator and a nonlinear transmission line", Opt. Express **17**, 19235–19240 (2009).

[66] M. Grimau Puigibert, G. H. Aguilar, Q. Zhou, F. Marsili, M. D. Shaw, V. B. Verma, S. W. Nam, D. Oblak, and W. Tittel, "Heralded single photons based on spectral multiplexing and feed-forward control", Phys. Rev. Lett. **119**, 083601 (2017).

[67] P.-C. Wang, O. Pietx-Casas, M. F. Askarani, and G. C. do Amaral, "Proposal and proof-of-principle demonstration of fast-switching broadband frequency shifting for a frequency-multiplexed quantum repeater", J. Opt. Soc. Am. B **38**, 1140–1146 (2021).

[68] T. van Leent, M. Bock, R. Garthoff, K. Redeker, W. Zhang, T. Bauer, W. Rosenfeld, C. Becher, and H. Weinfurter, "Long-distance distribution of atom-photon entanglement at telecom wavelength", Phys. Rev. Lett. **124**, 010510 (2020).

[69] Y. Hu, M. Yu, D. Zhu, N. Sinclair, A. Shams-Ansari, L. Shao, J. Holzgrafe, M. Zhang, and M. Loncar, "Electro-optic frequency shifting using coupled lithium-niobate microring resonators", in Conference on lasers and electro-optics (2020), STu4J.4.

[70] S. F. Preble, Q. Xu, and M. Lipson, "Changing the colour of light in a silicon resonator", Nature Photonics **1**, 293–296 (2007).

[71] M. Lauermann et al., "Integrated optical frequency shifter in silicon-organic hybrid (soh) technology", Opt. Express **24**, 11694–11707 (2016).

6

TOWARDS A MONOLITHIC, ALIGNMENT-FREE AND HIGHLY-EFFICIENT QUANTUM MEMORY FOR LIGHT

Antariksha Das, Jacob H. Davidson, Anna L. Tchebotareva, Wolfgang Tittel

Building quantum repeater-based quantum networks requires high-efficiency and multi-mode quantum memories for light with sufficient storage time to allow for feed-forward control. While a lot of progress has been reported over the past decade, all demonstrations were of the proof-of-principle type, making scaling to large networks impossible. Here we investigate a monolithic and alignment-free (pre-aligned) solid-state quantum memory based on a thulium-doped $Y_3Ga_5O_{12}$ (Tm:YGG) crystal. Simulations using realistic parameters suggest that this device is suitable to achieve efficient and faithful storage of single photon qubits with high multi-mode capacity for quantum networking.

Large portions of this chapter will be submitted to a journal.

6.1. INTRODUCTION

To reach high storage efficiency in the AFC protocol, a large optical depth of the storage medium - here thulium-doped crystals - is required. This allows enhanced light-matter interaction, and thus a high probability of absorption and emission. There are different ways to increase the optical depth of the quantum memory in order to improve efficiency. For example, one can use crystals with higher doping concentrations of ions, increase the length of the crystal, or select rare-earth elements with optical transitions that have high oscillator strength. However, one can increase the doping concentration only to a certain level. Beyond that, it only increases the inhomogeneous linewidth and not the absorption coefficient [1]. Increasing the length of the crystal is also not a promising solution, as this would bring many technical complexities and a very long crystal is inconvenient to integrate with other miniaturized quantum hardware. Furthermore, we would not want to exclude rare-earth elements with very good coherence properties just because they have low oscillator strength of transition. One promising way to solve this issue is to embed the crystal within an asymmetric **impedance-matched** optical cavity [2, 3]. Impedance matching means that the transmission from the first mirror matches the round-trip loss inside the cavity (this loss comes from the absorption of the crystal and the second mirror transmission); in this case, there would not be any reflection from the cavity. If the second mirror is highly reflective (preferably 100% reflectivity), nothing is transmitted through the cavity either. Thus, all energy would be absorbed by the crystal inside the cavity.

6.2. IMPEDANCE MATCHED CAVITY

The “impedance matching" term was first used in radio frequency electronics, where it refers to the condition that the reflected power from a load is minimum or the power transfer to the load is maximum. When used in an optical cavity, it means that the light reflected from the input mirror of a cavity is minimized by adjusting the reflectivity of the cavity mirrors [4–7].

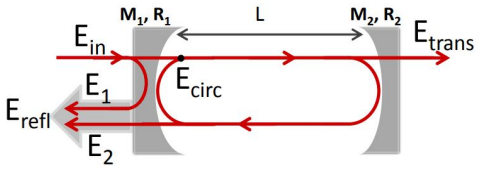

Figure 6.1: A schematic diagram of a Fabry-Perot cavity. (The Figure is adapted from [7])

Here, we consider a Fabry-Perot cavity composed of two mirrors, M_1 and M_2, spaced by a distance L, with reflectivity R_1 and R_2, as shown in Figure 6.1. Without loss of generality, the round-trip loss inside the cavity is set to $1-R_2e^{2\alpha L}$. At steady state, the circulating field inside the cavity, E_{circ} can be written as the sum of two parts: the incoming field that is transmitted through the input mirror $E_{in}t_1$ and the circulating field after one round trip at the same point, $E_{\text{circ}}\, e^{-2\alpha L - i\omega\frac{2L}{c}}$ (see the black dot in Figure 6.1) with

$$E_{\text{circ}} = E_{\text{circ}}\, r_2 r_1 e^{-2\alpha L - i\omega \frac{2L}{c}} + E_{\text{in}}\, t_1 \tag{6.1}$$

Here, $r_1 = \sqrt{R_1}$ and $t_1 = \sqrt{1-R_1}$ are the reflection and transmission coefficients for the input mirror M_1. Similarly r_2 and t_2 are the reflection and transmission coefficients for the rear mirror M_2. From Equation 6.1, the circulating field inside the cavity and the transmitted field after the second mirror can be written as,

$$E_{\text{circ}} = \frac{E_{\text{in}}\, t_1}{1 - r_2 r_1 e^{-2\alpha L - i\omega \frac{2L}{c}}} \tag{6.2}$$

$$E_{\text{trans}} = E_{\text{circ}}\, t_2 \tag{6.3}$$

The reflected field can be written as a sum of two parts, the directly reflected field from the front mirror: $E_1 = -r_1 E_{\text{in}}$ and the field leaking out from the circulating field inside the cavity through the front mirror: $E_2 = E_{\text{circ}}\, t_1 r_2 e^{-2\alpha L - i\omega \frac{2L}{c}}$. Since the electric field is reflected from a boundary with a higher refractive index, we put a minus sign in E_1 to represent the 180° phase shift of the reflected field relative to the incident field. The reflected field then can be expressed as,

$$E_{\text{refl}} = E_1 + E_2 \tag{6.4}$$

Depending on the reflected field, there are three possible scenarios: under-coupled, over-coupled, and impedance matched. Under-coupling and over-coupling conditions take place when the reflected field is dominated by the directly reflected field, E_1, and the field that leaks out from the cavity, E_2, respectively. Impedance matching is satisfied when the two fields E_1 and E_2 have equal amplitude, but the overall reflected field is zero since they have opposite phases and no power is reflected. They can be described by the following equations:

- Cavity is **under coupled**: $R_1 > R_2 e^{-2\alpha L}$
- Cavity is **over coupled**: $R_1 < R_2 e^{-2\alpha L}$
- Cavity is **impedance matched**: $R_1 = R_2 e^{-2\alpha L}$

In Fig.6.2, we consider an absorbing rare-earth-ion crystal inside the cavity and plot the reflected intensity as a function of the light frequency and the optical depth of the medium. We assume the front mirror reflectivity is $R_1 = 0.82$, and the back mirror reflectivity $R_2 = 0.99$. The Figure shows the reflected intensity goes to 0 only when the light is in resonance with the cavity and the cavity is impedance matched. In other words, when the impedance matching criterion is satisfied, the round-trip absorption by the ions is matched with the transmission from the first mirror, i.e $1 - R_1 = 1 - e^{-2\alpha L}$.

Since there is no reflection or transmission from the cavity, all incoming light will be absorbed by the ions and 100% energy transfer from the photon to the ions can be achieved. So a weakly absorbing material inside an impedance-matched cavity would behave like a highly absorbing material, which is required to obtain high storage efficiency in a quantum memory.

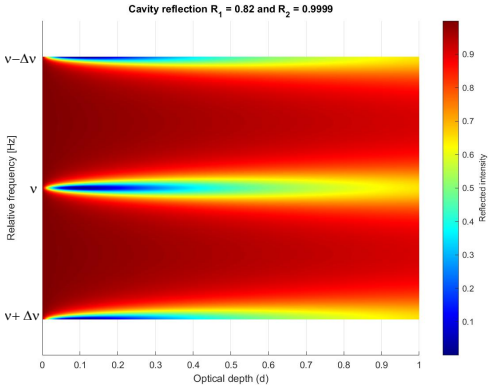

Figure 6.2: The reflected intensity is plotted as a function of the frequency of the incoming light and the optical depth of the medium. The cavity is impedance matched when the round-trip absorption by the medium is matched with the transmission from the first mirror.

6.3. QUANTUM MEMORY EFFICIENCY IN AN IMPEDANCE-MATCHED CAVITY

For a single pass crystal, the memory efficiency can be expressed as

$$\eta^{AFC}_{\text{single-pass}} = \tilde{d}^2 \exp(-\tilde{d}) \exp(-d_0)\eta_{\text{deph}} \tag{6.5}$$

where $\tilde{d}$ is the optical depth, averaged over the input photon bandwidth. For square peaks $\tilde{d} = d/F$, where F is the comb finesse $F = \Delta/\gamma$. The factor η_{deph} accounts for the dephasing due to the finite width of the peaks. For square peaks it can be written as $\eta_{\text{deph}} = \text{sinc}^2(\pi/F)$ and for gaussian AFC peaks $\eta_{\text{deph}} = e^{-\frac{7}{F^2}}$. The efficiency of a single-pass memory, where the output echo is emitted in the same mode as the input is bounded by 54% due to the re-absorption of the echo, which is accounted for by the factor $\exp(-\tilde{d})$ in the equation above.

To overcome the weak absorption of the crystal, it was proposed to use an optical cavity around the crystal and operate it in the impedance-matched regime [2, 3]. The impedance-matching condition is given by $R_1 = R_2 \exp(-2\tilde{d}) \exp(-2d_0)$. Hence, in the presence of a cavity, the AFC memory efficiency can be expressed as [8]

$$\eta^{AFC}_{\text{cavity}} = \left[\frac{2(1-R_1)\sqrt{R_2}}{\left(1-\sqrt{R_1R_2}e^{-(\frac{d}{F}+d_0)}\right)^2}\right]^2 \left(\frac{d}{F}\right)^2 e^{-2(\frac{d}{F}+d_0)}\eta_{\text{deph}}$$

where η_{deph} describes the reduction in efficiency due to the finite individual teeth width of the frequency comb. If the cavity is lossless, $\tilde{d} \ll 1$, and the input photon bandwidth is much smaller than the cavity linewidth (FWHM), one can show that in an impedance-matched cavity, the AFC memory efficiency is only limited by the intrinsic dephasing η_{deph}

$$\eta_{\text{cavity}} = \eta_{\text{deph}} \tag{6.6}$$

However, in practice, η_{cavity} is limited by the quality of the spatial interference between all the modes of the cavity. If the light is out of resonance or if the cavity is empty, all the incoming light would be rejected.

6.4. EXPERIMENTAL SETUP

The memory cavity-crystal is made of a 1.4 cm long 1% Tm: $Y_3Ga_5O_{12}$ (Tm:YGG) crystal and placed in an ADR-based cryostat operating at a temperature of 600 mK. The end facets of the crystal are reflection coated, with reflectivities R_2 = 99% on the rear and R_1 = 82% on the front side. The reflectivity value for the front facet is chosen to allow for impedance matching at the 795.32 nm Tm:YGG absorption wavelength by meeting the condition $R_1 = R_2 \exp(-2\tilde{d})$, with $\tilde{d}$ the average optical depth across the cavity resonance bandwidth. To facilitate the use of the cavity-crystal quantum memory in a practical quantum repeater setting, its input is pigtailed to a single-mode fiber for 795 nm wavelength (see Inset 2 of Fig.6.3). The in-out coupling efficiency of the cavity-crystal system is only 22-24%, which is the only major limitation of our novel design. There is also spatial mode mismatching because the curvature of the rear mirror does not match that of the input laser beam width.

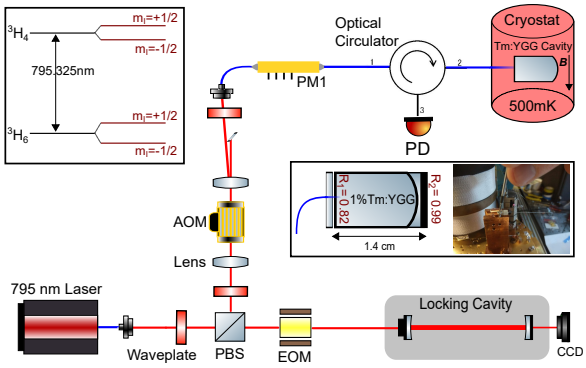

Figure 6.3: **A schematic diagram of the experimental setup:** AOM: acousto-optic modulator; EOM: electro-optic modulator; PD: photodetector to collect the reflected light from the cavity; CCD: charge-coupled device camera; ***B***: Magnetic field. Inset 1: Simplified energy level diagram of the $^3H_6 \rightarrow {}^3H_4$ optical transition of Tm^{3+} in $Y_3Ga_5O_{12}$. Only the lowest crystal field levels of each electronic manifold are shown. Inset 2: A schematic of the cavity-crystal and the real device of 1.4 cm long Tm:YGG cavity-crystal.

A schematic of our setup is presented in Fig.6.3. The light propagates along the 1.4 cm-long < 110 > axis of the crystal and its polarization is linear at the crystal input, orthogonal to the < 111 >-direction. A magnetic field is applied parallel to the < 111 >-direction using a superconducting solenoid. The magnetic field strength is detected using a Hall sensor mounted directly above the crystal.

The optical pulse sequence for our measurements is obtained from a continuous-wave external-cavity Toptica DLPro tunable diode laser emitting at 795.32 nm (vacuum)

to address the $^3H_6 \rightarrow {}^3H_4$ transition of Tm^{3+} ions in the crystal. A programmable pulse-blaster controls the timing sequence. The light is gated and shaped with a single-pass free-space acoustic-optic modulator (AOM). The 1st order diffracted light beam from the AOM is sent through a series of optical components (waveplates and polarizing beam-splitter) and a phase modulator (PM) where the frequency of the light is shifted through a serrodying signal created by an arbitrary waveform generator (AWG). The reflected signal from the Tm:YGG cavity-crystal is collected using an optical circulator and detected using an amplified silicon photodetector.

A small fraction of the light from the diode laser is used to frequency lock the laser to a high finesse cavity using the Pound-Drever-Hall method [9]. For good stability, the frequency stabilization setup is kept on a separate optical breadboard and isolated from the main optical setup. After passing through an electro-optic modulator (EOM)—for the creation of frequency sidebands—, the light beam is sent through a series of optical components for proper coupling into the temperature-stabilized high-finesse optical cavity. This allows us to obtain a narrow laser linewidth of a few tens of kilohertz.

6.5. RESULTS

In the following section, we describe the initial characterizations of the memory. First, we examined how cavity resonances interact with the Tm:YGG absorption profile. To capture the cavity resonances of the Tm:YGG cavity-crystal system, we slowly swept the laser frequency across the inhomogeneous Tm absorption line centered at 795 nm. As shown in Fig.6.6, the reflected spectra of different cavity resonances were detected and normalized to the input light intensity. The free spectral range of the cavity-crystal is measured to be around 6.2 GHz, which is in accordance with the theoretical prediction. The cavity resonances are convoluted with the 55 GHz inhomogeneously broadened Lorentzian absorption profile of the Tm:YGG, centered around 795.32 nm [10, 11]. The full-width-at-half-maximum (FWHM) linewidth of the cavity mode near the center of the inhomogeneously broadened Tm:YGG absorption line is around one GHz. On the other hand, far away from the center of the inhomogeneously broadened Tm:YGG absorption line, since the absorption by Tm^{3+} ions is low, the FWHM linewidth of the cavity mode is around hundreds of MHz. We note that the reflected intensity at the cavity resonances decreases and reaches a minimum at the wing of the absorption profile of the Tm:YGG. Given the front mirror reflectivity $R_1 = 82\%$ and back mirror reflectivity of $R_2 = 99\%$, the impedance-matching condition, $R_1 = R_2 \exp(-2\tilde{d})$, is satisfied for optical depth $\tilde{d} \approx 0.1$. This holds true at wavelengths 795.22 nm and 795.43 nm. Outside the absorption line, the intensity at the cavity resonances increases again.

As emphasized above, the impedance matching condition is fulfilled when the light is in resonance with the cavity and the reflected intensity goes to 0. Thus, it is very important to identify the center of the cavity resonances. To do that, first, we tune our laser to a specific cavity mode of the Tm:YGG cavity-crystal and then we burn a 2 MHz broad spectral hole at many different frequencies within that specific cavity mode. We observe that the spectral holes have an asymmetric lineshape. Depending on the frequencies where we burn our spectral hole, the degree of asymmetry in the spectral lineshape changes. To account for that we fit the spectral holes using the expression in Eq.6.7 for Fano resonances [12]. Fano resonances are widely studied in nanophotonics and arise from the

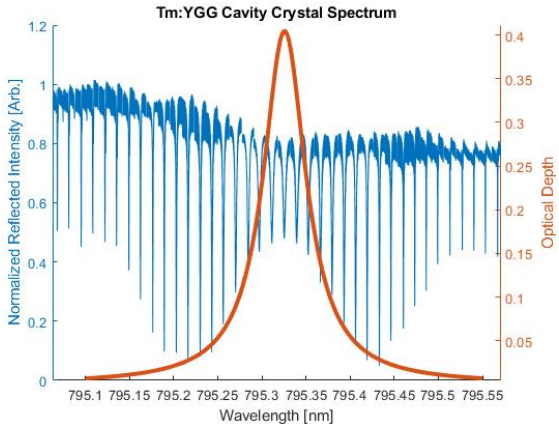

Figure 6.4: The measured reflection spectra (blue) of the Tm:YGG cavity-crystal system (left Y axis). The simulated Lorentzian profile (orange) shows the absorption of the Tm:YGG crystal without cavity (right Y axis).

constructive and destructive interference of a narrow discrete resonance with a broad spectral line or continuum [13]. A Fano resonance exhibits a distinctly asymmetric shape with the following functional form:

$$f(F,\gamma,\omega_0) = \frac{\left(F\gamma+\omega-\omega_0\right)^2}{(\omega-\omega_0)^2+\gamma^2} \tag{6.7}$$

where ω_0 and γ are standard parameters that denote the position and width of the resonance, respectively and F is the so-called Fano parameter, which describes the degree of asymmetry.

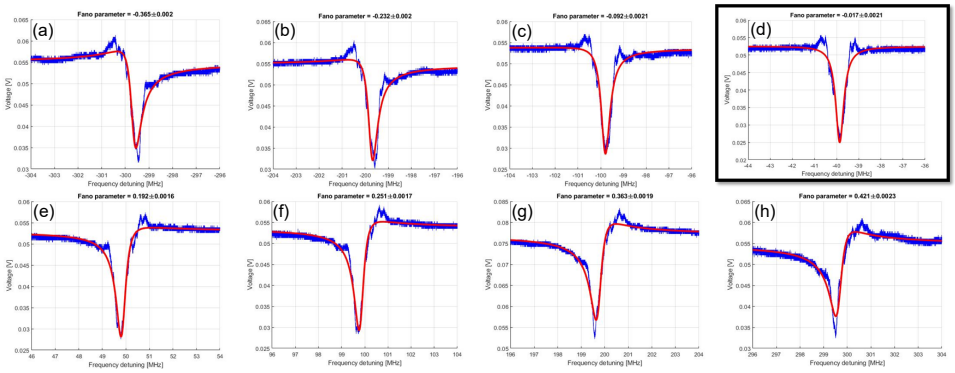

Figure 6.5: 2 MHz wide spectral holes are burned in the absorption line of the Tm:YGG cavity-crystal at different frequencies for a distinct cavity mode. As we start approaching the center of the cavity mode from (a)-(c), the spectral lineshape becomes more symmetric. in (d), we hit the center of the cavity mode. As we start moving away from the center, the spectral lineshape becomes asymmetric again, as described in (e)-(h).

As shown in Fig.6.5(a), the spectral lineshape of the 2 MHz broad spectral hole is

asymmetric and fits well with the Fano equation. As we start approaching the center of the cavity mode from Fig.6.5(a)-(c), the spectral lineshape becomes more symmetric. Then we hit the center of the cavity mode and the spectral lineshape of the spectral hole becomes symmetric with a Fano parameter very close to 0. As we start moving away from the center, the spectral lineshape becomes again asymmetric, as described in Fig.6.5(e)-(h). The degree of asymmetry in the spectral lineshape or the Fano parameter (F) guides us to find the center of the cavity modes.

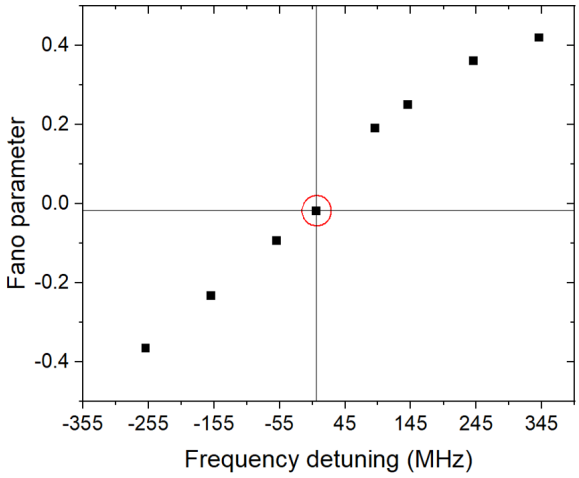

Figure 6.6: The fitted Fano parameter is plotted as a function of frequency detuning for a distinct cavity mode. The red circle indicates the value of the Fano parameter where we hit the center of the cavity mode.

To demonstrate the storage of classical laser pulses in our cavity-assisted Tm:YGG, we implement the atomic frequency comb-based quantum memory protocol [14]. Even though we were able to store classical laser pulse up to 60 μs of storage time, the storage efficiency was only a few percent [15]. This was mainly limited by the low in-out device coupling efficiency of 22-24%. In the future, we must improve this coupling in order to make an efficient cavity-assisted AFC quantum memory out of Tm:YGG crystal.

6.6. CONCLUSION

To summarize, we have demonstrated cavity-enhanced light-matter interaction in a monolithic and fiber-coupled cavity that can allow storing quantum states of light with high efficiency. To further improve key properties, several modifications are required. First, to reach an efficiency close to 100%, we need to improve the in-out device coupling efficiency. In addition, the finesse of the AFC has to be increased. As this is only possible if the total AFC width is smaller than the ground state splitting, in our case, 40 MHz/T, this limits the available bandwidth per spectral channel, implying the need for suitably adapted sources of quantum light. In principle, our fully fiber-pigtailed, cavity-enhanced Tm:YGG quantum memory can be integrated efficiently into the quantum repeater architecture outlined in [16].

BIBLIOGRAPHY

[1] F. Könz, Y. Sun, C. Thiel, R. Cone, R. Equall, R. Hutcheson, and R. Macfarlane, "Temperature and concentration dependence of optical dephasing, spectral-hole lifetime, and anisotropic absorption in eu 3+: y 2 sio 5", Physical Review B **68**, 085109 (2003).

[2] M. Afzelius and C. Simon, "Impedance-matched cavity quantum memory", Phys. Rev. A **82**, 022310 (2010).

[3] S. A. Moiseev, S. N. Andrianov, and F. F. Gubaidullin, "Efficient multimode quantum memory based on photon echo in an optimal qed cavity", Phys. Rev. A **82**, 022311 (2010).

[4] J. H. Davidson, P. Lefebvre, J. Zhang, D. Oblak, and W. Tittel, "Improved light-matter interaction for storage of quantum states of light in a thulium-doped crystal cavity", Phys. Rev. A **101**, 042333 (2020).

[5] M. Sabooni, S. T. Kometa, A. Thuresson, S. Kröll, and L. Rippe, "Cavity-enhanced storage–preparing for high-efficiency quantum memories", New Journal of Physics **15**, 035025 (2013).

[6] P. Jobez, I. Usmani, N. Timoney, C. Laplane, N. Gisin, and M. Afzelius, "Cavity-enhanced storage in an optical spin-wave memory", New Journal of Physics **16**, 083005 (2014).

[7] Q. Li, "Quantum memory development and new slow light applications in rare-earth-ion-doped crystals", (2018).

[8] M. Afzelius and C. Simon, "Impedance-matched cavity quantum memory", Phys. Rev. A **82**, 022310 (2010).

[9] E. D. Black, "An introduction to pound–drever–hall laser frequency stabilization", American journal of physics **69**, 79–87 (2001).

[10] C. W. Thiel, N. Sinclair, W. Tittel, and R. L. Cone, "Optical decoherence studies of Tm^{3+} : $Y_3Ga_5O_{12}$", Phys. Rev. B **90**, 214301 (2014).

[11] C. W. Thiel, N. Sinclair, W. Tittel, and R. L. Cone, "Tm^{3+} : $Y_3Ga_5O_{12}$ Materials for spectrally multiplexed quantum memories", Phys. Rev. Lett. **113**, 160501 (2014).

[12] M. F. Limonov, M. V. Rybin, A. N. Poddubny, and Y. S. Kivshar, "Fano resonances in photonics", Nature Photonics **11**, 543–554 (2017).

[13] A. E. Miroshnichenko, S. Flach, and Y. S. Kivshar, "Fano resonances in nanoscale structures", Reviews of Modern Physics **82**, 2257 (2010).

[14] M. Afzelius, C. Simon, H. de Riedmatten, and N. Gisin, "Multimode quantum memory based on atomic frequency combs", Phys. Rev. A **79**, 052329 (2009).

[15] M. F. Askarani et al., "Long-lived solid-state optical memory for high-rate quantum repeaters", Phys. Rev. Lett. **127**, 220502 (2021).

[16] N. Sinclair et al., "Spectral multiplexing for scalable quantum photonics using an atomic frequency comb quantum memory and feed-forward control", Phys. Rev. Lett. **113**, 053603 (2014).

7

CONCLUSIONS AND OUTLOOK

In this chapter, I will summarize the results of this thesis. This is followed by a brief discussion on further improvements, and the proposal of some interesting future projects. Finally, I conclude this thesis with some remarks on the impact of the research findings on the study of thulium-doped YGG, optical quantum memories, and frequency multiplexed quantum repeaters.

7.1. SUMMARY OF RESULTS

This thesis describes progress in creating and improving optical quantum memories using a thulium-doped garnet for use in frequency multiplexed quantum repeaters. In particular, it focuses on improvements to memory storage time and memory recall efficiency.

The work described in my thesis marks a significant advance in the development of optical quantum memories. Yet, substantial theoretical and experimental work remains before it will lead to applications that can be used in actual practice.

- **Chapter** 3: We perform an in-depth spectroscopic investigation of the 795 nm transition in Tm:YGG. The population and the decoherence dynamics are studied at temperatures as low as 500 mK. We measure the magnetic field dependent spectral diffusion finding that in the presence of a few hundred Gauss, this crystal offers an optical coherence time exceeding one millisecond and a ground-state Zeeman-level lifetime as long as tens of seconds. By taking advantage of these two unique spectroscopic properties, we implement a persistent atomic frequency comb (AFC) quantum memory protocol to demonstrate multiplexed storage of classical laser pulses in the temporal and spectral domains.

- **Chapter** 4: We conduct an in-depth study of frequency-dependent rate equations to understand, improve and optimize the optical pumping process for creating efficient atomic frequency comb-based memories in Tm:YGG. The modeling and the findings of this chapter provide a recipe for burning well-understood spectral features and atomic-frequency-comb quantum memories in this material.

- **Chapter** 5: We show the storage of classical laser pulses for storage times up to 100 μs, simultaneous storage of light pulses at multiple frequencies, as well as a proof-of-principle demonstration of frequency selective read-out for frequency multiplexed quantum repeaters using a Tm:YGG optical memory. These results show the promise of Tm:YGG as long-lived optical quantum memory for frequency multiplexed quantum repeater architectures without the need for AFC spin-wave storage.

- **Chapter** 6: We address the experimental limits imposed by our memory system, indicating routes for improvement in memory parameters. We discuss the possibility to use a monolithic impedance-matched cavity quantum memory to improve the storage efficiency in Tm:YGG. Our results suggest a path to high-efficiency quantum memories based on impedance-matched cavity AFC protocol in the Tm:YGG crystal.

7.2. POTENTIAL FUTURE PROJECTS

- **Improvements to the current thulium-based quantum memory.**
  In terms of two-level AFC quantum memories, Tm:YGG is one of the most promising and attractive candidates. But there is still a lot of room for the improvement of our particular thulium-based quantum memory using the AFC-based memory scheme.

  1. **Microwave spectroscopic investigation of Tm:YGG.** With the addition of microwave control to our system, we gain control of the spin population in the YGG lattice [1, 2]. We can address different ensembles of ions within the crystal and initialize the population on a smaller timescale compared to the long optical lifetime of this material. It can be possible to improve two-level optical AFC storage using RF pulses with appropriate frequency and magnitude, applied to the spin transition to maintain good optical coherence[1].
  2. **Spectroscopic investigations and optical decoherence dynamics in Tm:YGG at millikelvin temperatures.** The experiments discussed in this thesis are performed at a temperature of 500 mK- 600 mK. Decreasing the temperatures further may not only improve the coherence time T_2 but also the storage efficiency, by increasing the spin lifetime. Spectroscopic investigations of a Tm:$LiNbO_3$ bulk crystal furthermore show that spectral diffusion decreases when lowering the temperature[3]. This implies the possibility to extend the storage time beyond 100 μs.

     Spectral diffusion due to ion-ion interaction, for example, a long-range quadrupole-quadrupole interaction between Tm^{3+} ions, is likely to play a role in the observed memory decay [4]. The presence of such mechanisms has been conjectured in the case of Tm:YAG, which features the same site symmetry as Tm:YGG [5]. Decreasing the Tm doping concentration may help reduce the impact of this interaction.
  3. **Improved coherence and storage using optical clock transitions in Tm:YGG.** We note that the AFCs discussed in this thesis are created using uncontrolled,

optically, and magnetically inequivalent subsets of Tm^{3+} ions. There are six subgroups of magnetically inequivalent Tm^{3+} ions in the YGG lattice with different local orientations. Small magnetic field fluctuations in the crystalline environment of the YGG lattice due to surrounding nuclear spins or an unstable current supply used to create an external magnetic field can cause spectral diffusion and hence a reduction of the optical coherence time. To reduce spectral diffusion caused by varying magnetic fields at the Tm sites, it would be best to choose a specific site by means of direction and polarization of the light beam and a magnetic field direction for which the 795 nm Tm transition becomes insensitive to first-order magnetic field fluctuations. These transitions are often referred to as ZEFOZ (ZEro First-Order-Zeeman) transitions [6–9] or the optical clock transitions. It can be extremely useful for reducing decoherence due to noisy magnetic fields. These clock transitions exist in Tm:YGG [10]. Cutting the Tm:YGG crystal along the ZEFOZ axis can certainly improve the optical coherence time and hopefully would allow optical storage of beyond 100 μs.

4. **Better crystal growth.** The Tm:YGG crystal that we used for our experiment is birefringent which is inconsistent with the crystal symmetry and suggests imperfect crystal growth. Using a non-birefringent crystal and selecting a specific polarization state at its input will allow for optimizing photon-ion interaction, resulting in improved optical depth and memory efficiency.

5. **Highly efficient impedance-matched cavity quantum memory in Tm:YGG.** As discussed in chapter 6, the storage efficiency of quantum memory must be enhanced in order to be used in practical quantum networking purposes. To counter the effects of the limited optical depth of the used Tm:YGG crystal for our experiment, the light-atom interaction has to be enhanced using an impedance-matched cavity. This also removes the problem of re- absorption of photons that are emitted in the forward direction.

- **Telecom-compatible quantum memory in Tm:YGG.**
Telecom wavelength-compatible quantum memories are interesting because they can be integrated efficiently into the existing fiber-optic communication infrastructure without the need for any frequency conversion. Other than erbium, thulium-doped crystals can be a potential candidate in this regard. In Tm^{3+}, the non-ground state transition from the $^3F_4$ to $^3H_4$ level is around 1450 nm wavelength. In this case, the $^3H_6$ ground state can act as a shelving level for AFC-based quantum memories. As the transition frequency from the $^3H_6$ to the $^3F_4$ level is on the order of 100 THz, in cryogenic temperature, there will not be any phonon-induced population relaxation between these two levels. Thus, optical pumping can be performed efficiently.

- **Spectro-temporal storage and on-demand readout in Tm:YGG.**
Although this thesis focuses on 2-level AFC quantum memory and its role in frequency-multiplexed quantum repeaters, in practice, multiplexing across all possible degrees of freedom, including time and space will be required to counter entangle-

ment distribution rate-vs.-distance decay. In this context, it is important to create quantum memories that are compatible with any multiplexing strategy. We demonstrated long-lived storage along with spectral multiplexing in Tm:YGG. Using the 2-level AFC [11], the maximum storage time obtained from our memory is 100 μs. It may be possible to further improve the storage time and achieve on-demand recall by temporarily transferring the optical coherence between the $^3H_6$ and $^3H_4$ levels to coherence between the $^3H_6$ and $^3F_4$ levels, similar to the transfer of coherence in spin-wave AFC protocol [12]. Furthermore, this will also allow us to store many temporal modes simultaneously. For this reason, the coherence properties and the suitability of the $^3F_4$ state for such a transfer need to be investigated. Combining the 2-level AFC protocol with a controlled reversible inhomogeneous broadening-based quantum memory approach would also allow one to prevent the pre-set rephasing of coherence by adding controlled inhomogeneous broadening of each AFC tooth. Rephasing would only occur after reversing the process, and readout would be possible on-demand.

Along with the quantum memory, finding effective methods to construct frequency multiplexed sources and frequency-resolved Bell state measurements[13–16] are required in order to demonstrate frequency multiplexing for a full elementary link which remains a key goal.

- **Improvements of the source.**
  For our quantum repeater application, ideal single-pair entangled photon sources have to be used if resources should remain reasonable. Emitters, such as those based on parametric down-conversion or four-wave mixing, are convenient testbeds and good for initial demonstrations but also emit multiple pairs that reduce fidelities [17]. Some promising pair sources that would be suitable in this regard are quantum dots [18–20].

- **Improvement on the Bell-state measurement.**
  The efficiency of a linear optical Bell-state measurement can be enhanced if implemented through controlled-phase quantum gates [21] or auxiliary photons [22–25]. Quantum gates could be implemented using optical-to-microwave conversion protocols, thereby benefiting from superconducting quantum circuits.

For quantum memories, further testing, and development of rare-earth-ion-doped crystals are needed to identify further improved material candidates. We must explore all the possibilities to improve device performances, but also consider that a quantum device will never achieve its desired performance in every single aspect. Advanced quantum applications will be comprised of multiple components, it is likely that certain devices may need to compensate for the drawbacks of others; perhaps resulting in a trade-off of overall performance [26].

7.3. OUTLOOK

Rare-earth-ion-doped materials are widely used in a number of different technologies today [27–33]. Thulium-doped garnets, in particular Tm:YGG, is one of the most promis-

ing materials because of the long optical coherence time and easily accessible optical transition, within the range of commercial diode lasers. Its simple energy level structure compared to other rare earth-doped materials makes it straightforward to use. The only drawback is likely to be the gallium spins or additional magnetic impurities in the crystalline environment. This can affect the coherence properties of the material in presence of a magnetic field when it is favorable to create long-lived persistent spectral structures. For example an AFC for long-lived optical storage. However, they can also become a resource if used correctly [34, 35].

Further research is required to set the stage for a bright future of both fundamental and practical discoveries. In the coming years, we can expect to see functional quantum networks over large distances. We can hope that this research will bring together scientists, engineers, and researchers from various disciplines and across the governments and industry. It will likely to generate new opportunities, ideas, and avenues for innovation, while simultaneously garnering public awareness of the exciting quantum world.

This thesis covers a small part of the required components that are needed to develop quantum communication technology.

BIBLIOGRAPHY

[1] R. Lauro, T. Chanelière, and J.-L. Le Gouët, "Adiabatic refocusing of nuclear spins in tm^{3+}:yag", Phys. Rev. B **83**, 035124 (2011).

[2] M. F. Pascual-Winter, R.-C. Tongning, T. Chanelière, and J.-L. Le Gouët, "Spin coherence lifetime extension in tm^{3+}:yag through dynamical decoupling", Phys. Rev. B **86**, 184301 (2012).

[3] C. Thiel, Y. Sun, T. Böttger, W. Babbitt, and R. Cone, "Optical decoherence and persistent spectral hole burning in tm3+: linbo3", Journal of luminescence **130**, 1598–1602 (2010).

[4] M. F. Askarani et al., "Long-lived solid-state optical memory for high-rate quantum repeaters", Phys. Rev. Lett. **127**, 220502 (2021).

[5] C. W. Thiel, R. M. Macfarlane, Y. Sun, T. Böttger, N. Sinclair, W. Tittel, and R. L. Cone, "Measuring and analyzing excitation-induced decoherence in rare-earth-doped optical materials", Laser Physics **24**, 106002 (2014).

[6] R.-C. Tongning, T. Chanelière, J.-L. Le Gouët, and M. F. Pascual-Winter, "Optical clock transition in a rare-earth-ion-doped crystal: coherence lifetime extension for quantum storage applications", in Journal of physics: conference series, Vol. 605, 1 (IOP Publishing, 2015), p. 012037.

[7] D. L. McAuslan, J. G. Bartholomew, M. J. Sellars, and J. J. Longdell, "Reducing decoherence in optical and spin transitions in rare-earth-metal-ion–doped materials", Phys. Rev. A **85**, 032339 (2012).

[8] A. Ortu, A. Tiranov, S. Welinski, F. Fröwis, N. Gisin, A. Ferrier, P. Goldner, and M. Afzelius, "Simultaneous coherence enhancement of optical and microwave transitions in solid-state electronic spins", Nature Materials **17**, 671–675 (2018).

[9] A. Ruskuc, J. M. Kindem, J. G. Bartholomew, J. Rochman, Y. Q. Huan, and A. Faraon, "Coherent optical and spin dynamics of single 171yb ions embedded in a nanophotonic cavity", in Osa quantum 2.0 conference (2020), QTh6A.7.

[10] J. H. Davidson et al., "Measurement of the thulium ion spin hamiltonian in an yttrium gallium garnet host crystal", Phys. Rev. B **104**, 134103 (2021).

[11] M. Afzelius, C. Simon, H. de Riedmatten, and N. Gisin, "Multimode quantum memory based on atomic frequency combs", Phys. Rev. A **79**, 052329 (2009).

[12] M. Afzelius et al., "Demonstration of atomic frequency comb memory for light with spin-wave storage", Phys. Rev. Lett. **104**, 040503 (2010).

[13] R. Ikuta, R. Tani, M. Ishizaki, S. Miki, M. Yabuno, H. Terai, N. Imoto, and T. Yamamoto, "Frequency-multiplexed photon pairs over 1000 modes from a quadratic nonlinear optical waveguide resonator with a singly resonant configuration", Phys. Rev. Lett. **123**, 193603 (2019).

[14] A. Seri, D. Lago-Rivera, A. Lenhard, G. Corrielli, R. Osellame, M. Mazzera, and H. de Riedmatten, "Quantum storage of frequency-multiplexed heralded single photons", Phys. Rev. Lett. **123**, 080502 (2019).

[15] M. Grimau Puigibert, G. H. Aguilar, Q. Zhou, F. Marsili, M. D. Shaw, V. B. Verma, S. W. Nam, D. Oblak, and W. Tittel, "Heralded single photons based on spectral multiplexing and feed-forward control", Phys. Rev. Lett. **119**, 083601 (2017).

[16] N. B. Lingaraju, H.-H. Lu, D. E. Leaird, S. Estrella, J. M. Lukens, and A. M. Weiner, *Bell state analyzer for spectrally distinct photons*, 2021.

[17] S. Guha, H. Krovi, C. A. Fuchs, Z. Dutton, J. A. Slater, C. Simon, and W. Tittel, "Rate-loss analysis of an efficient quantum repeater architecture", Phys. Rev. A **92**, 022357 (2015).

[18] P. Senellart, G. Solomon, and A. White, "High-performance semiconductor quantum-dot single-photon sources", Nature nanotechnology **12**, 1026–1039 (2017).

[19] S. Buckley, K. Rivoire, and J. Vučković, "Engineered quantum dot single-photon sources", Reports on Progress in Physics **75**, 126503 (2012).

[20] Y. Arakawa and M. J. Holmes, "Progress in quantum-dot single photon sources for quantum information technologies: a broad spectrum overview", Applied Physics Reviews **7**, 021309 (2020).

[21] M. Nielsen, *A & chuang, il quantum computation and information*, 2000.

[22] W. P. Grice, "Arbitrarily complete bell-state measurement using only linear optical elements", Physical Review A **84**, 042331 (2011).

[23] S. Wein, K. Heshami, C. A. Fuchs, H. Krovi, Z. Dutton, W. Tittel, and C. Simon, "Efficiency of an enhanced linear optical bell-state measurement scheme with realistic imperfections", Physical Review A **94**, 032332 (2016).

[24] F. Ewert and P. van Loock, "3/4-efficient bell measurement with passive linear optics and unentangled ancillae", Phys. Rev. Lett. **113**, 140403 (2014).

[25] M. J. Bayerbach, S. E. D'Aurelio, P. van Loock, and S. Barz, "Bell-state measurement exceeding 50% success probability with linear optics", arXiv preprint arXiv:2208.02271 (2022).

[26] G. Kurizki, P. Bertet, Y. Kubo, K. Mølmer, D. Petrosyan, P. Rabl, and J. Schmiedmayer, "Quantum technologies with hybrid systems", Proceedings of the National Academy of Sciences **112**, 3866–3873 (2015).

[27] P. B. Sellin, N. M. Strickland, J. L. Carlsten, and R. L. Cone, "Programmable frequency reference for subkilohertz laser stabilization by use of persistent spectral hole burning", Opt. Lett. **24**, 1038–1040 (1999).

[28] P. B. Sellin, N. M. Strickland, T. Böttger, J. L. Carlsten, and R. L. Cone, "Laser stabilization at 1536 nm using regenerative spectral hole burning", Phys. Rev. B **63**, 155111 (2001).

[29] M. Colice, F. Schlottau, K. Wagner, R. K. Mohan, W. R. Babbitt, I. Lorgere, and J.-L. L. Gouet, "RF spectrum analysis in spectral hole burning media", in Optical information systems ii, Vol. 5557, edited by B. Javidi and D. Psaltis (International Society for Optics and Photonics, 2004), pp. 132–139.

[30] P. Berger, Y. Attal, M. Schwarz, S. Molin, A. Louchet-Chauvet, T. Chanelière, J.-L. L. Gouët, D. Dolfi, and L. Morvan, "Rf spectrum analyzer for pulsed signals: ultra-wide instantaneous bandwidth, high sensitivity, and high time-resolution", J. Lightwave Technol. **34**, 4658–4663 (2016).

[31] W. Tittel, M. Afzelius, T. Chaneliére, R. Cone, S. Kröll, S. Moiseev, and M. Sellars, "Photon-echo quantum memory in solid state systems", Laser & Photonics Reviews **4**, 244–267 (2010).

[32] F. Bussières, C. Clausen, I. Usmani, A. Tiranov, N. Sangouard, H. de Riedmatten, M. Afzelius, and N. Gisin, "Quantum memories with rare-earth-ion doped crystals", in 2013 conference on lasers and electro-optics pacific rim (2013), $MG2_2$.

[33] A. Kinos et al., *Roadmap for rare-earth quantum computing*, 2021.

[34] A. Ruskuc, C.-J. Wu, J. Rochman, J. Choi, and A. Faraon, *Nuclear spin-wave quantum register for a solid state qubit*, 2021.

[35] C. E. Bradley, J. Randall, M. H. Abobeih, R. C. Berrevoets, M. J. Degen, M. A. Bakker, M. Markham, D. J. Twitchen, and T. H. Taminiau, "A ten-qubit solid-state spin register with quantum memory up to one minute", Phys. Rev. X **9**, 031045 (2019).

ACKNOWLEDGEMENTS

This is probably the only non-scientific section of this thesis but carries equal significance as the rest of the scientific chapters.

Formulating a compact list of people who contributed to this work is a hard task. This also comes with the fear of missing out some important people. Nonetheless, I am going to take this risk and would try to acknowledge all those who have been a part of my life along the road to this Ph.D. journey; starting from my childhood, all the way up to my last-minute preparations before my Ph.D. defense. I reserve a special recognition to all of you. I will always be indebted to your efforts, and you will never be forgotten.

First and foremost, I would like to thank my supervisor, Prof. Wolfgang Tittel, for making this research possible, for his guidance, and for his support during the years of my Ph.D. that have culminated in this thesis. The fruitful discussions with him have helped me understand the problem and his advice and fresh ideas resulted in new progress. I wish him the best and all the success in the newly established lab in Geneva.

I would like to thank all the committee members of my Ph.D. defense - Prof. Ronald Hanson, Prof. Lieven Vandersypen, Dr. Johannes Borregaard, Prof. Mete Atatüre, Prof. Stefan Kröll, and Prof. Simon Gröblacher, for kindly spending their time to thoroughly read my thesis.

I would also take this opportunity to express my deep sense of gratitude and profound regard to my MS thesis supervisor Prof. Nirmalya Ghosh for his insightful advice, constant encouragement, and moral support throughout the wonderful journey of my research pursuit. The guidance I received from him can not be thanked in simple words.

In addition to this, I would like to express my sincere thanks to a very special friend, my dada - Mohsen. I was certainly not capable of doing everything that I have been doing now without his input and help. The first few months of my Ph.D. was indeed very challenging. Honestly, I would not have survived if he had not been there. Any word would fall short to describe his impact on my Ph.D.

I must not forget to mention the name of my teammate, my very good friend, Jacob (a.k.a Jake) who is really fun to interact with. After Mohsen left, he gave me good support and stood by my side in some tense moments. We could discuss really anything and everything. I believe, over the years, we really pushed each other to improve our dancing skills apart from the experimental skills. We really made the journey together and we shared each other's every high and low, joy and frustration. I wish him and Alex nothing

but the best.

I extend my sincere special thanks to my very good friend and an excellent teacher, Gustavo, for teaching me, and helping me whenever I faced some challenging situations in the lab. I have learned many experimental techniques from him. I have often irritated him with my silly questions and mistakes. Rather than getting angry, he encouraged me for asking doubts and explained them clearly.

Many thanks to Dr. Neil Sinclair and Dr. Anna Tchebotareva for all the interesting discussions during writing the journal articles. In every meeting with them, I have learned something new. Thank you very much for your input and constructive criticism which shaped my understanding of physics throughout my Ph.D.

I want to express my sincere gratitude to all the technicians and the support staff in QuTech. There is a whole lot of work that takes place behind the curtain and without their support, it would not have been possible for a Ph.D. student like me to keep going. A huge thanks to the cool group of general technicians - Siebe, Remco, Marc, Vinod, Roy, and Jelle; the cryo engineers Olaf and Jason for ensuring that the cryo is always up and running. Thanks to the very helpful electronics and control engineers - Raymond & Raymond, Roy, Jack, and our very own mechanical engineering team - Nico, Tim, and Stijn. A huge thanks to Jenny, Chantal, Shannon, Marja, Esther, and the rest of the management team for making my stay here at Delft, in a foreign country, much easier with all the diplomatic paper works.

I owe my deepest gratitude to some awesome people within our group and outside - very amazing Nir da, Tanmoy da, Sjoerd, Uri, Andreas, and Dorian for making my Ph.D. journey wonderful. Having these guys around as a friend and co-workers made everything easier. The work and the fun that I had with these people will always be cherished. Thanks to a lot of people for just being around, it was great having occasional chats with all of you - Fenglei, Mohammad, the “sid" duo Siddhant & Siddharth, Tim, Francisco, Guus, David, Carlo, Matteo, Max, Arian, Benjamin, Alejandro, Hans, Laurens, Yanik, Kian, Guido, Adrià, Pablo, Breno, Christine, Gertjan, Hemant and many more. Because of these people, QuTech has always felt warm, friendly, and vibrant.

In the last few weeks of my Ph.D., I have had the great opportunity to work with Emanuele. The successor of our lab. A very cool-headed and humble person. I hope with his positive approach, he will do excellent in his Ph.D. I wish him and Patrick good luck and all the very best with setting up a new lab in Geneva.

I feel grateful for all the lively, challenging, and enlightening discussions on various topics within and outside physics with my favorite Sudipta da, very calm and quiet Rajib da, undisturbed Ankit da, outspoken Subir da, and my childhood friends - Sankha and Pavak. Their continued effort motivated and inspired me to strive towards new goals.

Many individuals have had a huge influence on my studies here at Delft. Naming and

thanking them all would result in a very long list, but a few deserve a special thank you: Deepika, Hridya, Varun, and Gourab. These people have always made sure that I don't miss home very often. Special thanks to Koushik da, for teaching and cooking beautiful and delicious recipes. Home never felt away because of them. I must not forget to mention the name of Samya, Ricky, Ajmal, Subrata, Himadri, Rohith, Mayuri, Randhir bhaiya, Rana, Piuli, Saptarshi, Elizabeth, Garazi, and Megha. I think these guys all deserve a special mention because of making every bit of the memories very precious.

How can I forget about our very special QFA gang when it comes to life outside work? A big thanks to my sweetheart Cecilia, my beautiful friends - Monique, Andreia, Mariyeh, and my not-so-good friends - Jorgy, Gushu, and Mohamed. A big cheers to all those group outings and parties on the weekends. I hope, we will again be able to celebrate some meaningless occasion altogether. I owe my thanks to Nir da, Ayelet, and their family (including Elon, Guy, and Jonathan). You guys have hosted countless numbers of get-togethers and no stone has been unturned in terms of celebrating Christmas, kings day, Hanukkah, champions league matches, and whatnot. Throughout the pandemic, you people have been my family here in Delft. I would never have survived the past few years without you.

Playing football is always a very welcoming distraction from research work, especially with the Kavli Warriors team: Maarten, Chris, Conor, Tim, Hany, Jorge, Michael, Brecht, Sébastian, and Thijs, it was great to play football with you all.

Finally, above all else, I need to thank my partner in crime, my love, and most importantly my good friend Shramona (Memu). Thank you for supporting me over the last few years, I could not have made it without you. You make me truly happy, and I am so grateful for your love.

At last but not least, I want to express my sincere gratitude to all of my family members. Without the huge support of my whole family, my stay in the Netherlands, far away from my home, would not have been possible. Especially my parents: Bikash Ch. Das and Madhuri Das for fighting at each step, their tireless encouragement, and moral support during my Ph.D. They mean the world to me. I take this opportunity to thank my elder sister, Camelia for her encouragement and good wishes throughout my life. This accomplishment would not have been possible without them.

I feel blessed that I had the privilege to be taught by some excellent teachers in my life: my father Bikash Ch. Das, Amal Bhattacharya, Prof. Narayan Banerjee, Prof. Nirmalya Ghosh, Soumyadeep Mukherjee, Subhankar Deb, Mrinalkanti Deb, Samir Saha, Jayanta Chakraborty, and many more. I am highly obliged for their enormous support, works of inspiration, and guidance. They helped me to shape my career goals and also seeded the desire to learn and develop my skills to explore the unknown.

I would also like to thank all the people who read my thesis. Thank you for sticking with this thesis so far.

Thank you all for being such an important part of my journey!

LIST OF PUBLICATIONS

6. *Quadratic Zeeman spectral diffusion of thulium ion population in a yttrium gallium garnet crystal*,
Jacob H. Davidson[1], **Antariksha Das**[1], Nir Alfasi, Rufus L Cone, Charles W Thiel, Wolfgang Tittel
In communication with Phys. Rev. B
arXiv:2210.05005 (2022).

5. *Optical coherence and relaxation dynamics in a thulium-doped yttrium gallium garnet crystal at sub-kelvin temperatures for quantum memory applications*,
Antariksha Das[1], Mohsen Falamarzi Askarani[1], Jacob H. Davidson et al.
In preparation.

4. *A long-lived solid-state optical quantum memory for high-rate quantum repeaters*,
Mohsen Falamarzi Askarani[1], **Antariksha Das**[1], Jacob H Davidson, Gustavo C Amaral, Neil Sinclair, Joshua A Slater, Sara Marzban, Charles W Thiel, Rufus L Cone, Daniel Oblak, Wolfgang Tittel,
Phys. Rev. Lett. **127**, 220502 (2021).

3. *Measurement of the thulium ion spin Hamiltonian in a yttrium gallium garnet host crystal*,
Jacob H Davidson, Philip JT Woodburn, Aaron D Marsh, Kyle J Olson, Adam Olivera, **Antariksha Das**, Mohsen Falamarzi Askarani, Wolfgang Tittel, Rufus L Cone, and Charles W Thiel
Phys. Rev. B **104**, 134103 (2021). Featured as an editor's suggestion.

2. *Frequency multiplexed photon pairs and detection for quantum repeaters*,
Tanmoy Chakraborty, Hedser van Brug, **Antariksha Das**, Oriol Pietx-Casas, Peng-Cheng Wang, Gustavo Castro do Amaral, Anna L. Tchebotareva, Wolfgang Tittel
arXiv:2205.10028 (2022).

1. *Spin-selective scattering modes in a disordered anisotropic optical medium*,
Ankit Kumar Singh, **Antariksha Das**, Sourin Das, Nirmalya Ghosh
Phys. Rev. A **102**, 033518 (2020).

[1] These authors contributed equally to this work

CURRICULUM VITÆ

Antariksha DAS

30-11-1995	Born in Dinhata, West Bengal, India.

EDUCATION

2005-2013	Secondary and Higher Secondary education Dinhata High School, Dinhata, Coochbehar, West Bengal, India
2013-2018	Integrated Bachelor's & Master's of Science (BS-MS) in Physical Sciences Thesis: "*Spin Optical Effects in Spatially Tailored Media*" Under the supervision of Prof. dr. Nirmalya Ghosh Indian Institute of Science Education and Research (IISER) Kolkata, India
2018 - 2023	Doctorate in Physics Delft University of Technology, Delft, The Netherlands
Thesis:	*Towards a Long-Lived and Efficient Photonic Quantum Memory in a Thulium-Doped Crystal*
Promotors:	Prof. dr. Wolfgang Tittel Prof. dr. Ronald Hanson